Performance Enhancement of Solution-Processed Organic-Inorganic Halide Perovskite Solar Cells

著者（英）	Md. Emrul Kayesh
year	2019
その他のタイトル	溶液プロセスによって作製された有機無機ハライドペロブスカイト太陽電池の性能向上
学位授与大学	筑波大学 (University of Tsukuba)
学位授与年度	2018
報告番号	12102甲第8978号
URL	http://doi.org/10.15068/00156643

Performance Enhancement of Solution-Processed Organic-Inorganic Halide Perovskite Solar Cells

Md. Emrul Kayesh

February 2019

Performance Enhancement of Solution-Processed Organic-Inorganic Halide Perovskite Solar Cells

Md. Emrul Kayesh

Doctoral Program in Materials Science

Submitted to the Graduate School of
Pure and Applied Sciences
in Partial Fulfillment of the Requirements
for the Degree of Doctor of Philosophy in
Engineering

at the
University of Tsukuba

Abstract

Perovskite solar cells (PSCs) have sparked great excitement in the scientific community due to their easy and low cost of fabrication. With significant contribution from researchers around the world, the power conversion efficiency (PCE) of PSCs has been approached to the established photovoltaic technology within a few years. However, the stability and toxicity issues, prevent the commercialization of PSCs. At present, a lot of research have been focused not only to fabricate efficient device but also stable. For PSCs, the perovskite materials itself, having higher sensitivity towards moisture and oxygen, is the key issue for stability. It has been demonstrated that the morphology and crystallinity of perovskite film determine the performance of PSCs. If the perovskite films contain pin-holes, oxygen and moisture can easily penetrate into the inner domain and oxidize. So, the fabrication of pin-hole free uniform and robust nature of perovskite films is the prerequisite for efficient and stable PSCs. In order to achieve these goals, the main focus of this thesis is to develop the perovskite films for high efficiency and stable PSCs.

Therefore, in this thesis, the widely used one step anti-solvent dripping (ASD) method was optimized through the detail observation of different anti-solvents such toluene, chlorobenzene, *p*-xylene and ether treatment on the $MAPbI_3$ films and corresponding device performance. From the structural and optical characterization, it was revealed that the intrinsic properties of perovskite were independent of different anti-solvent treatment, but the morphology changed which affects the corresponding device performance. Due to the high boiling point and miscibility in precursor solution, toluene and chlorobenzene treated perovskite form single grain structure across the cross-section with high stability. As a result, the corresponding devices showed highly efficient and stable performance both in dark and under continuous light illumination. Hence, a correlation between different anti-solvent treatment with morphology of perovskite films and stability in corresponding device was observed.

In ASD method, usually a mixed of solvents such as Dimethylformamide (DMF) and Dimethyl sulfoxide or DMF and Gamma-Butyrolactone are used to control the perovskite crystallization rate by forming intermediate complex with metal halide before final perovskite film formation. However, for large scale commercial applications, the ASD system with single solvent precursor solution is more beneficial. But the perovskite film from single solvent precursor system experienced poor morphological and optoelectronic properties which negatively affect the final device performance.

Therefore, in this thesis, an additive engineering was performed for single solvent precursor system to control the crystallization rate of perovskite films. Here, copper chloride (II) was used as additive in which the Cl^- ion formed intermediate phase with PbI_2 and slowed down the $CH_3NH_3PbI_3$ crystallization rate. As a result, larger and uniform grain size perovskite film with optimum optoelectronic properties was observed and the corresponding PSCs showed 56% higher PCE as compare with the pristine PSCs.

Although the PCE of Pb-based PSCs has approached to 23.3%, but the toxicity of Pb in PSCs effectively hinders their wide spread applications. As an alternative of Pb, Sn-based perovskites have been extensively explored due to their similar or even superior photovoltaic properties. However, the Sn-based PSCs

suffer from poor device performance and stability. This is because, the facial tendency to Sn^{2+} oxidation and inability to form pin-hole free uniform Sn-based perovskite films. For Sn-based perovskite film formation, SnF_2 has been identified as essential additive for continuous film with lower Sn^{4+} content. However, the addition of SnF_2 more than 10 mol% causes phase separation but at this concentration, the perovskite contains a lot of pin-holes with higher Sn^{4+} content.

Therefore, along with SnF_2, a coadditive engineering with hydrazinium chloride (N_2H_5Cl) was performed to use its dual beneficial aspects for controlling crystal growth rate and retarding Sn^{2+} oxidation. To do this, the additive engineered single solvent precursor system was used that was optimized during the Pb-based work. A detail morphological, structural and optoelectronic characterizations were performed to observe the effects of N_2H_5Cl on the fabricated films. From these analyses, it was revealed that the addition of N_2H_5Cl reduce the Sn^{4+} concentration up to 20% which lead to the suppression of charrier recombination and pinhole-free uniform coverage. These remarkable improvements in $FASnI_3$ film enhanced both PCE and shelf life stability of Sn-based PSCs in dark condition. However, these devices showed poor light soaking stability but for real life implementation, this is the most crucial factor for a solar.

In an attempt to improve light soaking stability of Sn-based PSCs, another coadditive engineering was performed with long carbon chain containing bifunctional organic additive, 5-ammonium valeric acid iodide (5-AVAI). From the ^1H NMR analysis, it was observed that the addition of 5-AVAI into the precursor solution undergoes a hydrogen bond interaction with SnI_6^{4-} octahedra through its bifunctional groups ($COOH^-$ and NH_3^-). This interaction slowed down the perovskite crystallization rate and cross-linked adjacent grains to form pinholes-free uniform and crystalline film with a preferred orientation along <h00> direction. As a result, the addition of 5-AVAI augmented the PCE of $FASnI_3$-based PSCs from 3.4 to 7.0% in a 0.25 cm^2 area. Moreover, this additive formed a hydrophobic layer over the perovskite film which protects the perovskite film from moisture and oxygen. This enhanced the air stability of $FASnI_3$ film and the corresponding PSCs were able to maintain their initial performance for 100 h under continuous illumination and at maximum power point tracking conditions.

Contents

Chapter 1

General Introduction

1.1 Motivation

1.1.1 Global Worming

Energy is the basic need of humankind. The demand of energy is increasing exponentially with rising population and development of newer technology. The human race needs more energy than ever for the advancement of civilization towards the future direction. Energy has different forms such as thermal energy, mechanical energy, electrical energy, magnetic energy, chemical energy, nuclear energy etc. Among these, electrical energy is the most convenient form of energy which can be easily converted to any other form of energy as required. At present, the modern civilization is based on the electrical energy.

Usually, Electricity is harnessed by burning fossil fuels, nuclear power sources, and renewable energy sources. Due to the safety and difficulty in radioactive waste disposal process issues, nuclear power plants have lost their attractiveness. In addition, improper radioactive waste disposal leads to threatn environment and life. At present, production of electricity by burning fossil fuels is the only choice from the cost and available technological perspective. However, fossil fuel will not able to meet the growing energy demand of world economy for long time. It has been estimated that the reserve oil and natural gas will be depleted within several decades if other alternative energy sources are not developed.

Moreover, over usage of fossil fuels generates a lot of toxic gases which are responsible for many environmental disasters. After the industrial evaluation, the concentration of CO_2, one of the greenhouse gas (GHG), has been increased up to 35% primarily due to burning of fossil fuel.[1]The greenhouse gases act as a blanket for infrared radiation which traps the radiative energy and increases temperature. This is triggering the melting of polar ice in the north and south pole. As a result, the rise of sea level start to threaten the existence of many countries which are at par or below sea level.

By realizing the threat, a lot of efforts are being taken to generate environmental awareness from all over the world. Among the different global organization, the United Nation Framework on Climate Change is regularly organizing Conference of Parties (COP) since 1995 to make an agreement among all nations. From these efforts, the organizers have succeeded to achieve a huge landmark at COP21 in 2015, whereby all nations agreed to keep the global warming level below 2°C. After realizing the severity of global warming, the green policies are now being seriously adopted by a lot of country. To fight against the global warming and to secure the energy crisis, the strategies have been taken mainly based on uprooting its base such as stop deforesting and limiting CO_2 emission. Although continuous efforts have been given to make these processes more sustainable but still over 80 % of the global energy demand is now fulfilled by using fossil fuels such as coal, oil, natural gas etc. So, to get ride from the global warming problems, we must have to focus on the substitution of fossil fuel with renewable energy.

1.1.2 Renewable Energy

Renewable energy is known as the green energy which are generated from the infinite natural source. The production of energy from the renewable sources such as sunlight, wind, rain, tides, waves, biomass and geothermal heat etc. are clean, natural and have no negative impact on the earth's atmosphere. In comparison with other energy source, renewable energy resources exist over wide geographical areas. So, the development of renewable energy can solve a lot of current major problems such as energy crisis, climate change and economic scourge. To discourage the use of fossil fuel, an ordinance has been passed in which the GHG emitters will have to pay penalty for the climate change due to the GHG effect.[2] This initiative will provide powerful tool for the development of renewable energy technologies. To promote the development of renewable sources such as solar power and wind power, an international public concern has already been grown. In this regard, 30 countries have started to use renewable energy sources and meet more than 20% of their energy requirement from these sources. Some countries such as Iceland and Norway have fixed their goals to meet their all energy demand from renewable energy in near future. In this regard, Denmark has decided to use 100% renewable energy for their total energy supply by 2050.

In general, to implement the renewable energies in practical life, they must have to price competitive against the energy divided from the conventional sources. In this parameter, every source of renewable energy has its own limitations. For example, although the production of electricity from hydropower is much cheaper but their main disadvantages are the location of the plant, dependency of rainfall, cost of energy transmission and the significant impact on the environment as large area have to be flooded. The other renewable sources of energy such geothermal, wave and biomass are very much inefficient and also much depended on the nature which make them unrealistic for applications. This leaves wind and solar are the only realistic candidate as the substituent of fossil fuel and hope for the future energy demand. But these sources also have some of their won disadvantages, beside high cost of fabrication, they are also depended on the nature such as wide and sun light. Due to this dependency, the power grid integrates with a substantial amount of wind and solar power, must have to build up a storage system or a very efficient way of energy re-distribution among different remote area. Despite of these limitations, the wind and solar are consider as the only future green energy supplier due to their abundant source materials.

1.1.3 Solar Energy

Due to eco-friendly and sustainability, the solar energy has attracted tremendous attention.[4] Every year, the sun supplies energy to earth on the order of gigantic i.e. 33×10^{24} joule which is about 10,000 time more than what mankind consumes currently. This means the solar panels with 2 % power conversion efficiency (PCE) covering 1.5% of total land area of earth are sufficient to fulfill current energy demand. So, the efficient harness of sun light can solve most of the urgent problems associated with energy that the world is facing now.

According to a theoretical calculation, the sun will shine more than six billion years with its full illumination. In term of energy sources, only solar energy is more than enough to meet the world's energy demand without any adverse effect to human beings as well as without contributing to any greenhouse gases to the atmosphere in the up-coming future.[5] Therefore, solar energy is the only potential renewable source to fulfill the current and future energy demand. At present, most of the develop countries are moving toward solar cells or photovoltaic devices to meet their energy demand.

1.1.4 Solar Cells

The photoelectric effect was first observed by a French physicist, Edmund Bequerel as early as 1839. With ~1% PCE, the first photovoltaic cell was built in 1883. The photovoltaic devices attracted much attention with the significant enhancement of PCE up to 6% by Bell Laboratories in 1954. But the use of photovoltaic devices was still limited due to their complicated and expensive fabrication procedure. In 1960s, the space programs research revealed the fundamental mechanism of photovoltaic which drastically improved the performance and cost effectiveness. Later the rise of energy crisis forced the researcher to involve into the photovoltaic technology as an alternative source of fossil fuel. The solar cells can be classified into three generations such as first, second and third. The first-generation solar cells are based on silicon wafer such as monocrystalline, polycrystalline and amorphous silicon solar cell. At present, these type of solar are dominating the market although their high cost of expensive fabrication. With much cheaper, thin films based solar cells are known as the second-generation solar cell such cadmium telluride and copper indium selenide/sulfide solar cells etc. In comparison with the first generation, these solar cells are much cheaper but still expensive due to their sophisticated fabrication technology. To overcome these problems, the third-generation solar cells have been developed which involve easy and low-cost fabrication techniques. The third-generation solar cells include organic photovoltaics, dye-sensitized solar cells (DSSC), quantum dot sensitized solar cells, and perovskite solar cells (PSCs) etc. Among the third-generation solar cells, the PSCs have experienced a rapid enhancement of PCE within very short period and become a competitor with the existing silicon solar cells in the market. Although an enhanced PCE of PSCs have been observed but some crucial drawbacks such toxicity of Pb, stability and reproducibility etc. effectively hinder their commercial applications. In accord to the latest development of PSCs, the aims of this study are to solve some of the existing problems in this solar cell device engineering technology.

1.2 Perovskite Solar Cells

1.2.1 Properties of Perovskite

Perovskite solar cells are the third-generation solar cell in which the active layer that’s means the absorber is made of perovskite material. The perovskite material is composed of optimum photovoltaic properties which makes them most suitable candidate for solar cells. Some of their important properties are

discussed in the following section.

Crystal Structure of Organic-Inorganic Perovskite Materials

The crystal structure of organic-inorganic perovskite is generally expressed by ABX_3 formula. Here the $[BX_6]$ octahedrons share their corner in three-dimensional space as shown in figure 1.1. In this structure the A site is monovalent organic or inorganic cation ($CH_3NH_3^+$ $NH_2CHNH_2^+$ or Cs^+), B is the divalent metal cation (Pb^{2+} or Sn^{2+}) and X is the halogen anion (Cl^-, Br^- or I^-). The figure 1.1 schematically illustrate a unit cell of 3D perovskite.

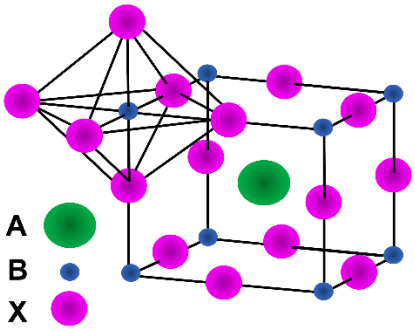

Figure 1.1: The unit cell of 3D organic inorganic perovskite structure

To form a stable perovskite structure, ionic radius of cation (A) and anion (B) must be maintained a certain ratio range which is known as tolerance factor. The tolerance factor (t) is expressed by the follows expression.[6]

$$t = \frac{R_A + R_B}{\sqrt{2}(R_B + R_X)}$$

Where R_A, R_B, R_X are the ionic radius of cation A, cation B and anion X respectively. Depending on the value of tolerance factor different type of perovskite is formed. The following table shows the range of tolerance factor and corresponding structure.

Table 1.1: Tolerance factor for perovskite materials

Tolerance factor	Structure	Comments
<0.7	Non-perovskite	A is too small or B is too large
0.7-0.9	Tetragonal/orthorhombic rhombohedral	Ideal perovskite structure
>1.0	Various layered structures	A-cation too large

Beside tolerance factor, the octahedral factor (μ) must be fulfilled to form perovskite structure which can be expressed by the following equation.

$$\mu = \frac{R_B}{R_X}$$

Table 1.2: Value of tolerance and octahedral factor of some common perovskite materials

Compound	*t*	*μ*	Perovskite
$CH_3NH_3SnI_3$	0.720	0.536	Yes
$CH_3NH_3PbI_3$	0.822	0.541	Yes
$CH_3NH_3CdI_3$	0.884	0.432	no

Table 1.2 shows some value of tolerance and octahedral factor. From this table we can see that to form perovskite both tolerance and octahedral factor must be fulfilled. The octahedral factor should be higher than 0.442.[7]

The phase or structure of perovskite is also dependent on temperature. Here table 1.3 shows the range of temperature over which different phase exist for $CH_3NH_3PbX_3$ (X=Cl^-, Br^-, and I^-).

Table 1.3: Crystal structure data for $CH_3NH_3PbX_3$(X=Cl^-, Br^- and I^-) as a function of temperature.[7]

Structure	$CH_3NH_3PbCl_3$	$CH_3NH_3PbBr_3$.	$CH_3NH_3PbI_3$.
Cubic	>178.8 K	>236.9 K	>327.4 K
Tetragonal	172.9-178.9 K	144.5-236.9 K	162.2-327.4 K
Orthorhombic	<172.9 K	<144.5 K	<162.2 K

High Absorption Coefficient

Perovskite materials usually have very high absorption coefficient. For example, the $MAPbI_3$ has an absorption coefficient of about $1.5x10^4$ at 550 nm. This value is one order higher than that of silicon.[8-9] The large absorption coefficient value help to efficient light absorption with a thin absorber. The thinner the absorber is, the lesser the defect and higher the charge recombination resistance. Thus, the absorber material with higher absorption coefficient not only absorb light more efficiently but also have optimum photovoltaic properties.[10]

Low Exciton Binding Energy

The exciton binding energy is the required energy needed to dissociate exciton into free electron and hole. Lower exciton binding energy is needed to reduce energy loss. For example, the lower open circuit voltage (V_{OC}) in organic photovoltaic cells are mainly due to the higher exciton binding energy which are in the range of 0.6 V to 1.0 V.[11] On the other hand, depending on the perovskite materials, the excitonic binding energy is in the range of 9-80 mV.[12] Such a small energy value help to contribute lower V_{OC} losses in PSCs.

Long Charge Carrier Diffusion Length

Solution process organic-inorganic perovskites show much longer carrier diffusion length (500 nm-8000 nm) in comparison with the organic semiconductors (~10nm).[13] For photovoltaic application, the carrier diffusion length is one of the most important parameter for efficient charge transportation. The longer diffusion length allows to increase the thickness of absorber layer without affecting charge recombination and collection. The diffusion length is related with charge carrier lifetime (τ) and mobility (μ) according to the following equation.

$$L_D = \sqrt{K_B T \mu \tau}/e$$

Here, K_B, T and e are the Boltzman constant, temperature and elementary charge, respectively.
All of these parameters depend on the crystallinity, morphology, and type of defects of perovskite materials.

Ambipolar Charge Transport

The perovskite is well known for its ambipolar charge transport properties in which they can transport both electron and hole in a balance way. Most of the semiconductor show unbalanced transport properties due to their higher difference in effective mass of electron and hole (m_e^* and m_h^*). On the other hand, theoretical analysis shows that effective mass of electron and hole in perovskite is nearly similar ($m_e^* = 0.23\ m_0$ and $m_h^* = 0.29 m_0$) which balance ambipolar charge transportation.[14] In a working solar cell, the bulk polarization depends on the balanced ambipolar charge transportation, consequently affects the short circuit current (J_{SC}), open circuit voltage (V_{OC}) and fill factor (FF). So, the ambipolar charge transportation is necessary properties for solar cell. The perovskite can behave as n-type or p-type depending on the interfacial layer to which it is attached.[15]

Predominant p-Type Character in Perovskite

Although perovskite is considered as an intrinsic semiconductor, but it usually behaves p-type or n-type depending on the synthesis procedure. For example, if Sn-based perovskite is synthesized from reducing condition it become n-type but when it is synthesized from oxidizing condition it behaves like p-type semiconductor. But in general, both Sn-based or Pb-based perovskite behave p-type.

1.2.2 Structure of Perovskite Solar Cells

The first perovskite solar cells were based on DSSC type in which $CH_3NH_3PbI_3$ (perovskite) was used as a sensitizer on thick mesoporous scaffolds in 2009.[26] Due to the reaction between liquid electrolyte and perovskite, the cell was too unstable. This problem was overcome by replacing electrolyte with solid state

hole transporting material. After that the PSCs experienced a rapid development. At present, the PSCs have mainly three type structure which are briefly discussed in the following section.

Meso TiO_2 Structure

Figure 1.2 shows the meso TiO_2 structure. In this structure, a mesoporous TiO_2 layer is deposited on to the transparent fluorine doped tin Oxide (FTO) or indium tin oxide (ITO) coated glass as an electron transporting layer (ETL). Then a perovskite capping layer is placed on the TiO_2. After that the hole transporting layer, followed by metal electrode (Au or Ag).

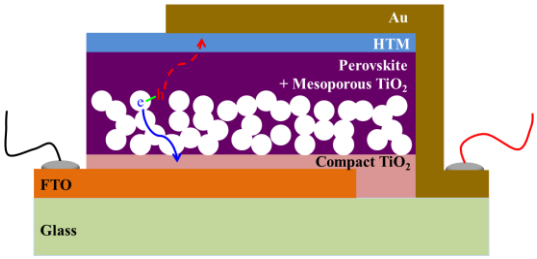

Figure 1.2: Meso TiO_2 type PSC

Planar Structure

The sequence of different layers of planar structure is same as the meso -TiO_2 structure. The only difference is the use of compact ETL (such as TiO_2, SnO_2 etc.) instead of meso-TiO_2 layer. The figure 1.3 schematically shows the planar structure of PSCs.

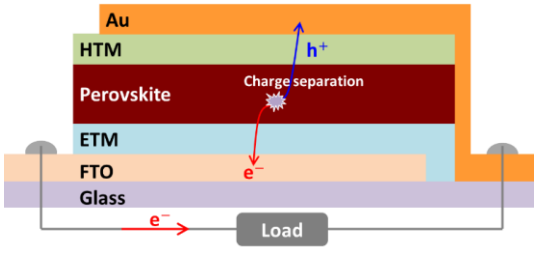

Figure 1.3: Planar structure PSCs

Inverted Planar Structure

The Inverted Planar PSCs is just opposite of normal structure in which a hole transporting layer (HTL) is first deposited on the transparent conductive oxide coated (FTO or ITO) glass. Then, the perovskite

layer is deposited on to it. Subsequently, the ETL is deposited on the perovskite layer and finally the photovoltaic device is completed by evaporating low work-function metal such Au or Ag (Figure 1.4).

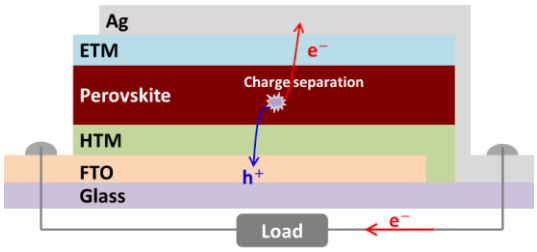

Figure 1.4 Inverted planar structure PSCs

1.2.3 Perovskite Film Deposition Technique

For PSCs, the deposition of perovskite film is the most important part as its quality determine the performance of device. There are several methods have been developed for the fabrication of perovskite film such one-step annealing method, two-step dipping method, vapor assist solution process, dual sources vapor method and one-step anti-solvent method. A brief discussion about different fabrication methods are given in the following paragraph.

1.2.3.1 One Step Annealing Method

In this method, the starting material such AX (A = methylammonium ion or formamidinium ion etc. and X= I, Br, Cl etc.) and BX_2 (B = Pb^{2+} or Sn^{2+} etc.) is first dissolved in a suitable solvent such (Dimethylformamide) DMF or (Dimethyl sulfoxide) DMSO or (Gamma-Butyrolactone) GBL to make precursor solution. The precursor solution is then spin coated at a certain speed for a certain time. After that, it is annealed at 100 ^{O}C to 120 ^{O}C time for 30 to 60 min and obtained the final perovskite film. Figure 1.5 schematically show the whole process.

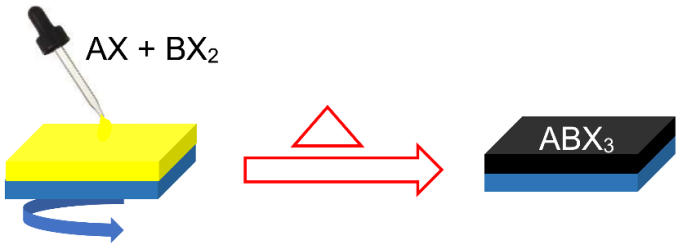

Figure 1.5: Schematically represent the one step annealing method

1.2.3.2 Two-Step Dipping Method

In two-step dipping method, BX_2 is fist dissolved in a suitable solvent (DMF, DMSO etc.) to make precursor solution. The precursor solution is then spin coated at a certain rate and dried at room temperature. After that it is dipped in to AX solution (usually Isopropanol used as solvent) and annealed at 100 ^{0}C to 130 ^{0}C for 30 min to obtain final perovskite film. Figure 1.6 schematically shows the two-step dripping processes. The morphology of perovskite film directly depends on the concentration of both BX_2 and AX solution.

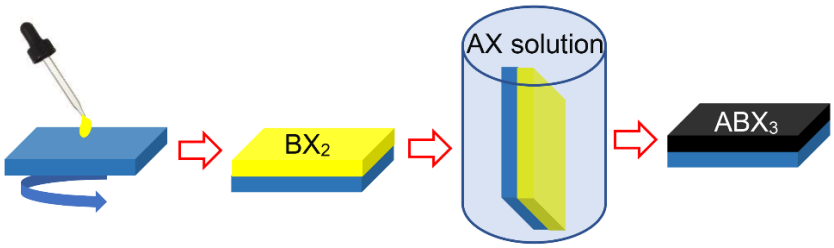

Figure 1.6: Schematically represent the two-step dipping method

1.2.3.3 Dual Source Vapor Method

The dual source vapor method was developed by Snaithe et al. in 2013 and produced high quality perovskite film with uniform thickness. In this method, AX and BX_2 are placed into two crucibles and simultaneously evaporated. The thickness and composition of perovskite film are controlled by regulating the evaporation rate (Figure 1.7). All the process is performed under high vacuum and needed relatively longer time in comparison with spin coating method.

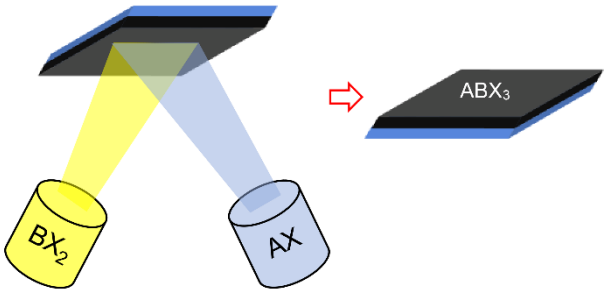

Figure 1.7: Schematic illustration of perovskite film formation through dual source vapor method

1.2.3.4 Vapor Assist Solution Process

In vapor assist solution process, BX_2 layer is first deposited by spin coating BX_2 solution at a certain

rotation speed for certain period of time, and dried at 110 ^{0}C for 15 min. Then, AX powder was spread out around the BX_2 coated substrates with a petri dish covering on the top and heated at 150 °C for desired time (Figure 1.8). Both the deposition of BX_2 film and vapor treatment of BX_2 film are carried out in glovebox. After cooling down, the as-prepared substrates are washed with isopropanol, dried and annealed.

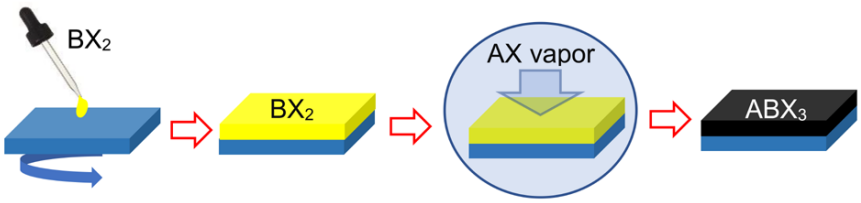

Figure 1.8 Schematic presentation of perovskite film formation through vapor assist solution process.

1.2.3.5 One Step-Anti Solvent Dripping Method

One-step anti solvent dripping (ASD) method is considered as the most efficient perovskite film fabrication method, was developed by Seok et al in 2014. In this method, the perovskite precursor solution is prepared by mixing AX and BX_2 in to a solvent or mixture of solvents such DMF or DMSO or DMF-DMSO etc. The precursor solution is then spin coated at a certain rate and during this spinning an optimum amount of anti-solvent is dripped on the substrate to accelerate the heterogeneous nucleation. After completing the spin coating, the substrate is annealed at 100 ^{0}C to 130 ^{0}C for 30 min to obtain highly uniform crystalline perovskite films. Figure 1.9 schematically shows the whole process.

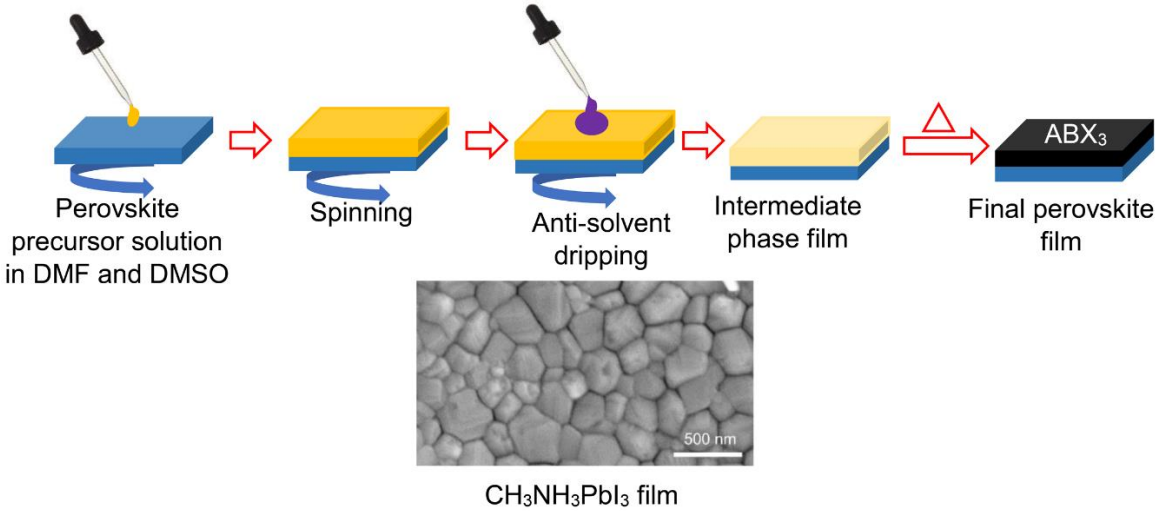

Figure 1.9: Schematic illustration of one-step anti-solvent dripping method

1.2.4 Working Principle of Perovskite Solar Cells

When light is illuminated on to the perovskite material, electron from the valence band moves to the conduction band and creates exciton (i.e. electron-hole pair) (Figure 1.10). As the perovskites have low excitonic binding energy (i.e. 4-22 meV for $CH_3NH_3PbI_3$), the exciton dissociated into free electron and hole at room temperature and move across the device. Due to the high charge mobility and long diffusion length, electron and hole can easily move across the perovskite. Thus, electron diffuse through the perovskite to the ETL and subsequently collected to the electrode whereas the photogenerated holes diffuse through the perovskite and collected at the electrode. The ETL and HTL are also known as the charge blocking or selective layer and are vital for the performance of PSCs. By the virtue of ETL and HTL, the right charge is collected at the appropriate electrode whereas the wrong one is prevented. To do this, selection of ETL or HTL with appropriate energy levels with respect to those of perovskite is most crucial. To be a good HTL for optimum photovoltaic operation, it should have its conduction band or lowest unoccupied molecular orbital far above that of conduction band of perovskite. Simultaneously, the valence band or highest occupied molecular orbital of HTL should be just above the valence band of perovskite. The opposite requirements are needed for ETL to screen the appropriate charges. This charge selectivity property is essential for the device performance because if an electron reach to wrong electrode it will recombine non-radiatively with one of many holes present there. This process leads the unwanted loss of photogenerated charges.[27-28]

The charge recombination also occurs at the interface, grain boundaries or impurities in the perovskite leading to the conversion of these photogenerated charge into heat by a process of non-radiative recombination. This process is unwanted and can be minimized by controlling these defects. But there is one type radiative recombination in which the photogenerated charges recombine each other and emits photon leading to the loss of effective carriers. This is a natural phenomenon and cannot be avoided.

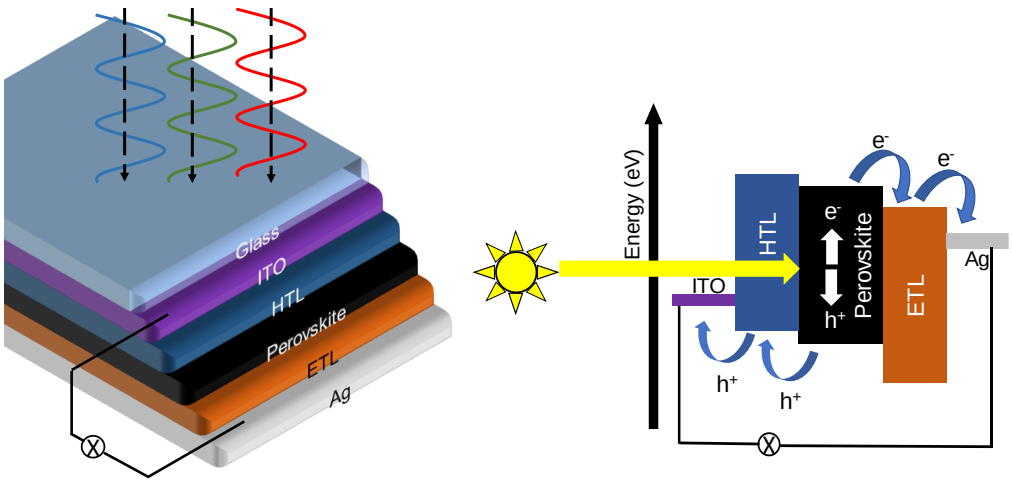

Figure 1.10: Schematic illustration of working principle of PSC for inverted planar (ITO/HTL/perovskite/ETL/metal electrode) structure with energy diagram.

1.2.5 Characteristics of Perovskite Solar Cells

The perovskite solar cell is behaved like a diode in dark condition (Figure 1.11a) but when illuminated its current increased by an order of magnitude which is due to the photogenerated current (Figure 1.11b). For solar cell, the performance is determined through the current/voltage measurement. To do this, usually several potentials is applied (from negative value to positive value) and measure the corresponding current.

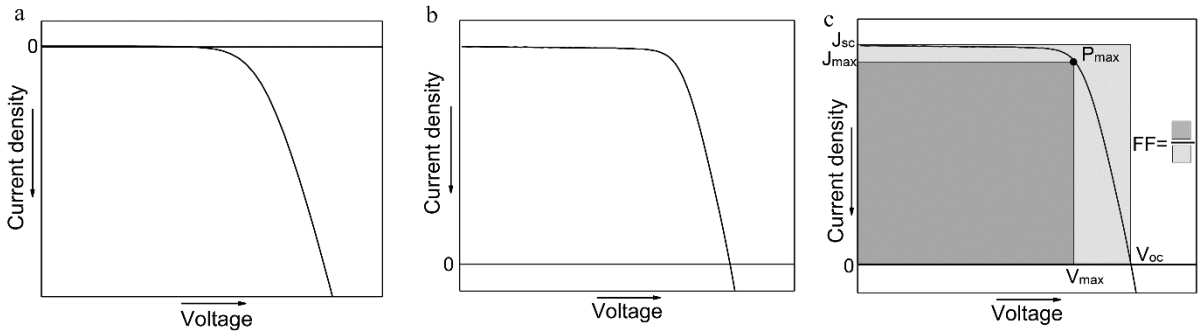

Figure 1.11 J-V curves of PSCs measured under dark (a) and illumination conditions. J-V curves measured under illumination and the corresponding performance parameters (c).

To determine the performance of solar cell, three parameters, short circuit current (J_{SC}), open circuit voltage (V_{OC}) and fill factor (FF) (Figure 1.11) are needed which can be defined by the following equation:

Power conversion efficiency (PCE) = $\eta = \frac{P_{out}}{P_{in}} X100 = 100 = \frac{J_{MAX}V_{MAX}}{P_{in}} X100$

$$FF = \frac{J_{MAX}V_{MAX}}{J_{SC}V_{OC}}$$

$$PCE = \frac{J_{SC}V_{OC}FF}{J_{SC}V_{OC}} X100$$

to account the resistive loss, a series (R_S) and shunt resistance (R_{SH}) are added to the equivalent circuit of solar cell (Figure 1.12). So, the characteristic J-V curve can be expressed by the following equation.

$$J = J_{ph} - J_0 \left\{ \exp\left[\frac{q(V + JR_S)}{nkT}\right] - 1 \right\} - \frac{V + JR_S}{R_{sh}}$$

Where, J_{ph}, J_0, n, k, q and T are the photogenerated current density, reverse saturation current density, ideality factor of the diode, Boltzmann's constant, temperature and elementary charge respectively. So, from this equation, we can see that the PCE of solar cell is mainly depended on the J_0, R_s and R_{sh}.

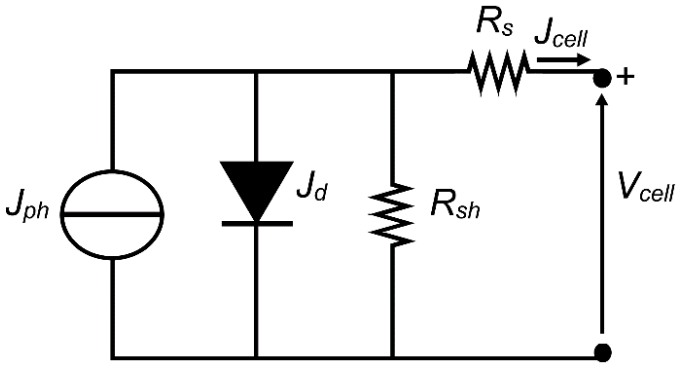

Figure 1.12 Equivalent circuit of solar cell.

For a solar cell, quantum efficiency is one of the important measure which provide information that how efficiently convert the incident light into the electrical energy at a given wavelength. There are two types of quantum efficiency exist: internal quantum efficiency (IQE) and external quantum efficiency (EQE).

EQE is the ratio between the number of collected charge to the total number of incident photons on a certain active area at a given wavelength.

$$EQE = \frac{electrons/sec}{photons\ /sec} = \frac{current/(charge\ of\ one\ electron)}{(total\ power\ of\ photons)/(energy\ of\ one\ photon)}$$

IQE is the ratio between the number of collected charge to the number of incident photons at a given wavelength that are absorbed by the absorber layer only.

$$EQE = \frac{electrons/sec}{photons\ /sec} = \frac{EQE}{1 - reflection - transmission}$$

Due to the loss of light by reflection or transmission, the EQE is always less the IQE. The difference between IQE and EQE is used to identify the loss mechanism between absorbed photons and photo to charge conversion efficiency of absorbing materials. Generally, EQE is referred as incident photon to carrier conversion efficiency (IPCE) and is measured by using chronoamperometry (potentiostate). The IPCE is expressed by the following equation,

$$IPCE\ (\lambda) = EQE(\lambda) = \frac{electrons/cm^2/s}{photons/\ cm^2/s} = \frac{j_{ph}\left(\frac{mA}{cm^2}\right) X1239.8\ (VXnm)}{P_{mono}\left(\frac{mW}{cm^2}\right) X\ \lambda(nm)}$$

Where, 1239.8V X nm is the product of plank's constant and speed of light (c), P_{mono} is the illuminated power intensity in mW/cm^2 and is the wavelength at which illumination power is measured. So, the integration of IPCE over the measured wavelength will give the J_{SC} of solar cell. The result of this measurement makes a curve in which it crosses the voltage axis (X) at a point called open circuit voltage (V_{OC}) and the current axis (Y) at a point called the short circuit current (J_{SC}).

1.3 Toxicity of Pb in Perovskite Solar Cells

PSCs have undergone rapid progress during the last decade and reached the PCE over 23%.[16] Despite the impressive progress in Pb-halide perovskite photovoltaics, the commercialization of PSCs are facing several challenges related to presence of toxic lead element and stability upon prolonged exposure to light, humidity, and high temperature. Moreover, the implementation of Pb-based PSCs in real life is effectively hinder due to the restriction of using vast amount of toxic Pb in industrial production. According to the U.S. EPA, the maximum limit for Pb^{2+} content in air and water were set to 0.15 μg L^{-1} and 15 μg L^{-1} respectively.[17] Pb^{2+} in PbI_2, which is the decomposition product of perovskites, has a larger solubility (K_{sp}) on the order of 1×10^{-8} than the Cd^{2+} in toxic CdTe solar cells, K_{sp} on the order of $\approx 1 \times 10^{-22}$.[18] This makes Pb-based PSCs higher toxic than CdTe solar cells. The easy solubility of perovskite bears the risk of leakage into the environment by rain water and have vast impact on environment and nature surrounding us. With these potential exposure risk of vast amount of Pb to environment from PSCs, prior to commercialization, it is important to replace the toxic Pb in PSCs with non-toxic alternative materials.

1.4 Substituent of Pb in Perovskite Solar Cells

As a substituent of Pb^{2+}, the other environmentally friendly cations such as germanium (II) (Ge^{2+}), tin (II) (Sn^{2+}), cupper (II) (Cu^{2+}), and bismuth (III) (Bi^{3+}) have been explored in PSCs.[19-22] However, realizing the beneficial aspects and successful implementation of these non-toxic perovskite absorbers with non-toxic metals have seen limited success. Due to the similar group element to Pb, Sn has been extensively considered as an alternative of toxic Pb-based perovskite. Besides, similar atomic radius of Pb (1.4 Å) and Sn (1.35 Å), both elements have identical inactive outer shell orbitals. These similar features of Pb and Sn, encourages substitution of Pb by Sn without perturbating the favorable optoelectronic properties. Moreover, the theoretical limits for Sn-based PSCs is about 32.91% which is higher than Pb-based PSCs (30.14%) due to their optimum band gap in the range of 1.1 eV to 1.4 eV.[23] The table 1.4 shows the comparative physical properties between Sn and Pb based perovskite films. Although the Sn-based perovskites have similar or even superior optoelectronic properties but the PCE of Sn-based PSCs are far below the Pb-based counterpart.[24-25] This is because, the Sn based perovskites are suffered from some fundamental limitations.

I. Difficult to synthesize uniform and fully covered Sn-based thin films without additives due to the rapid crystallization of perovskite at room temperature.

II. The facial tendency to oxidation from Sn^{2+} to Sn^{4+} when exposed in air or even in glove box with a trace amount of water or oxygen.

III. Lack of energy levels matching among the existing ETL and HTL with the Sn-based perovskite materials.

Table 1.4: comparison of physical properties between Sn and Pb based perovskite films

Properties	Sn-based perovskite	Pb-based Perovskite
Band gap (eV)	~1.2-1.4	~1.6-1.8
Electron mobility ($cm^2V^{-1}s^{-1}$)	~2000	~60
Electron diffusion coefficient (cm^2s^{-1})	~1.28 ± 0.73	~0.036
Diffusion length (nm)	~500	~8000
Absorption coefficient (cm^{-1})	~10^4	~10^5

1.5 Stability of Perovskite Solar Cells

Over the past several years, the efficiency of PSCs has reached to the values that are competitive with the commercially established photovoltaic technologies. However, to be commercialized, any solar cell must have to go through the operational stability along with inexpensive fabrication technology and high PCE. The easy and low-cost fabrication techniques with high PCE have already made PSCs as potential price competitive candidate. However, for commercial products such as solar panels, the solar cell must have to sustain at least one decade regardless how inexpensive the fabrication process. This arise the question whether the PSCs can even meet the stability standard of commercial requirement. Initially most of the researches were focused mainly on the improvement of PCE but now a lot of attention has been paid on the stability issues. In general, the stability of PSCs cab be categorized into three classes such as extrinsic stability, device structure and intrinsic stability of perovskite materials.

The factors influence the extrinsic stability are moisture, oxygen, and ultraviolet light etc. which can be eliminated by simply employing suitable encapsulation. As no encapsulation is perfect so these extrinsic factors limit the lifetime of PSCs. To exclude these extrinsic factors, throughout this work the encapsulation for PSCs were performed inside the N_2 fill glove box.

The device architecture has a significant effect on the stability of PSCs. This effect much pronounced for Sn-based PSCs. For example, X. W. Sun et al. has demonstrated that the regular structure suffered from the poor reproducibility and stability due the deposition of hole transporting material on perovskite film which contain different types of dopant.[29] To get ride from this effect, in this work all the devices were fabricated in the inverted structure.

The intrinsic stability is the properties of perovskite itself. The stability of PSCs mainly depends on the stability of perovskite layer. The perovskite materials are sensitive to the oxygen and moisture. Upon exposure to the moisture and oxygen, perovskite dissociates into its metal halide and readily dissolve in water. For films, the stability depends on morphology and crystallinity of perovskite. The highly crystalline and pin-hole free uniform usually shows higher stability. The effects of morphology and crystallinity on the device performance and stability for Pb-based PSCs have been mentioned in chapter 2 and chapter 3. Due to the facial

tendency to oxidation and difficultly to fabricate uniform films, Sn-based PSCs are much unstable as compare with Pb-based PSCs. In this thesis work, the coadditive engineering has been performed for Sn-based PSCs as mentioned in chapter 3 and chapter 4.

1.6 Aim of the Thesis

To improve the perovskite film quality, several fabrication methods have been developed and among them, ASD has been widely used for the fabrication of highly efficient PSCs. The success of ASD method is mainly dependent on the selection and dripping time of anti-solvent. In this regard, Xiao et al. used twelve different anti-solvents to induce crystallization of $MAPbI_3$ perovskite and find out four suitable anti-solvents for uniform film morphology.[30] Recently, Paek et al. performed a thorough study on six commonly used anti-solvents to evaluate the best one in term of device performance.[31]However, in all these conducted studies, they have failed to focus on the most crucial stability factor variation with anti-solvents. Hence, to further advance the development of PSCs, investigating the roles of various anti-solvents on the morphology of perovskite films for stable device performance is urgently needed which has not explored yet.

Therefore, in this study, the effect of different anti-solvents on the stability of PSCs have been observed. The suitable anti-solvents have been identified from the perspective of performance and light soaking stability.

In ASD method, to obtain uniform film with optimum optoelectronic properties, usually a mixed of solvents such as DMF and DMSO or DMF and GBL is used. The role of this mixed solvent is to slow down the perovskite crystallization rate by forming a complex compound before final perovskite film formation. However, a single solvent with medium boiling point for the perovskite precursor system is more beneficial for large scale fabrication. But the perovskite films fabricated from ASD method in single solvent system, are suffered from inferior structural and optoelectronic properties.

Therefore, to optimize the single solvent ASD method, an additive engineering with $CuCl_2$ has been performed. Detail morphological, structural and optoelectronic characterization have been performed to observe the effects of $CuCl_2$ addition on perovskite film.

Although the PSCs shows PCE above 23% but the presence of toxic of Pb in PSCs effectively hinders their commercial applications.[16] Due to the similar or even superior optoelectronic properties of Sn based perovskite, it has been considered as the alternative of Pb. However, Sn-based perovskite compounds implemented in PSCs show poor photovoltaic performance. This is because Sn-based perovskite is suffered from some fundamental problems such as facial tendency to oxidation from Sn^{2+} to Sn^{4+} and inability to form pin-holes free uniform films. To retard the oxidation of Sn^{2+}, Mathews et al. were used SnF_2 as additive which is now considered as an essential element for fabrication of uniform perovskite films.[32] Later it has been observed that suppression Sn^{2+} oxidation is not enough only by SnF_2 and other reducing agents are necessary to overcome the issue arisen. But a negative impact has been observed on the morphology with the addition of another reducing agent. So, the addition of a secondary additive with suitable functionality which can simultaneously assist to form a uniform film and retard the Sn^{2+} oxidation might be beneficial.

Therefore, in this thesis, the effects of coadditive with dual beneficial aspects for uniform Sn-based perovskite film growth with controlled rate and effective suppression of Sn^{2+} oxidation have been observed. To do this, the Sn-based perovskite films were fabricated by the ASD method that was optimized during the Pb-based work. A detail morphological, structural and optoelectronic characterization have been performed for the fabricated perovskite films. In addition, the effects of coadditive on the performance of PSCs have also been observed. However, the Sn-based PSCs suffered from light soaking stability which is needed to overcome for real life applications.

To enhance the stability of Sn-based PSCs, several attempts have been performed such as partial substitution of MA^+ by FA^+, I^- by Br^-, introduction of 2D/3D composite perovskite concept from Pb-based PSCs etc. But till now, the maximum reported stability is only 1h under operational condition at maximum power point tracking condition (MPPT). However, long carbon chain molecules with bifunctional groups at the two ends are well known for their dual beneficial aspects for Pb-based such as cross-linking adjacent grains through hydrogen bond formation and forming an inert passive layer on the surface.[33-34] So, this type of additives might be useful for Sn-based PSCs to simultaneously enhance the performance and stability of Sn-based PSCs.

Therefore, in this studied, the effects bifunctional additive with long carbon chain molecule on the passivation of grain boundaries, film formation, and crystallinity, as well as on the device performance and stability of Sn-based PSCs have been observed. This is done by the detail characterization of the fabricated perovskite films and corresponding PSCs.

References

(1) Atehmengo, N., Idika, I. K., Shehu, A., & Ibrahim, R. Climate Change/Global Warming and its Impacts on Parasitology/Entomology. *Parasitology*, **2014** ,5, 1-11.

(2) Heidari, N.; Pearce, J. M. A Review of Greenhouse Gas Emission Liabilities as The Value of Renewable Energy for Mitigating Lawsuits for Climate Change Related Damages. *Renew. Sustain. Energy Rev.* **2016,** *55*, 899-908.

(3) Mathiesen, B. V.; Lund, H.; Connolly, D.; Wenzel, H.; Østergaard, P. A.; Möller, B.; Nielsen, S.; Ridjan, I.; Karnøe, P.; Sperling, K. Smart Energy Systems for Coherent 100% Renewable Energy and Transport Solutions. *Appl. Energy* **2015,** *145*, 139-154.

(4) Chen, S.; Hou, Y.; Chen, H.; Tang, X.; Langner, S.; Li, N.; Stubhan, T.; Levchuk, I.; Gu, E.; Osvet, A. Exploring the stability of novel wide bandgap perovskites by a robot based high throughput approach. *Advanced Energy Materials* **2018,** *8*, 1701543.

(5) Lewis, N. S. Toward Cost-Effective Solar Energy Use. *science* **2007,** *315*, 798-801.

(6) Jacobsson, T. J.; Pazoki, M.; Hagfeldt, A.; Edvinsson, T. Goldschmidt's Rules and Strontium Replacement in Lead Halogen Perovskite Solar Cells: Theory and Preliminary Experiments on $CH_3NH_3SrI_3$. *J. Phys. Chem. C,* **2015,** *119*, 25673-25683

(7) Navas, J.; Sánchez-Coronilla, A.; Gallardo, J. J.; Martín, E. I.; Hernández, N. C.; Alcántara, R.; Fernández-Lorenzo, C.; Martín-Calleja, J. Revealing the Role of Pb^{2+} in the Stability of Organic–Inorganic Hybrid Perovskite $CH_3NH_3Pb_{1-x}Cd_xI_3$: an experimental and theoretical study. *Phys. Chem. Chem. Phys* **2015,** *17,* 23886-23896.

(8) Fan, Z.; Sun, K.; Wang, J. Perovskites for Photovoltaics: a Combined Review of Organic–Inorganic Halide Perovskites and Ferroelectric Oxide Perovskites. *J. Mater. Chem. A,* **2015,** *3,* 18809-18828.

(9) De Wolf, S.; Holovsky, J.; Moon, S.-J.; Löper, P.; Niesen, B.; Ledinsky, M.; Haug, F.-J.; Yum, J.-H.; Ballif, C. Organometallic Halide Perovskites: Sharp Optical Absorption Edge and its Relation to Photovoltaic Performance. *J. Phys. Chem. Lett.*, **2014,** *5*, 1035-1039.

(10) Jensen, N.; Hausner, R.; Bergmann, R.; Werner, J.; Rau, U. Optimization and Characterization of Amorphous/Crystalline Silicon Heterojunction Solar Cells. *Prog. Photovolt.: Res. Appl.,***2002,** *10*, 1-13.

(11) Giebink, N. C.; Wiederrecht, G. P.; Wasielewski, M. R.; Forrest, S. R. Thermodynamic Efficiency Limit of Excitonic Solar Cells. *Phys. Rev. B,* **2011,** *83,* 195326.

(12) Hu, M.; Bi, C.; Yuan, Y.; Xiao, Z.; Dong, Q.; Shao, Y.; Huang, J. Distinct Exciton Dissociation Behavior of Organolead Trihalide Perovskite and Excitonic Semiconductors Studied in the Same System. *Small* **2015,** *11*, 2164-2169.

(13) Xing, G.; Mathews, N.; Sun, S.; Lim, S. S.; Lam, Y. M.; Grätzel, M.; Mhaisalkar, S.; Sum, T. C. Long-Range Balanced Electron-and Hole-Transport Lengths in Organic-Inorganic $CH_3NH_3PbI_3$. *Science* **2013,** *342,* 344-347.

(14) Giorgi, G.; Fujisawa, J.-I.; Segawa, H.; Yamashita, K. Small Photocarrier Effective Masses Featuring Ambipolar Transport in Methylammonium Lead Iodide Perovskite: a Density Functional Analysis. *J. Phys. Chem. Lett.,***2013,** *4*, 4213-4216.

(15) Heo, J. H.; Im, S. H.; Noh, J. H.; Mandal, T. N.; Lim, C.-S.; Chang, J. A.; Lee, Y. H.; Kim, H.-j.; Sarkar, A.; Nazeeruddin, M. K. Efficient Inorganic–Organic Hybrid Heterojunction Solar Cells Containing Perovskite Compound and Polymeric Hole Conductors. *Nat. Photonics,* **2013,** *7*, 486.

(16) Green, M. A.; Hishikawa, Y.; Dunlop, E. D.; Levi, D. H.; Hohl-Ebinger, J.; Ho-Baillie, A. W. Y. Solar Cell Efficiency Tables (version 51). *Prog Photovolt Res Appl.* **2018,** *26*, 3-12.

(17) Fewtrell, L., Kaufmann, R. & Prüss-Üstün, A. *Lead:* Assessing The Environmental Burden of Disease at National and Local Levels (World Health Organization, **2003**).

(18) Zayed, J.; Philippe, S. Acute Oral and Inhalation Toxicities in Rats with Cadmium Telluride. *Int. J. Toxicol.,* **2009,** *28*, 259-265.

(19) Chung, I.; Song, J.-H.; Im, J.; Androulakis, J.; Malliakas, C. D.; Li, H.; Freeman, A. J.; Kenney, J. T.; Kanatzidis, M. G. $CsSnI_3$: Semiconductor or Metal? High Electrical Conductivity and Strong Near-Infrared Photoluminescence from a Single Material. High hole mobility and phase-transitions. *J. Am. Chem. Soc.* **2012,** *134*, 8579-8587.

(20) Cortecchia, D.; Dewi, H. A.; Yin, J.; Bruno, A.; Chen, S.; Baikie, T.; Boix, P. P.; Grätzel, M.; Mhaisalkar, S.; Soci, C. Lead-Free $MA_2CuCl_xBr_{4-x}$ Hybrid Perovskites. *Inorg. Chem.* **2016,** *55*, 1044-1052.

(21) Krishnamoorthy, T.; Ding, H.; Yan, C.; Leong, W. L.; Baikie, T.; Zhang, Z.; Sherburne, M.; Li, S.; Asta, M.; Mathews, N. Lead-Free Germanium Iodide Perovskite Materials for Photovoltaic Applications. *J. Mater. Chem A* **2015,** *3*, 23829-23832.

(22) Slavney, A. H.; Hu, T.; Lindenberg, A. M.; Karunadasa, H. I. A Bismuth-Halide Double Perovskite with Long Carrier Recombination Lifetime for Photovoltaic Applications. *J. Am. Chem. Soc.* **2016,** *138*, 2138-2141.

(23) Rühle, S. Tabulated Values of The Shockley–Queisser Limit for Single Junction Solar Cells. *Solar Energy* **2016,** *130*, 139-147.

(24) Noel, N. K.; Stranks, S. D.; Abate, A.; Wehrenfennig, C.; Guarnera, S.; Haghighirad, A.-A.; Sadhanala, A.; Eperon, G. E.; Pathak, S. K.; Johnston, M. B. Lead-Free Organic–Inorganic Tin Halide Perovskites for Photovoltaic Applications. *Energy Environ. Sci.* **2014,** *7*, 3061-3068.

(25) Shao, S.; Liu, J.; Portale, G.; Fang, H. H.; Blake, G. R.; ten Brink, G. H.; Koster, L. J. A.; Loi, M. A. Highly Reproducible Sn-Based Hybrid Perovskite Solar Cells with 9% Efficiency. *Adv. Energy Mater.* **2018,** *8*, 1702019

(26) Kojima, A.; Teshima, K.; Shirai, Y.; Miyasaka, T. Organometal Halide Perovskites as Visible-Light Sensitizers for Photovoltaic Cells. *J. Am. Chem. Soc.* **2009,** *131*, 6050-6051.

(27) Tress, W.; Marinova, N.; Inganäs, O.; Nazeeruddin, M. K.; Zakeeruddin, S. M.; Graetzel, M. In the Role of The Hole-Transport Layer in Perovskite Solar Cells-Reducing Recombination and Increasing Absorption, PVSC, 2014 IEEE 40th, IEEE: **2014**, 1563-1566.

(28) Bi, D., Yang, L., Boschloo, G., Hagfeldt, A., & Johansson, E. M. (). Effect of Different Hole Transport Materials on Recombination in $CH_3NH_3PbI_3$ Perovskite-Sensitized Mesoscopic Solar Cells. *J. Phys. Chem. Lett*, **2013**,*4*, 1532-1536.

(29) Hao, F.; Stoumpos, C. C.; Cao, D. H.; Chang, R. P.; Kanatzidis, M. G. Lead-Free Solid-State Organic–

Inorganic Halide Perovskite Solar Cells. *Nat. Photonics,* **2014,** *8*, 489.
(30) M. Xiao, F. Huang, W. Huang, Y. Dkhissi, Y. Zhu, J. Etheridge, A. Gray-Weale, U. Bach, Y.B. Cheng, L. Spiccia, A Fast Deposition-Crystallization Procedure for Highly Efficient Lead Iodide Perovskite Thin-Film Solar Cells, Angew. Chem., **2014**, 126, 10056-10061.
(31) S. Paek, P. Schouwink, E.N. Athanasopoulou, K. Cho, G. Grancini, Y. Lee, Y. Zhang, F. Stellacci, M.K. Nazeeruddin, P. Gao, From Nano-to Micrometer Scale: The Role of Antisolvent Treatment on High Performance Perovskite Solar Cells, Chem. Mater., **2017**, 29, 3490-3498.
(32) Kumar, M. H.; Dharani, S.; Leong, W. L.; Boix, P. P.; Prabhakar, R. R.; Baikie, T.; Shi, C.; Ding, H.; Ramesh, R.; Asta, M. Mathews, N. Lead‐Free Halide Perovskite Solar Cells with High Photocurrents Realized Through Vacancy Modulation. *Adv. Mater.* **2014,** *26*, 7122-7127.
(33) Grancini, G.; Roldán-Carmona, C.; Zimmermann, I.; Mosconi, E.; Lee, X.; Martineau, D.; Narbey, S.; Oswald, F.; De Angelis, F.; Graetzel, M. One-Year Stable Perovskite Solar Cells by 2D/3D Interface Engineering. *Nat. Commun.* **2017,** *8*, 15684.
(34) Li, X.; Dar, M. I.; Yi, C.; Luo, J.; Tschumi, M.; Zakeeruddin, S. M.; Nazeeruddin, M. K.; Han, H.; Grätzel, M. Improved Performance and Stability of Perovskite Solar Cells by Crystal Crosslinking with Alkylphosphonic Acid ω-Ammonium Chlorides. *Nat. Chem.* **2015,** *7*, 703-711.

Chapter 2

Influence of Anti-Solvents on $CH_3NH_3PbI_3$ Films Surface Morphology for Fabricating Efficient and Stable Inverted Planar Perovskite Solar Cells

2.1 Introduction

Perovskite solar cells (PSCs) have attracted tremendous attention due to the favorable photovoltaic properties of perovskite compound such as- tunable optical band gap, high molar extinction coefficient, broad absorption spectrum, high charge carrier mobility, and ambipolar charge transport capability.[1-7] Since the introduction of PSCs, it has seen rapid improvement in power conversion efficiency (PCE) from 3.8% to 22.1% within few years.[8-12] Besides, the unique properties of perovskite compounds, the development of various device structures and versatile fabrication processes of high quality perovskite film growth are the key factors for achieving high performance .[13] Among existing various PSC structures, the inverted planar structure (p-i-n) has been identified as a promising candidate.[14,15] Generally, in a p-i-n PSC, a p type semiconducting material is deposited on top of the transparent conductive oxide glass followed by perovskite compound as the light absorber and n -type semiconducting material as the electron transport layer. In a PSC, light is absorbed by the perovskite absorber result in an efficient electron-hole pair generation to produce photovoltaic effect, which makes the morphology of the perovskite film an important factor. For deposition of a homogeneous and compact perovskite layer, several fabrication methods have been developed such as- one step spinning, two step dipping, single source evaporation, dual sources evaporation method, and one step anti-solvent dripping (ASD) method.[7,16-19] Among the existing processes, the ASD method has been extensively used for the fabrication of the perovskite layer due to their enhanced capability of forming high quality perovskite crystals.[20,21] Generally, high boiling point solvents - N, N-dimethylformamide (DMF), dimethyl sulfoxide (DMSO), gamma-butyrolactone or combination of two solvents are used to dissolve the perovskite precursor materials.[22,23] However, only spin-coating of the precursor solution does not yield homogeneous and uniform perovskite layer with crystalline properties.[24] ASD method was developed in 2014 by Jeon et al. highlighted that, formation of a dense and uniform perovskite layer can be anticipated by forming stable CH_3NH_3Br-PbI_2-DMSO intermediate phase and dripping with toluene as anti-solvent during the spin-coating process.[19] At present, the ASD method has been used by numerous groups to fabricate perovskite absorber layers with recorded PCEs in PSCs.[10,25-27] Dripping certain amount of anti-solvents during the spin coating of perovskite layer speeds up the heterogeneous nucleation by forming a local super-saturation of precursor solution on the spinning perovskite deposited substrate. To understand the effect of different anti-solvents on the perovskite

films morphology, Xiao et al. used 12 different anti-solvents to fabricate perovskite film.[28] They observed that, the anti-solvents such as 2-propanol and chloroform produced non-uniform central area in the perovskite absorber film whereas the chlorobenzene, benzene, xylene and toluene anti-solvents formed uniform film over the entire substrate. Ahn et al. used diethyl ether to selectively remove the DMSO from the spinning solution containing equimolar CH_3NH_3I (MAI), PbI_2, and DMSO which led them to fabricate PSCs with PCE as high as 18.3%.[20] In a recent work, Paek et al. have conducted a thorough study on six anti-solvents for mesoporous PSCs to evaluate the best anti-solvent from the PCE perspective.[29] However, all the studies conducted regarding anti-solvent has failed to reveal the most crucial factor of stability which is one of the key aspects for the development of PSC. Hence, understanding the effects of various anti-solvents on the morphology of perovskite films for designing stable PSCs has remained a challenge for further development.

Here in this work, the effects of four anti-solvents such as- toluene, chlorobenzene, *p*-xylene and ether on the film formation of high quality perovskite absorbers and their stability in p-i-n PSCs have been studied. The stability performances both in dark and under air mass (AM) 1.5G sunlight conditions have been observed. The effects of different ASD on the morphology of perovskite films and corresponding electrical behaviors of p-i-n PSCs have also been observed. This study reveals the inter-relation between the morphology of aforementioned ASD treated perovskite layer with their corresponding long-term stability in PSCs. From the conducted experiments and analysis, it has been highlights that, toluene and chlorobenzene anti-solvent treated PSCs are highly efficient with stable performances in dark and standard AM 1.5G sunlight condition for 30 days.

2.2 Experimental Procedures

2.2.1 Materials

In this work. all the chemical used as received without any further purification, including PbI_2 (99%, Sigma–Aldrich), MAI (> 98%, Tokyo Chemical Industry Co., Japan), Nickel acetylacetonate (95%, Sigma–Aldrich), PCBM (Phenyl-C61-butyric acid methyl ester) (99.5%, Lumtec Co., Taiwan). Magnesium acetatetetrahydrate (99%), Bathocuproine (BCP) and super dehydrated solvents of DMF, DMSO, toluene, chlorobenzene, *p*-xylene, ether, acetonitrile, methanol and ethanol, were all purchased from Wako Co., Japan.

2.2.2 Perovskite Film Fabrication

The precursor solution for $CH_3NH_3PbI_3$ perovskite film was obtained by mixing equaimolar ratio of (1.2 mmol) PbI_2 and MAI in 1.8 mL of DMF and DMSO (4:1) mixed solvent. The perovskite film was deposited by spin-coating 70 μL of precursor solution at 5000 rpm for 42 s. During spin-coating, an optimum amount of anti-solvent was dripped on the substrate after 17 s. Four different anti-solvents such as toluene (100 μL), chlorobenzene (100 μL), p-xylene (100 μL) and ether (100 μL) has been used. The spin-coated films were then annealed at 100 °C for 30 min.

2.2.3 Solar Cell Fabrication

PSCs were fabricated on the patterned fluorine doped tin oxide (FTO) coated glass substrates. The substrates were ultrasonically cleaned with detergent, deionized water, acetone, and ethanol respectively for 15 min each. The cleaned substrates were treated with ultraviolet/ ozone radiation for 30 min. The NiO_X layer was deposited on to the FTO substrate by spraying a solution of nickel acetylacetonate and magnesium acetate tetrahydrate in acetonitrile/ethanol (with 95:5%V) at 570 °C. The NiO_X films were then annealed at 570 °C for 15 min and cooled down to room temperature. After cooling at room temperature, the substrates were transferred to glove box and the $CH_3NH_3PbI_3$ perovskite films were deposited. An electron transporting layer PCBM (20 mg mL^{-1} in chlorobenzene) and BCP (saturated solution in methanol) were deposited by spin-coating at 1000 rpm for 30 s and 6000 rpm for 30 s respectively. Finally, a 90 nm thick silver layer was vacuum deposited through a shadow mask with an active area of 1.02 cm^2. For PSC sealing, the front active area of FTO was sandwiched by a cavity glass using UV glue.

2.2.4 Characterization

The ultraviolet visible (UV–Vis) spectra were measured by a Shimadzu UV/Vis 3600 spectrophotometer. Scanning electron microscope (SEM) images were obtained by using a JSM-6500F field-emission scanning electron microscope under an acceleration voltage of 5 kV. The atomic force microscopy (AFM) measurements were performed by using JSPM - 5200 scanning probe microscope. The X-Ray Diffraction (XRD) was measured on a Rigaku MiniFlex600 powder X-ray diffractometer with 2 θ - θ geometry at a scanning rate of 1° min^{-1} using Cu-K_α radiation (1.5418 Å). The current density-voltage (J-V) characteristics were measured using a solar simulator with standard AM 1.5G sunlight (100mWcm^{-2}, WXS-155S-10: Wacom Denso Co., Japan) under ambient conditions with a humidity>70%. The J-V curves were measured by forward (−0.2 V to 1.2 V) or reverse (1.2 V to −0.2 V) scans by using the Keithley 2400 as a digital source meter. The step voltage was fixed at 10 mV and the delay time was set at 50 ms. J-V curves for all devices were measured by masking the cells with a metal mask 1.02 cm^2 in area. Monochromatic incident photon-to-current conversion efficiency (IPCE) spectra were measured with a monochromatic incident light of 1×10^{16} photons cm^2 in direct current mode (CEP-2000BX, Bunkoukeiki Co., LTD). The light intensity of the solar simulator was calibrated by a standard silicon solar cell. The light soaking stability was tested on a solar cell light resistance test system (Model BIR-50, Bunkoukeiki Co., LTD) equipped with a Class AAA solar simulator;<420 nm ultraviolet light was cut off with an optical filter.

2.3 Results and discussion

2.3.1 Perovskite Films Formation

The principle of solvent / anti-solvent crystallization is by rapid precipitation of super saturation level which leads to the formation of small crystals. In solvent / anti-solvent crystallization, this reduction in solubility is achieved by using an anti-solvent. The super saturation level depends on the miscibility of anti-solvent with the solvent. In the process of ASD method, the anti-solvents are used for creating local super saturation in the precursor solution. With these principles of miscibility and immiscibility, different type of anti-solvents such as toluene, chlorobenzene (miscible both in DMF and DMSO), ether (miscible only in DMF) and *p*-xylene (immiscible both in DMF and DMSO) have been selected to this experiment. To find out the effect of miscibility of anti-solvents into the solvents for the fabrication of perovskite films, the change of color of the perovskite films has been observed immediately after anti-solvent treatment (Figure 2.1a), after annealing at 100 °C for 5 s (Figure 2.1b) and after annealing at 100 °C for 10 min (Figure 2.1c).

Figure 2.1. Photographic images of perovskite films formed by chlorobenzene, toluene, ether and *p*-xylene ASD treatment; (a) immediatly after anti-solvent treatment, (b) after 5 s annealing at 100 ^{0}C and (c) after 10 min annealing at 100 ^{0}C.

From figure 2.1, it was observed that immediatly after chlorobenzene dripping, the perovskite containing substrate changed to brown and toluene dripped perovskite films turned to light brown from light yellow color. Whereas, the ether and *p*-xylene treated perovskite films remained light yellow color. After 5 sec annealing at 100 ^{0}C, chlorobenzene and toluene dripped perovskite films turned homogeneous dark brown whereas the ether treated film formed dark brown color with light brown circle at the center. The *p*-xylene treated film formed inhomogeneous light brown color. The variation of colors is expected due to the degree of anti-solvent ability which depends on the miscibility of anti-solvents into the solvents. As the *p*-xylene is immiscible both in DMF and DMSO with lowest crystallization rate, hence the change of color is the slowest for this ASD.

But after 10 min annealing at 100 ^{0}C all films turned to shiny black (Figure 2.1c). For toluene and chlorobenzene dripping, homogeneous perovskites were formed whereas the ether and *p*-xylene treatment formed inhomogeneous films with circle at the center of the substrate (Figure S2.1).

The UV-vis absorption spectra of $MAPbI_3$ perovskite layers fabricated using toluene, chlorobenzene, *p*-xylene and ether ASD treatment are shown in Figure 2.2a. The absorption spectra of toluene, chlorobenzene, *p*-xylene and ether treated perovskite films overlap with each other. All the films exhibited similar absorption band edge at 780 nm, which corresponds the band gap excitation of $MAPbI_3$ perovskite material. The optical bandgap, E_g of the $MAPbI_3$ compound was determined from diffuse reflectance measurements (Figure 2.2b). The optical absorption coefficient (α/S) was calculated using reflectance data according to the Kubelka–Munk equation, $\alpha/S = [(1\text{-}R)^2]/2R$, where R is the percentage of reflected light, and α and S are the absorption and scattering coefficients respectively.[30] The band gap of $MAPbI_3$ perovskite layers formed with toluene, chlorobenzene, *p*-xylene and ether ASD were 1.61 eV each.

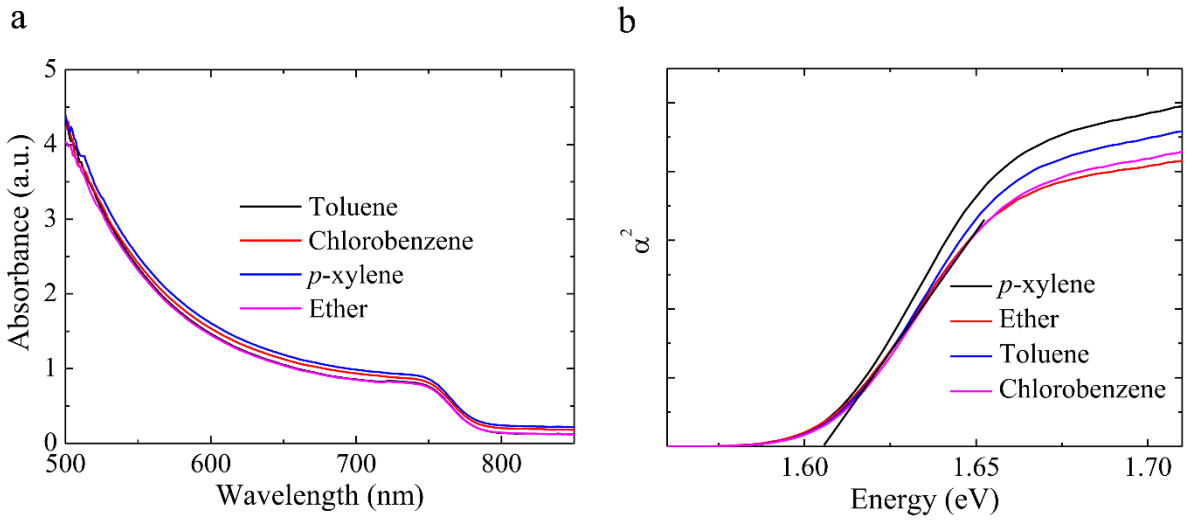

Figure 2.2. (a) UV-vis absorbance spectra and (b) absorption coefficient of $MAPbI_3$ films fabricated using toluene, chlorobenzene, *p*-xylene and ether anti-solvents.

XRD characterization was performed on the fabricated perovskite layers to investigate the crystal structure of materials formed by different anti-solvents treatment and has been shown in figure 2.3a. From the diffraction pattern, three clear peaks were observed at 14.08 ^{0} , 28.40 ^{0} and 31.83 ^{0} which were represented by (110), (220) and (310) planes respectively indicating the formation of tetragonal $CH_3NH_3PbI_3$.[31-34] These diffraction patterns show no peaks corresponding to the PbI_2 or CH_3NH_3I compounds which indicates the full conversion of $CH_3NH_3PbI_3$. XRD patterns of perovskite films fabricated by different anti-solvents revealed that the formation of tretragonal $CH_3NH_3PbI_3$ were independent of aforemensioned ASD treatments. After continuous illumination for 30 days under standard AM 1.5 sunlight (100 mW cm^{-2}) and relative humidity of >70 %, XRD measurement was performed to evaluate the stability of perovskite films (Figure 4.3b). The XRD patterns for the toluene and chlorobenzene ASD treated perovskite films showed no new peaks indicating

that these films were stable under 30 days continuous light soaking. On the other hand, for the *p*-xylene treated perovskite film, a new peak at 12.72 ^{0} which can be assigned for the PbI_2 has been observed (Figure 2.3b).[35] This result indicate that the *p*-xylene ASD treated perovskite films decomposed during the light soaking period.

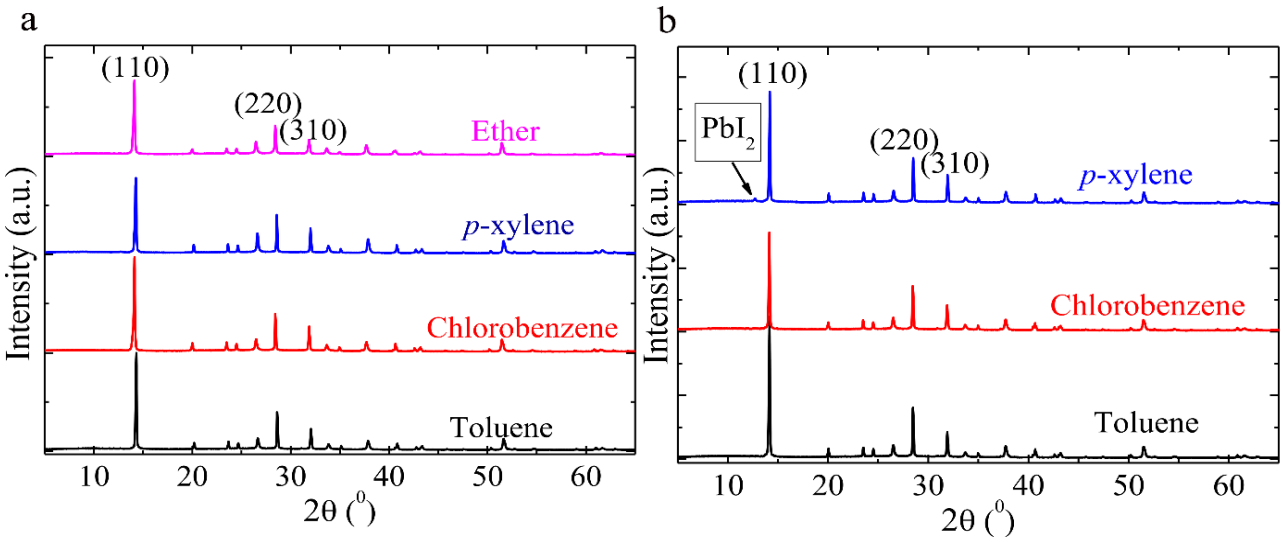

Figure 2.3. XRD patterns of $MAPbI_3$ fabricating by using toluene, chorobenzene, *p*-xylene and ether anti-solvents (a) fresh (b) after 30 days ligh soaking.

The AFM measurment has been peroformed to measure the roughness of the $MAPbI_3$ films treated with toluene, chlorobenzene, *p*-xylene and ether anti-solvents. From the calculation of root mean-squared (R.M.S.) roughness, the R.M.S. values for $MAPbI_3$ films treated with toluene, chlorobenzene, *p*-xylene and ether were recorded at 14.7 nm, 12.4 nm, 19.6 and 43.6 nm respectively (Figure 2.4). The detail line profiles are given in the supporting inforamtion (Figure S2.2-2.5). The toluene, chlorobenzene and *p*-xylene treated films showed similar low roughness whereas the ether treatment produced comparatively rougher $MAPbI_3$ films. Similar trend has been observed by the Paek et al. in which the toluene, chlorobenzene, and *p*-xylene formed very smooth surface but the perovskite surface treated with ether resulted with the roughest surface .[29]

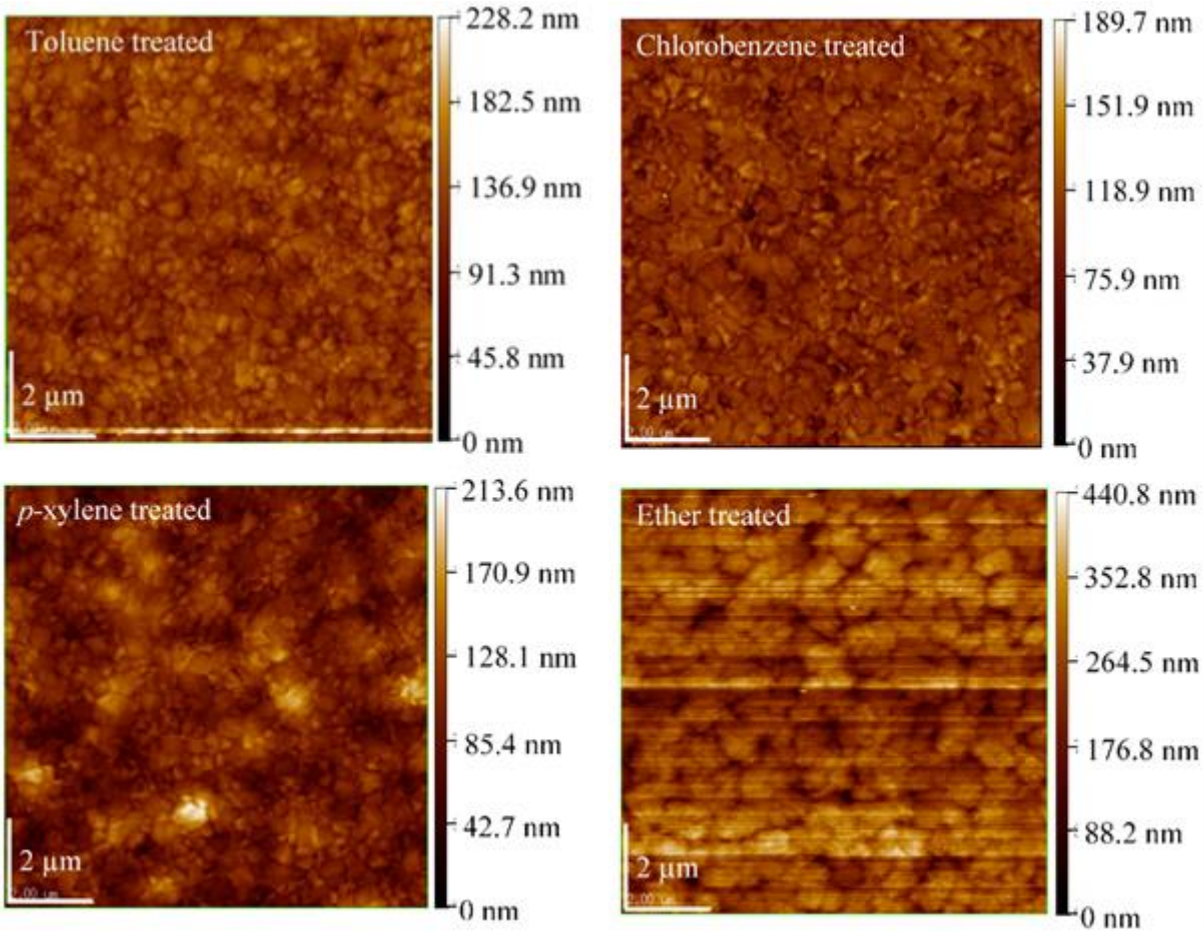

Figure 2.4. AFM images of perovskite films treated with toluene, chlorobenzene, *p*-xylene and ether. All the perovskite films has been deposited on NiOx substrates (area = 10 × 10 µm)

The perovskite films treated with different anti-solvents exhibited different morphologies. The effects of anti-solvent on the morphology and the structure of corresponding perovskite layers were characterized by SEM. Figure 2.5 shows the surface morphologies of perovskite films dripped with various types of anti-solvent. The toluene and chlorobenzene treated $MAPbI_3$ perovskite films were homogeneous and showed full coverage of the NiOx coated FTO substrate as shown in Figures 2.5a and 2.5b. Whereas the *p*-xylene treated film fully covered the substrate with inhomogeneous particle size (Figure 2.5c), the ether treatment formed aggregate of small grains, cracks and numerous pinholes throughout the whole film surface (Figure 2.5d). These results are in consistent with the AFM measurement results (Figure 2.4).

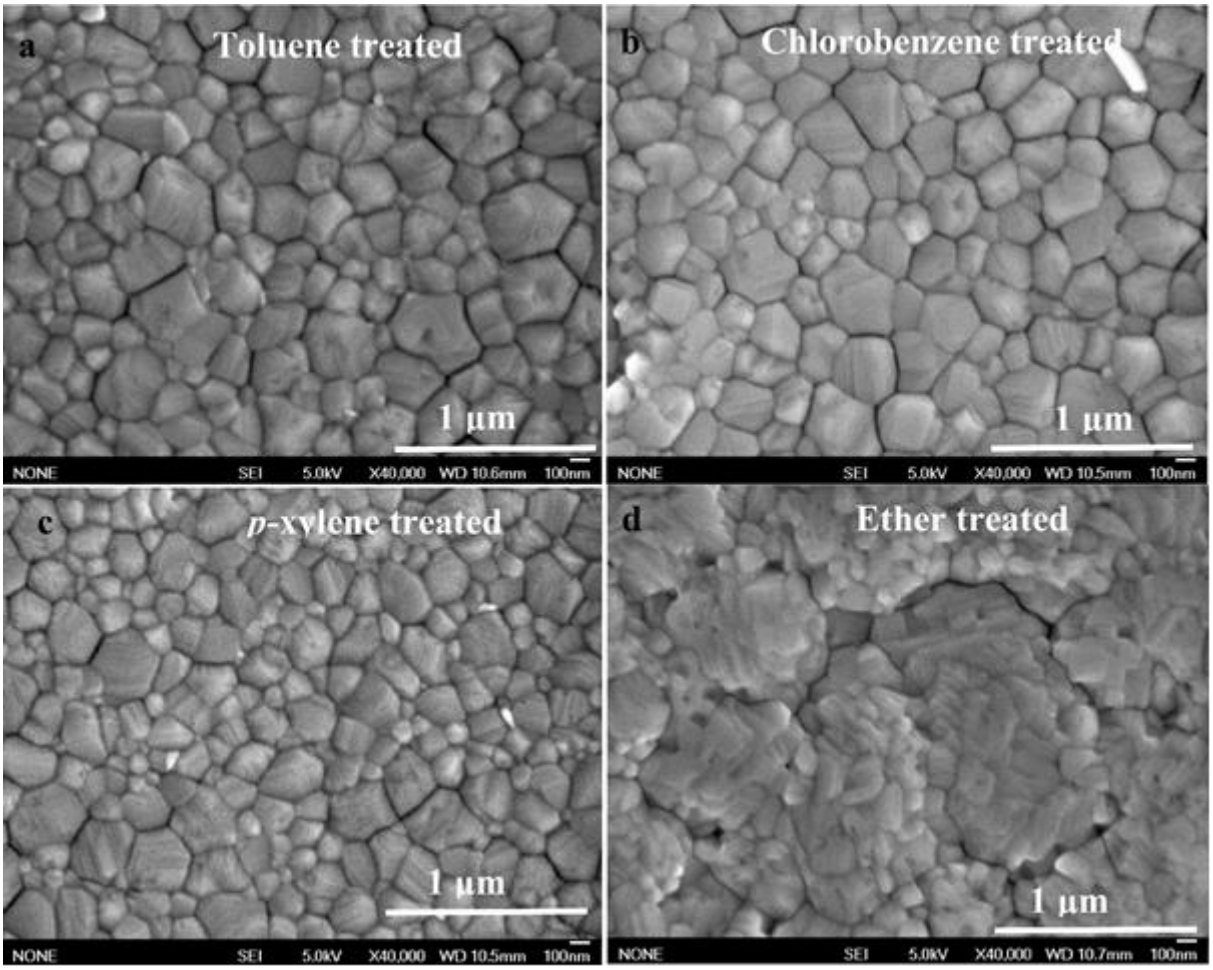

Figure 2.5. SEM images of $MAPbI_3$ films (top surface) formed by anti-solvents - (a) toluene, (b) chlorobenzene, (c) *p*-xylene and (d) ether.

To observe the grain structures of the $MAPbI_3$ layer, the cross-sectional images have been taken for the perovskite films fabricated by different anti-solvent treatment (Figure 2.6). From the cross sectional view, one important feature of grain structure with toluene, chlorobenzene and *p*-xylene dripped has been observed. These perovskite layers formed single grain structure through out the cross-section (Figures 2.6a, 2.6b and 2.6c). In this case, the grain boundaries were only in the vertical direction with no grain boundaries along the horizontal direction. The ether treated perovskite layer formed poly-grains with pinholes (Figure 2.6d).

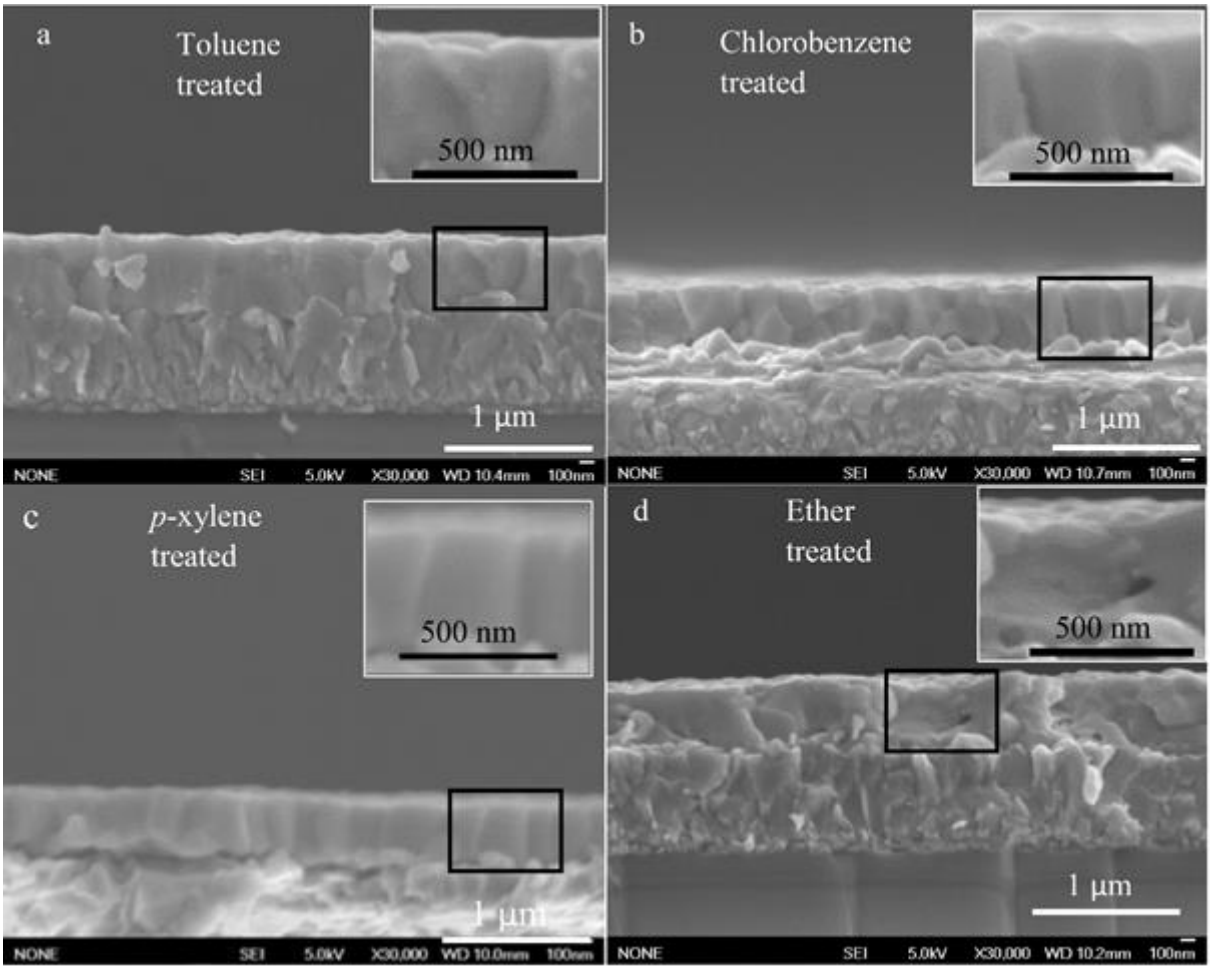

Figure 2.6. Cross-sectional SEM images of $MAPbI_3$ films formed by using (a) toluene, (b) chlorobenzene, (c) *p*-xylene and (d) ether. Inset shows the marked part of film cross section in higher magnification.

To observe the effect of light soaking on the grain structures, the cross-sectional SEM measurement on the same perovskite films after 30 days continuous light soaking have been performaed (Figure 2.7). From this measurment, it has been ovserved that the grain structures of toluene and chlorobenzene treated perovskite films remained unaffected even after 30 days light soaking (Figures. 2.7a and 2.7b). But for the *p*-xylene treated perovskite film, some white particles along the grain boundaries of perovskite film were observed after 30 days of light soaking (inset Figure 2.7c). The presence of these particles was not recorded at the initial cross-section observation (Figure 2.6c). These white particles might be PbI_2, as the decomposition product of $CH_3NH_3PbI_3$ after light soaking (Figure 2.3b). For ether treated perovskite film, the size and number of pores increased with light soaking time until the 5^{th} day (Figure 2.7d).

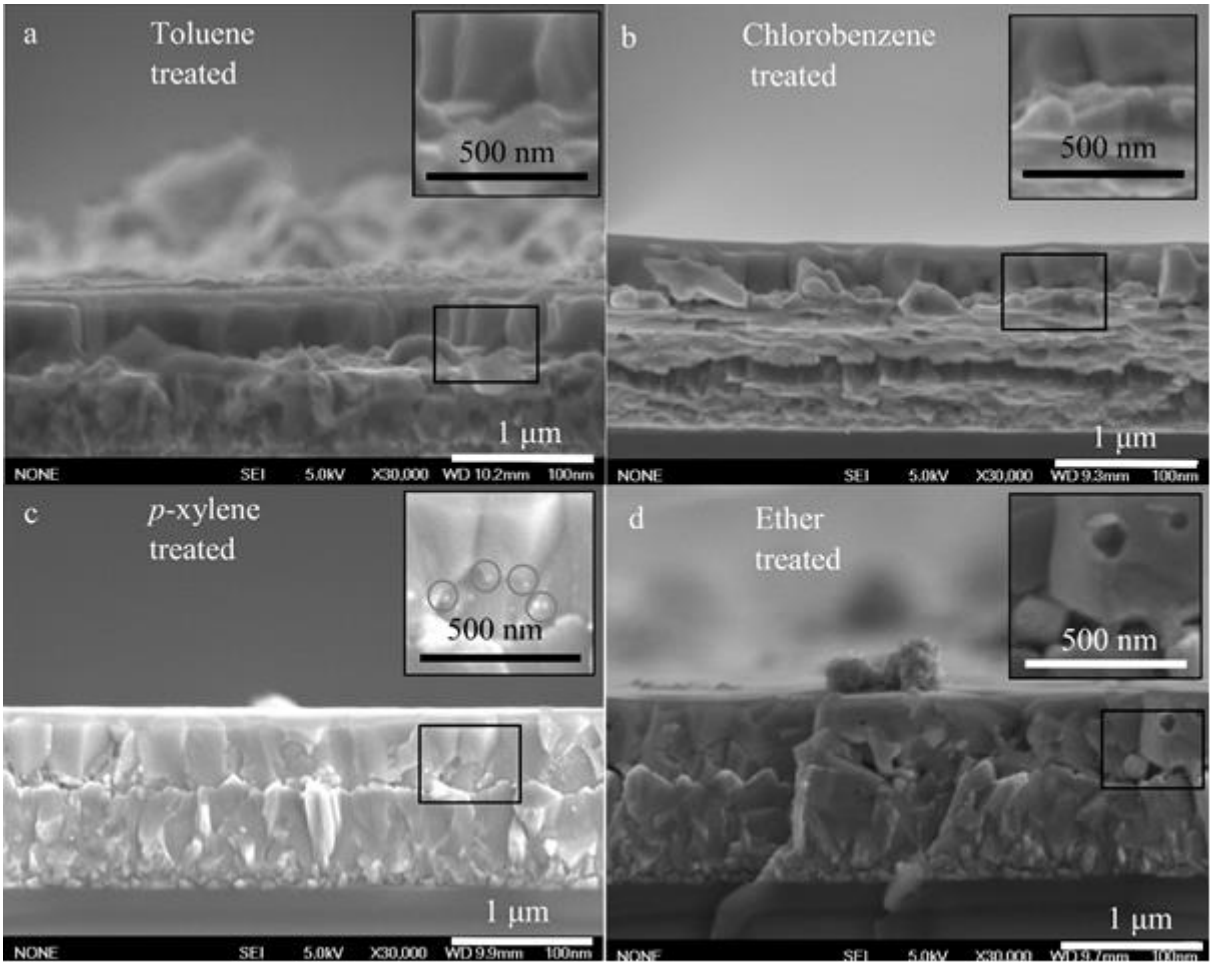

Figure 2.7. Cross-sectional SEM images of $MAPbI_3$ films formed by (a) toluene, (b) chlorobenzene, (c) *p*-xylene anti-solvents after 30 days light soaking and (d) ether anti-solvents after 5 days light soaking. Inset shows the marked part of film cross section in higher magnification.

2.3.2 Photovoltaic Performance

To observe the effects of anti-solvent treatment during the fabrication of perovskite films on the device performance, PSCs devices were fabricated with the corresponding films in FTO/NiOx/$MAPbI_3$/$PC_{61}BM$/BCP/Ag structure. Figure 2.8 shows the photovoltaic performances of corresponding PSCs fabricated with toluene, chlorobenzene, *p*-xylene and ether treated $MAPbI_3$ films. Figure 4.8a shows the IPCE spectra of freshly prepared PSC devices. All the freshly prepared devices exhibited similar quantum efficiency from the visible to the near-IR (300 nm - 800 nm) region. The toluene dripped PSC exhibited maximum IPCE of 90 % in the, 450 nm - 800 nm regions, whereas the chlorobenzene, *p*-xylene and ether treated cells showed IPCE of >80 % in the same region. The ether treated PSC showed a dip within 350 nm - 425 nm wavelengths.

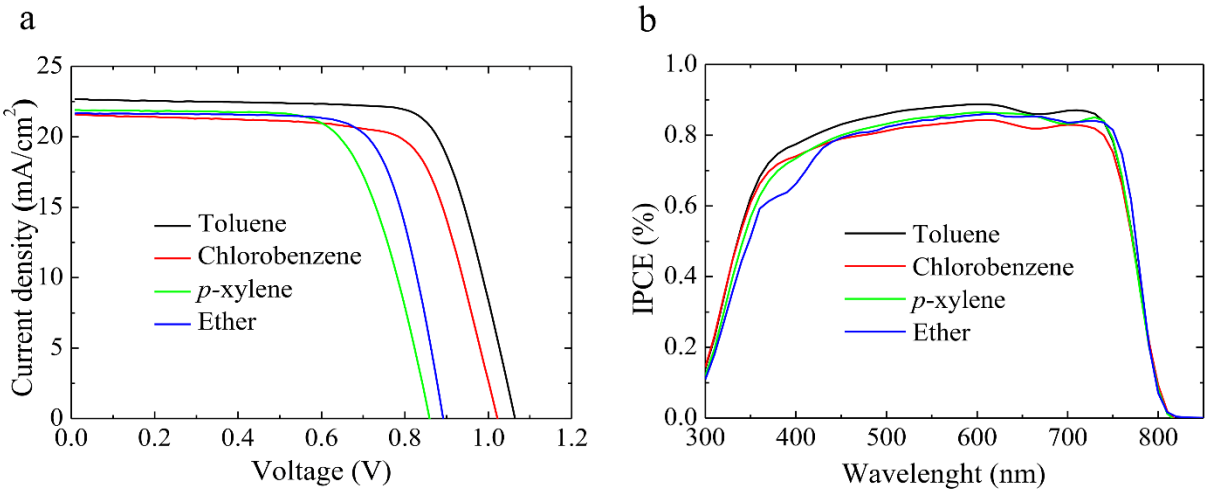

Figure 2.8. The performance of PSCs (freshly prepared) prepared by different anti-solvents; IPCE (a) and *J-V* (b).

Table 2.1. Summary of device performance parameters obtained from the *J-V* measurements of PSCs fabricated with different anti-solvents treatment.

Anti-solvent	Remarks of the PSCs	J_{SC} (mA/cm^2)	V_{OC} (V)	FF	PCE (%)[a)]
Toluene	average	21.378 ± 0.39	1.051 ± 0.02	0.730 ± 0.02	16.38 ± 0.45
	champion	22.68	1.064	0.743	17.93
Chlorobenzene	average	20.44 ± 1.08	0.990 ± 0.03	0.705 ± 0.04	14.30 ± 0.93
	champion	21.58	1.022	0.716	15.78
p-xylene	average	20.11 ± 1.2	0.803 ± 0.06	0.626 ± 0.04	10.12 ± 1.08
	champion	21.61	0.850	0.646	11.88
Ether	average	19.96 ± 0.32	1.001 ± 0.17	0.703 ± 0.06	14.01 ± 1.37
	champion	19.94	1.057	0.745	15.70

[a)] The PSCs parameters were measured using a metal mask of 1.02 cm^2 surface area and mean deviations are calculated from 10 devices for each anti-solvent treatment.

The photovolatic performances parameters of PSCs fabricated with perovskite films treated with toluene, chorobenzene, *p*-xylene and ether are summarized in Table 2.1. The champion PSC fabricated with toluene treated perovskite showed high PCE of 17.93 % (short circuit current (J_{SC}) = 22.68 mA/cm^2, open circuit voltage (V_{OC}) = 1.064 V, fill factor (FF) = 0.743). The best chlorobenzene treated perovskite film based PSC showed PCE of 15.78 % with photovoltaic parameters of J_{SC} = 21.58 mA/cm^2, V_{OC} = 1.022 V, and FF= 0.716. The *p*-xylene treated perovskite film yielded with PCE of 11.88 % in a PSC. In comparison to toluene and chlorobenzene tretated films, *p*-xylene treated PSC showed comparatively lower V_{OC} and FF which were 0.850 V and 0.646 respectively. The PCE of the ether treated champion PSC was 15.70 %. The FF of the PSC

fabricated by ether treated perovskite film was higher than that of cholorbenzene and *p*-xylene based PSCs fabricated with the same configuration.

2.3.3 Stability Under Dark Condition

The stability in dark condition for PSCs, fabricated with different anti-solvent treatment, has been observed by monitoring the variation of photovoltaic parameters as a function of time for 30 days (Figure 2.9). It has been observed that, the J_{SC} and FF for the

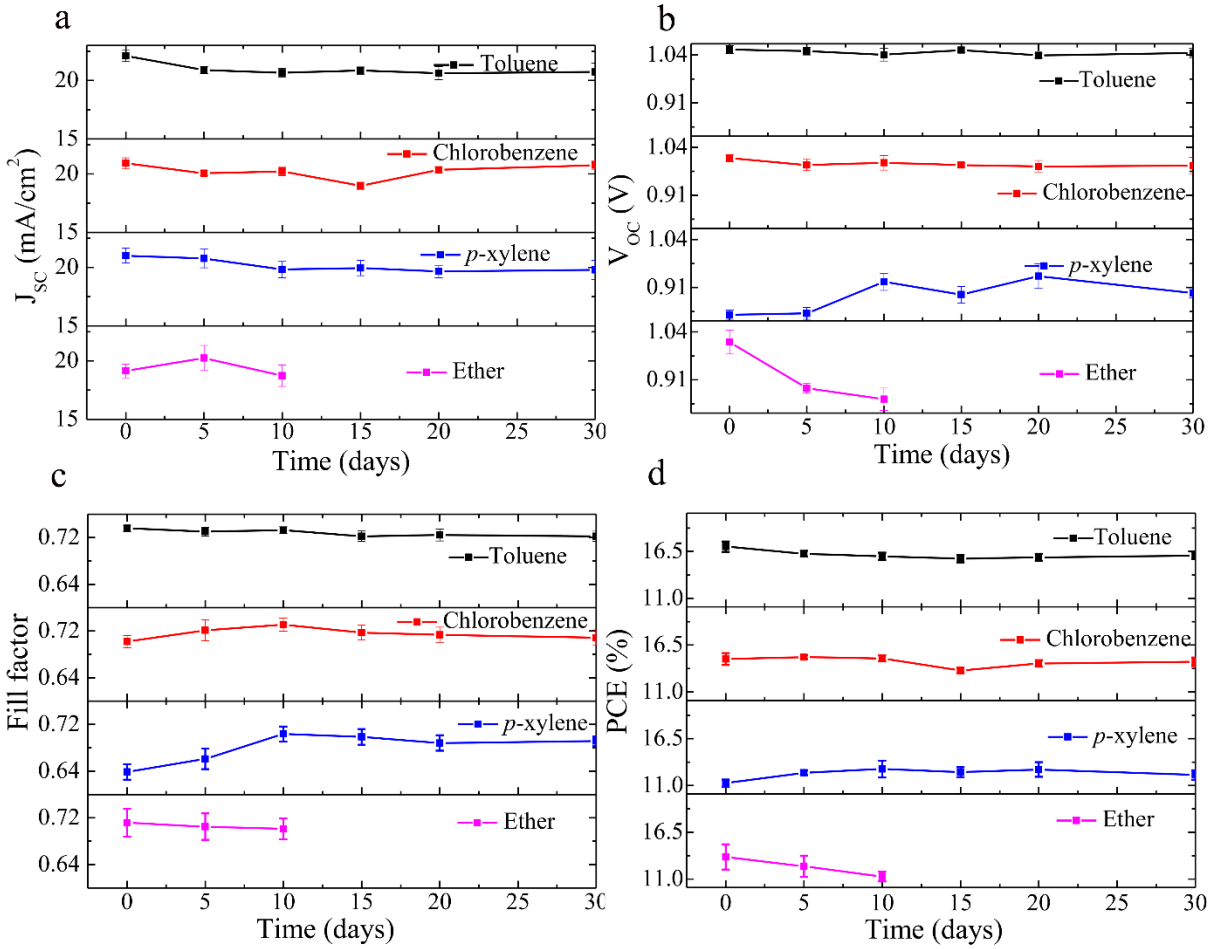

Figure 4.9. Time dependent performances of photovoltaic parameters (a) J_{SC}, (b)V_{OC}, (c) FF and (d) PCE of p-i-n PSCs fabricated by toluene, chlorobenzene, *p*-xylene and ether treatment in dark condition for 30 days.

toluene treated PSC decreased from 22.68 mA/cm^2 to 21.77 mA/cm^2 and 0.743 to 0.727 respectively after 30 days in dark condition which resulted in decreased PCE from 17.93% to 16.54%. The photovoltaic parameters for the chlorobenzene treated PSC remained constant throughout 30 days in dark condition. The most distinct change has been observed for the *p*-xylene and ether treated PSCs. For *p*-xylene treated PSC, the V_{OC} and FF incresed from 0.850 V to 0.912 V and 0.646 to 0.706 respectively which lifted the PCE from

11.88 % to 13.31 % . But for the ether treated PSC, the PCE decreased from 15.70 % to 12.08 % on the 10th day and no photovoltaic performance was observed afterwards. This detoriation in PCE was due to the decrease of FF and V_{OC} from 0.745 to 0.724 and 1.057 V to 0.833 V respectively. From these results, it has been observed that, with increased duration in dark condition the *p*-xylene treated PSC shows increased PCE. Whereas a decreased PCE has been recorded for toluene and ether treated PSCs. The PCE remained constant for the chlorobenzene treated cell during the test in dark condition.

2.3.4 Stability Under Light Soaking Condition

Figure 2.10 shows the effects of light soaking on the IPCE for PSCs fabricated by toluene,

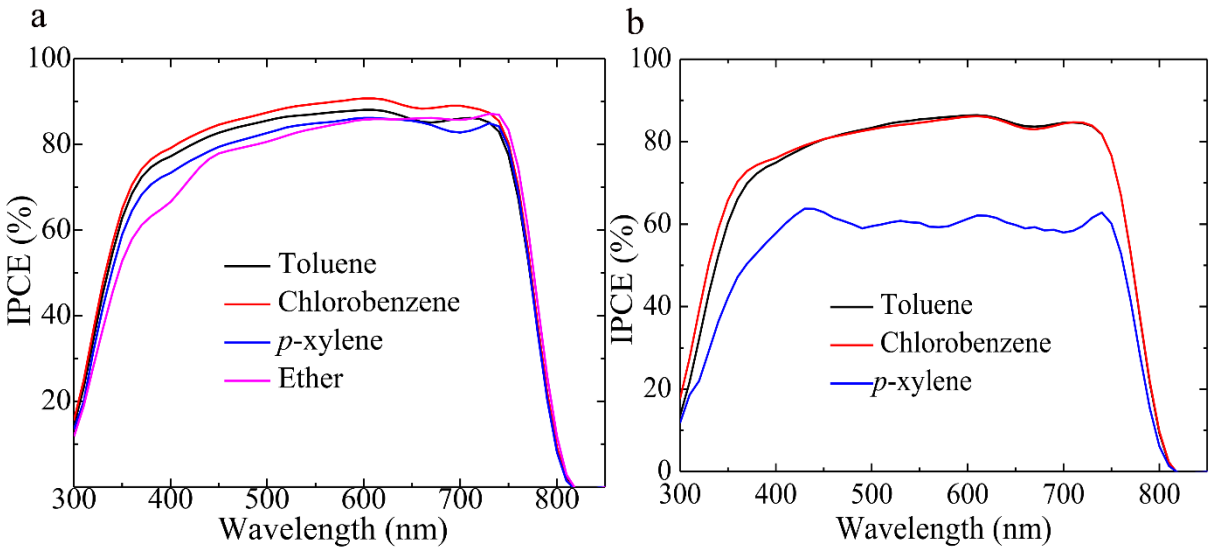

Figure 2.10. The variation of IPCE for PSCs fabricated by toluene, chorobenzene, *p*-xylene and ether anti-solvents treatment as a funtion of light soaking time (a) on after1st day and (b) 30th day of light soaking.

chlorobenzene, *p*-xylene and ether ASD treatment after 1st and 30th day. The IPCE for the Figure 2.10 shows the effects of light soaking on the IPCE for PSCs fabricated by toluene, chlorobenzene, *p*-xylene and ether ASD treatment after 1st and 30th day. The IPCE for the chlorobenzene treated PSC showed 92 % at 600 nm after 1st day and decreased to 84 % after 30 days of light soaking. Whereas for the toluene treated PSC, we observed constant 84 % IPCE at 600 nm through the 30 days light soaking. *p*-xylene treated PSC showed 82 % IPCE after 1st day which was decreased to 60 % after 30 days light soaking.

Figure 2.11a shows the time dependent performance of J_{SC} for toluene, chlorobenzene, *p*-xylene and ether treated PSCs. J_{SC} values for toluene and *p*-xylene remained constant during the entire light soaking period. The J_{SC} for the chlorobenzene treated PSC decreased from 21.56 mA/cm^2 to 18.45 mA/cm^2 after 30 days light soaking. The declining trend in J_{SC} value (from 20.38 mA/cm^2 to 13.75 mA/cm^2) is noticeable for the ether treated PSC with increasing time. Figure 2.11b presents the variation of V_{OC} with increasing time under light soaking. The V_{OC} for the PSCs fabricated by toluene and chlorobenzene were stable during this period, but the

p-xylene treated cell showed stable V_{OC} up to 17 days only and after that decreased with increasing time. The ether treated cell showed a rapid decrease of V_{OC} from the 1st day of light soaking test. The variation of FF with light soaking time followed the same trend as the V_{OC} (Figure 2.11c). The PCE for the toluene and chlorobenzene treated PSCs were stable performance throughout the entire light soaking period. They retained ~ 90 % of their respective initial PCE after 30 days. The *p*-xylene treated cell exhibited moderate stability in which the initial PCE was reduced by 5 % after 17 days and by 29 % within 30 days (Figure 2.11d). However, the ether treated PSC was most unstable and showed rapid degradation, which lost its initial PCE by 85 % on the 4th day and showed no photovoltaic performance on the 5th day. To further understand the underlying reasons for such variation in stability concerns, the hysteresis behavior of the corresponding PSCs has been studied both in dark and under continuous illumination which has been described in the following section.

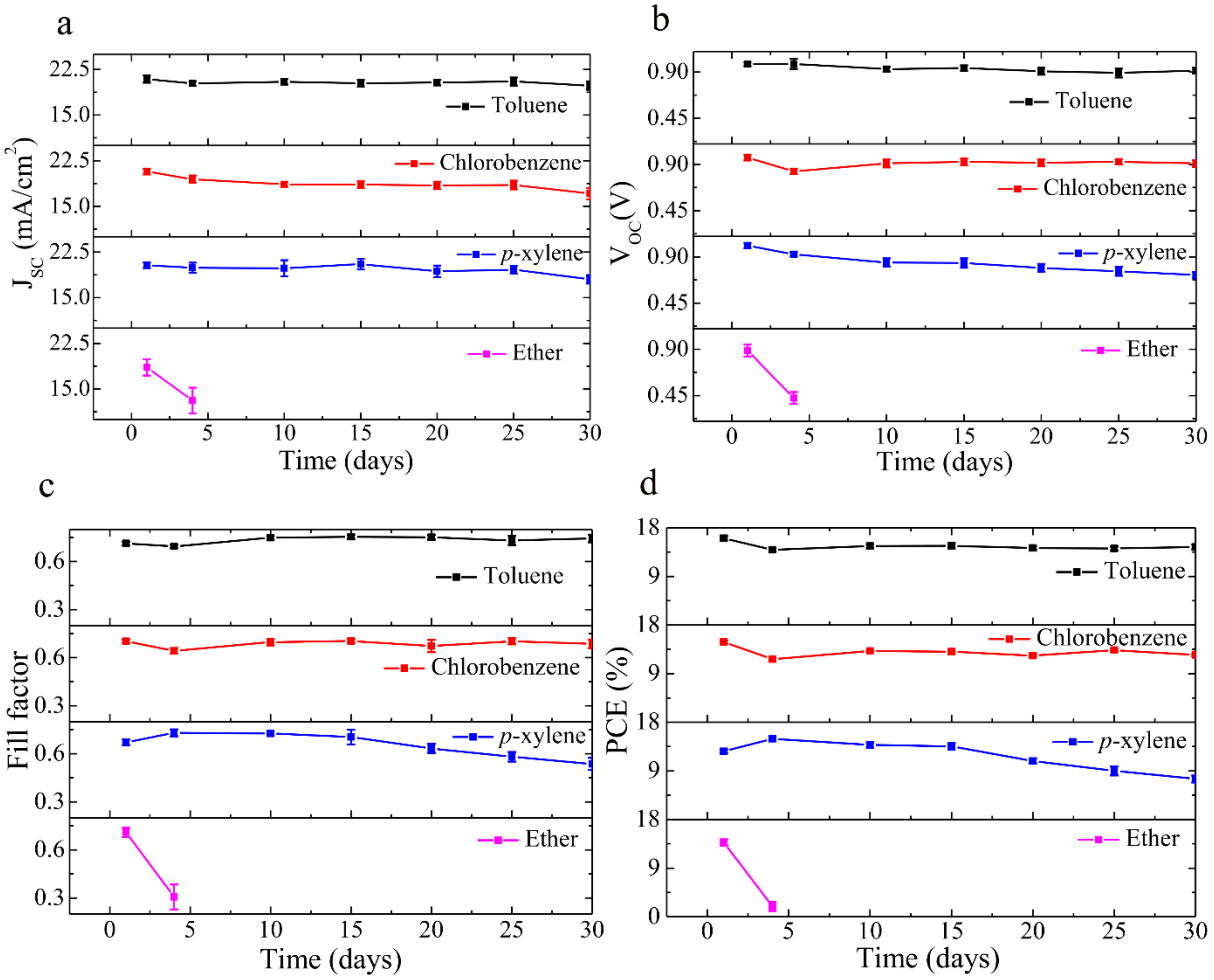

Figure 2.11. Time dependant variation of photovoltaic performance parameters (a) J_{SC}, (b) V_{OC} ,(c) FF and (d) PCE of PSCs fabricated by toluene, chlorobenzene, *p*-xylene and ether treatment (for 3 devices each) under contionious illumination for 30 days with standard AM 1.5 sunlight (100 mW cm^{-2}) and relative humidity of >70%.

2.3.5 Hysteresis Analysis

To observe the hysteretic behavior of PSCs fabricated by toluene, chlorobenzene, *p*-xylene and ether as a function of time, the *J-V* measurement has been performed in forward bias (F-B, -0.2 to 1.2 V) and reverse bias (R-B, 1.2 to -0.2 V) at the step width of 10 mV and delay time of 50 ms. Figure 2.12 shows the hysteretic behavior of toluene, chlorobenzene, *p*-xylene and ether treated PSCs on 1st and after 30th day measured in dark condition. The detailed photovoltaic parameters on 1st and after 30th day of *J-V* measurements are summarized in Table 2.2. The PSCs fabricated by toluene and chlorobenzene ASD treatment showed negligible hysteresis within 30 days (Figure 2.12a and 2.12b). Whereas the *p*-xylene treated PSC shows a higher hysteresis than the toluene and chlorobenzene treated PSCs (Figure 2.12c). On the 1st day, the J_{SC} showed 1.87 mA/cm^2 decrease value but the V_{OC} and FF increased from 0.850 V to 0.959 V and 0.646 to 0.687, respectively, in the R-B compared to F-B measurement. This increment in V_{OC} and FF lifted the PCE from 11.88 % to 13.00 % in R-B measurement. After 30 days in dark condition, from the *J-V* measurement with F-B and R-B scan, the main difference has been observed on the V_{OC} parameter rather than the J_{SC} or FF (Table 2.2). The ether treated PSC showed negligible hysteresis on the 1st day but after the 10th day a large hysteresis was observed (Figure 2.12d). After the 10th day, the hysteresis was due to the change in V_{OC} from 0.833 V to 1.064 V during F-B and R-B measurement respectively.

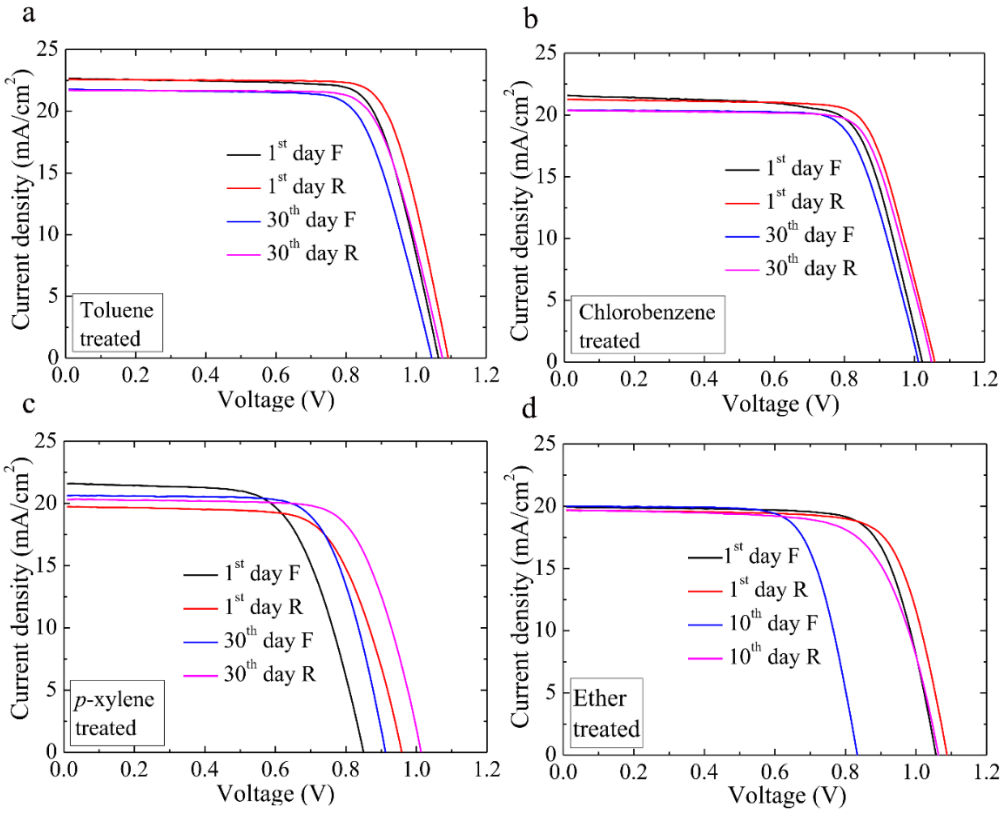

Figure 2.12. Forward and reverse scan of *J-V* curves of PSCs, treated with different anti-solvents, at different period of time under dark condition.

Table 2.2. Photovoltaic parameters of PSCs devices with toluene, chlorobenzene, *p*-xylene and ether treated perovskite films studied under dark condition.

Anti-solvent	Time (day)	Scan direction	J_{SC} (mA/cm^2)	V_{OC} (V)	FF	PCE (%)
Toluene	1	Forward	22.68	1.064	0.743	17.93
		Reverse	22.58	1.092	0.763	18.81
	30	Forward	21.77	1.045	0.727	16.54
		Reverse	21.07	1.091	0.754	17.34
Chlorobenzene	1	Forward	21.58	1.022	0.716	15.78
		Reverse	21.26	1.058	0.742	16.68
	30	Forward	20.41	1.011	0.734	15.15
		Reverse	20.36	1.049	0.748	15.96
p-xylene	1	Forward	21.61	0.850	0.646	11.88
		Reverse	19.74	0.959	0.687	13.00
	30	Forward	20.66	0.912	0.706	13.31
		Reverse	20.35	1.013	0.714	14.71
Ether	1	Forward	19.94	1.057	0.745	15.70
		Reverse	19.68	1.088	0.749	16.03
	10	Forward	20.41	0.833	0.724	12.08
		Reverse	19.68	1.064	0.697	14.59

The Hysteresis behaviour under light soaking condition has also been observed under light soaking condition for differente anti-solvent treated PSCs (Figure 2.13). Figure 2.13a presents the *J-V* hysteresis curves for toluene treated cell after the 1st and 30th day of light soaking. Here the PSC experienced negligible hysteresis during the light soaking period. The J_{SC} and FF vales for the forward and reverse bias were almost same and only showed little increase in V_{OC} for the R-B than F-B. The chlorobenzene treated PSC showed similar hysteresis behavior as for toluene treated cell after the 1st day of light soaking (Figure 2.13b). After 30th day of light soaking, the hysteresis increased a little compared to the 1st day of light soaking as observed in Figure 2.13b. For the *p*-xylene treated PSC (Figure 2.13c), low hysteresis up to 17th day was observed and immediate gradual hysteresis increament with increased light soaking time has been recorded. The increase in hysteresis was due to the variation in J_{SC} and V_{OC} parameters, whereas the FF remained unaffected. The F-B resulted in a higher J_{SC} and lower V_{OC} compared to R-B. The difference in J_{SC} and V_{OC} between F-B and R-B scans increased from 0.33 mA/cm^2 to 5.83 mA/cm^2 and 0.1 V to 0.14 V respectively, during light soaking period (Table 2.3). The PSC fabricated by using ether ASD treated perovskite film showed very high hysteresis even after the 1st day of light soaking (Figure 2.13d) and no photovoltaic response was observed from the 5th day onwards. In this device, after the 1st day of light soaking, the hysteresis was mainly due to the V_{OC} difference, whereas a reduced value of 0.138 V in the F-B compared to R-B has been observed. But after the 4th day, the hysteresis behaviour was reflected by the difference in all photovoltaic performance parameters during F-B and R-B measurement. From the hysteretic behavior of the fabricated PSCs, it is eminent that, PSCs with perovskite layers fabricated by toluene and chlorobenzene ASD treatment were most stable and showed negligible hysteresis. The *p*-xylene treated PSC showed stable performance upto 17 days

under continuous light soaking and also showed minor hysteresis but after 17 days light soaking, the stability deteriorated and hysteresis eventually increased. Lastly, the ether treated PSC showed unstable performance as it was also reflected from its hysteresis behavior from the 1st day of light soaking.

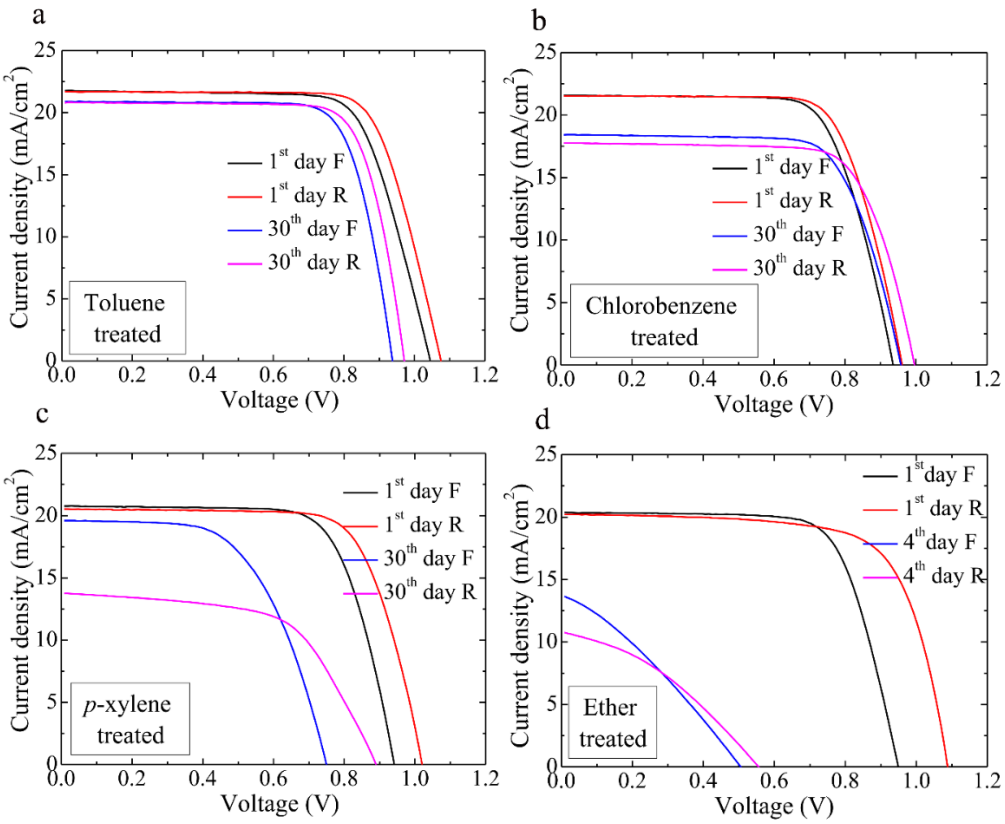

Figure 2.13. Forward and reverse scan of *J-V* curves of PSCs, treated with different anti-solvents, after 1 day and 30 days of light soaking under air mass 1.5 sunlight (100 mW cm^{-2}) and relative humidity of >70 %.

Table 2.3. Photovoltaic parameters of PSCs with different anti-sovents treatment after the 1st and 30th day for toluene, chlorobenzene and *p*-xylene and after the 1st and 4th day for ether under light soaking.

Anti-solvent	Time (day)	Scan direction	J_{SC} (mA/cm^2)	V_{OC} (V)	FF	PCE (%)
Toluene	1	Forward	21.77	1.045	0.727	16.54
		Reverse	21.69	1.075	0.746	17.39
	30	Forward	20.90	0.938	0.763	14.96
		Reverse	20.79	0.972	0.770	15.56
Chlorobenzene	1	Forward	21.56	0.936	0.717	14.47
		Reverse	21.52	0.961	0.727	15.04
	30	Forward	18.45	0.958	0.717	12.66

		Reverse	17.76	0.996	0.728	12.88
p-xylene	1	Forward	20.77	0.941	0.716	14.01
		Reverse	20.44	1.038	0.699	14.83
	30	Forward	19.61	0.750	0.583	8.57
		Reverse	13.78	0.890	0.591	7.25
Ether	1	Forward	20.38	0.950	0.718	13.88
		Reverse	20.24	1.088	0.704	15.51
	4	Forward	13.75	0.505	0.307	2.14
		Reverse	10.80	0.556	0.360	2.16

From the stability and *J-V* hysteresis observations during light soaking period, it is eminent that, the PSCs with low *J-V* hysteresis during F-B and R-B measurement were more stable. To find out the origin of *J-V* hysteresis, Reenen et al. performed a numerical work on PSCs and demonstrated that both ions migration and interfacial trap states are combinedly responsible for hysteresis.[36] In this study, the similar compostion has been used for for all layers during PSCs fabrication. So the ions migration in all PSCs should be same but the interfacial trap state may be varied due to different anti-solvent treatment. In this situation, it is suspected that the interfacial trap states are the only responsible candidate for different hysteresis behavior. It is well known that PCBM deposition on top of perovsktie film penetrates into the perovskite absorber film via grain boundaries and sufficiently passivates the trap states located at the grain boundaries resulting reduced hysteresis of the overall PSC.[37] From the SEM cross-sectional characterization, it has been observed that toluene, chlorobenzene and *p*-xylene dripping formed single grains exceeding the perovskite films thickness. So, the PCBM deposited on the top of these perovskite films, easily penetrated into the corresponding films and effectively passivateed the trap. This process is schematrically illustrated in figure 2.14a. Hence, these PSCs showed negligible hysteresis and stable performance in dark condition. The ether treated perovskite film contained small aggregated grains with cracks and numerous pinholes providing limited penetration opportunities for PCBM to passivate the trap state (Figure 2.14b). Hence, the PSC formed via ether ASD treatment showed poor stability in the dark condition.

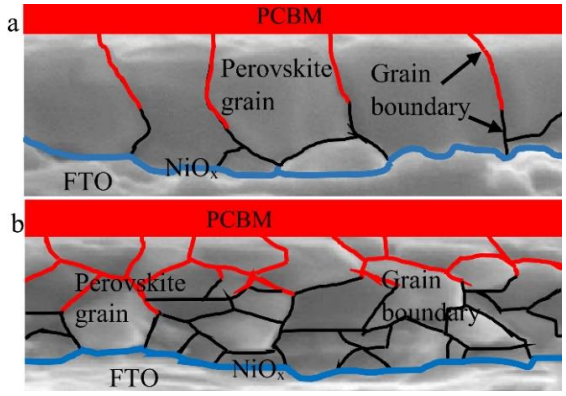

Figure 2.14. Diagrams show the path for the PCBM penetration for (a) single grain structure and (b) multi-grain structure.

After 30 days light soaking, the toluene and chlorobenzene treated perovsktie films remained same as initial films (Figure 2.7a and 2.7b). Hence these PSCs showed stable performance throughout the entire period of light soaking test. But for the *p*-xylene treated perovskite films after 30 days light soaking, some white particles aroung the grian boundaries were observed, may be decomposition product of $CH_3NH_3PbI_3$ after light soaking, the PSC experienced a large hysteresis. These newly formed white particles during light soaking may be act as interfacial trap state and hinder the overall charge transpotation process resulted in a large hysteresis with very low Jsc in the reverse scan (Figure 2.13c). Thus the *p*-xylene treated PSC intially showed stable performance but detoriated with increased time of light soaking. For ether treated perovskite film, the light soaking increases the pore size and number of pinholes. Hence, the PSC formed via ether ASD treatment showed worst performance and poor stability from the beginning of light soaking.

2.4 Summary

In this work, the effects of toluene, chlorobenzene, *p*-xylene and ether anti-solvents treatment on the perovskite film formation and corresponding device peroformance in terms of perovskite film morphology and corresponding device performancce and stability have been observed. From detail characterization, it has been revealed that the opetical and structural propeties of perovskite films were independent of anti-solvent treatment but the morphology varied which affects the device performance. Due to the formation of single grain structure across the cross-section and robust nature, the toluene and chlorobenzene treated PSCs showed stable performance both under dark and light soaking conditions. On the other hand, the unstable performance of *p*-xylene treated PSCs were due to the deterioration of perovskite films under light soaking condition. For the ether treated PSCs, the poor film morphology caused worest device performanc. Throug this study, a correlation between the morphology of perovskite film formed by different ASD treatment and stability in the respective fabricated PSCs has been successfully highlighted. This study will be help to choose the appropriate anti-solvent for the fabrication of stable and high efficient PSC.

References

(1) J.H. Noh, S.H. Im, J.H. Heo, T.N. Mandal, S.I. Seok, Chemical Management for Colorful, Efficient, and Stable Inorganic–Organic Hybrid Nanostructured Solar Cells, *Nano Lett.* **2013**, 13, 1764-1769.

(2) N. Pellet, P. Gao, G. Gregori, T.Y. Yang, M.K. Nazeeruddin, J. Maier, M. Grätzel, Mixed‐Organic‐Cation Perovskite Photovoltaics for Enhanced Solar‐Light Harvesting, *Angew. Chem. Int. Ed*., **2014**, 53, 3151-3157.

(3) T.C. Sum, N. Mathews, Advancements in Perovskite Solar Cells: Photophysics Behind the Photovoltaics, *Energy Environ. Sci.*, **2014**, 7, 2518-2534.

(4) Y. Ogomi, A. Morita, S. Tsukamoto, T. Saitho, N. Fujikawa, Q. Shen, T. Toyoda, K. Yoshino, S.S. Pandey, T. Ma, $CH_3NH_3Sn_xPb_{(1-x)}I_3$ Perovskite Solar Cells Covering up to 1060 nm, *J. Phys. Chem. Lett*., **2014**, 5, 1004-1011.

(5) G. Xing, N. Mathews, S. Sun, S.S. Lim, Y.M. Lam, M. Grätzel, S. Mhaisalkar, T.C. Sum, Long-range balanced electron-and hole-transport lengths in organic-inorganic $CH_3NH_3PbI_3$, *Science*, **2013**, 342, 344-347.

(6) S.D. Stranks, G.E. Eperon, G. Grancini, C. Menelaou, M.J. Alcocer, T. Leijtens, L.M. Herz, A. Petrozza, H.J. Snaith, Electron-Hole Diffusion Lengths Exceeding 1 Micrometer in an Organometal Trihalide Perovskite Absorber, *Science*, **2013**, 342, 341-344.

(7) J.H. Heo, S.H. Im, J.H. Noh, T.N. Mandal, C.-S. Lim, J.A. Chang, Y.H. Lee, H.-j. Kim, A. Sarkar, M.K. Nazeeruddin, Efficient Inorganic-Organic Hybrid Heterojunction Solar Cells Containing Perovskite Compound and Polymeric Hole Conductors, *Nat. Photonics*, **2013**, 7, 486-491.

(8) M. Saliba, T. Matsui, K. Domanski, J.-Y. Seo, A. Ummadisingu, S.M. Zakeeruddin, J.-P. Correa-Baena, W.R. Tress, A. Abate, A. Hagfeldt, Incorporation of Rubidium Cations into Perovskite Solar Cells Improves Photovoltaic Performance, *Scienc*e, **2016**, 354, 206-209.

(9) A. Kojima, K. Teshima, Y. Shirai, T. Miyasaka, Organometal Halide Perovskites as Visible-Light Sensitizers for Photovoltaic Cells, *J. Am. Chem. Soc*., **2009**, 131,6050-6051.

(10) M. Saliba, T. Matsui, J.-Y. Seo, K. Domanski, J.-P. Correa-Baena, M.K. Nazeeruddin, S.M. Zakeeruddin, W. Tress, A. Abate, A. Hagfeldt, Cesium-Containing Triple Cation Perovskite Solar Cells: Improved Stability, Reproducibility and High Efficiency, *Energy Environ. Sci*., **2016**, 9, 1989-1997.

(11) D. Bi, C. Yi, J. Luo, J.-D. Décoppet, F. Zhang, S.M. Zakeeruddin, X. Li, A. Hagfeldt, M. Grätzel, Polymer-Templated Nucleation and Crystal Growth of Perovskite Films for Solar Cells with Efficiency Greater Than 21%, *Nat. Energy*, **2016**, 1, 16142.

(12) Y. Cheng, X. Xu, Y. Xie, H.W. Li, J. Qing, C. Ma, C.S. Lee, F. So, S.W. Tsang, 18% High‐Efficiency Air‐Processed Perovskite Solar Cells Made in a Humid Atmosphere of 70% Rh, Solar RRL, **2017**, 1, 1700097.

(13) B. Ding, Y. Li, S.-Y. Huang, Q.-Q. Chu, C.-X. Li, C.-J. Li, G.-J. Yang, Material Nucleation/Growth Competition Tuning Towards Highly Reproducible Planar Perovskite Solar Cells with Efficiency Exceeding 20%, *J. Mater. Chem. A*, **2017**, 5, 6840-6848.

(14) W. Chen, Y. Wu, Y. Yue, J. Liu, W. Zhang, X. Yang, H. Chen, E. Bi, I. Ashraful, M. Grätzel, Efficient and Stable Large-Area Perovskite Solar Cells with Inorganic Charge Extraction Layers, *Science*, **2015**, 350, 944-948.

(15) Y. Wu, F. Xie, H. Chen, X. Yang, H. Su, M. Cai, Z. Zhou, T. Noda, L. Han, Thermally Stable $MAPbI_3$ Perovskite Solar Cells with Efficiency of 19.19% and Area over 1 cm^2 achieved by Additive Engineering, *Adv. Mater.,* **2017**, 29, 1701073.

(16) J.W. Lee, D.J. Seol, A.N. Cho, N.G. Park, High-Efficiency Perovskite Solar Cells Based on the Black Polymorph of $HC(NH_2)_2PbI_3$, *Adv. Mater.,***2014**, 26, 4991-4998.

(17) C. Momblona, O. Malinkiewicz, C. Roldán-Carmona, A. Soriano, L. Gil-Escrig, E. Bandiello, M. Scheepers, E. Edri, H. Bolink, Efficient Methylammonium Lead Iodide Perovskite Solar Cells with Active Layers from 300 to 900 nm, *APL Mater.,***2014**, 2, 081504.

(18) M. Liu, M.B. Johnston, H.J. Snaith, Efficient Planar Heterojunction Perovskite Solar Cells by Vapour Deposition, *Nature,* **2013**, 501, 395.

(19) N.J. Jeon, J.H. Noh, Y.C. Kim, W.S. Yang, S. Ryu, S.I. Seok, Solvent Engineering for High-Performance Inorganic–Organic Hybrid Perovskite Solar Cells, *Nat. Mater.*, **2014**, 13, 897-903.

(20) N. Ahn, D.-Y. Son, I.-H. Jang, S.M. Kang, M. Choi, N.-G. Park, Highly Reproducible Perovskite Solar Cells with Average Efficiency of 18.3% and Best Efficiency of 19.7% Fabricated Via Lewis Base Adduct of Lead (Ii) Iodide*, J. Am. Chem*. Soc.*,***2015**, 137, 8696-8699.

(21) J.P.C. Baena, L. Steier, W. Tress, M. Saliba, S. Neutzner, T. Matsui, F. Giordano, T.J. Jacobsson, A.R.S. Kandada, S.M. Zakeeruddin, Highly Efficient Planar Perovskite Solar Cells Through Band Alignment Engineering, *Energy Environ. Sci*., **2015**, 8, 2928-2934.

(22) Y. Wu, A. Islam, X. Yang, C. Qin, J. Liu, K. Zhang, W. Peng, L. Han, Retarding the Crystallization of PbI_2 for Highly Reproducible Planar-Structured Perovskite Solar Cells Via Sequential Deposition, *Energy Environ. Sci.,* **2014**, 7, 2934-2938.

(23) P.-H. Huang, Y.-H. Wang, J.-C. Ke, C.-J. Huang, The Effect of Solvents on the Performance of $CH_3NH_3PbI_3$ Perovskite Solar Cells, *Energies*, **2017**, 10, 599.

(24) G.E. Eperon, V.M. Burlakov, P. Docampo, A. Goriely, H.J. Snaith, Morphological Control for High Performance, Solution‐Processed Planar Heterojunction Perovskite Solar Cells, *Adv. Funct. Mater*.,**2014**, 24, 151-157.

(25) W.S. Yang, B.-W. Park, E.H. Jung, N.J. Jeon, Y.C. Kim, D.U. Lee, S.S. Shin, J. Seo, E.K. Kim, J.H. Noh, Iodide Management in Formamidinium-Lead-Halide–Based Perovskite Layers for Efficient Solar Cells, *Science*, **2017**, 356, 1376-1379.

(26) D.-Y. Son, J.-W. Lee, Y.J. Choi, I.-H. Jang, S. Lee, P.J. Yoo, H. Shin, N. Ahn, M. Choi, D. Kim, Self-Formed Grain Boundary Healing Layer for Highly Efficient $CH_3NH_3PbI_3$ Perovskite Solar Cells, *Nat. Energy*, **2016**, 1, 16081.

(27) Y. Wu, X. Yang, W. Chen, Y. Yue, M. Cai, F. Xie, E. Bi, A. Islam, L. Han, Perovskite Solar Cells with 18.21% Efficiency and Area Over 1 cm^2 Fabricated by Heterojunction Engineering, *Nat. Energy*, **2016**, 1,16148.

(28) M. Xiao, F. Huang, W. Huang, Y. Dkhissi, Y. Zhu, J. Etheridge, A. Gray-Weale, U. Bach, Y.B. Cheng, L. Spiccia, A Fast Deposition‐Crystallization Procedure for Highly Efficient Lead Iodide Perovskite Thin‐Film Solar Cells, *Angew. Chem.*, **2014**, 126, 10056-10061.
(29) S. Paek, P. Schouwink, E.N. Athanasopoulou, K. Cho, G. Grancini, Y. Lee, Y. Zhang, F. Stellacci, M.K. Nazeeruddin, P. Gao, From Nano-to Micrometer Scale: The Role of Antisolvent Treatment on High Performance Perovskite Solar Cells, *Chem. Mater.*, **2017**, 29, 3490-3498.
(30) L. Gate, Comparison of The Photon Diffusion Model and Kubelka-Munk Equation with the Exact Solution of the Radiative Transport Equation, *Applied optics*, **1947**, 13, 236-238.
(31) T. Baikie, Y. Fang, J.M. Kadro, M. Schreyer, F. Wei, S.G. Mhaisalkar, M. Graetzel, T.J. White, Synthesis and Crystal Chemistry of The Hybrid Perovskite $(CH_3NH_3)PbI_3$ for Solid-State Sensitised Solar Cell Applications, *J. Mater. Chem. A*, **2013**, 1, 5628-5641.
(32) S. Dharani, H.K. Mulmudi, N. Yantara, P.T.T. Trang, N.G. Park, M. Graetzel, S. Mhaisalkar, N. Mathews, P.P. Boix, High Efficiency Electrospun TiO_2 Nanofiber Based Hybrid Organic–Inorganic Perovskite Solar Cell, *Nanoscale*, **2014**, 6, 1675-1679.
(33) S. Gharibzadeh, B.A. Nejand, A. Moshaii, N. Mohammadian, A.H. Alizadeh, R. Mohammadpour, V. Ahmadi, A. Alizadeh, Two‐Step Physical Deposition of a Compact CuI Hole‐Transport Layer and The Formation of an Interfacial Species in Perovskite Solar Cells, *ChemSusChem*, **2016**, 9, 1929-1937.
(34) N. Rajamanickam, S. Kumari, V.K. Vendra, B.W. Lavery, J. Spurgeon, T. Druffel, M.K. Sunkara, Stable and Durable $CH_3NH_3PbI_3$ Perovskite Solar Cells at Ambient Conditions, *Nanotechnology*, **2017**, 27, 235404.
(35) T. Zhang, N. Guo, G. Li, X. Qian, Y. Zhao, A Controllable Fabrication of Grain Boundary PbI_2 Nanoplates Passivated Lead Halide Perovskites for High Performance Solar Cells, *Nano Energy*, **2016**, 26, 50-56.
(36) S. van Reenen, M. Kemerink, H.J. Snaith, Modeling Anomalous Hysteresis in Perovskite Solar Cells, J. *Phys. Chem. Lett.,* **2015**, 6, 3808-3814.
(37) Y. Shao, Z. Xiao, C. Bi, Y. Yuan, J. Huang, Origin and Elimination of Photocurrent Hysteresis by Fullerene Passivation in $CH_3NH_3PbI_3$ Planar Heterojunction Solar Cells, *Nat. Commun.*, **2014**, 5, 5784.

Supporting Information

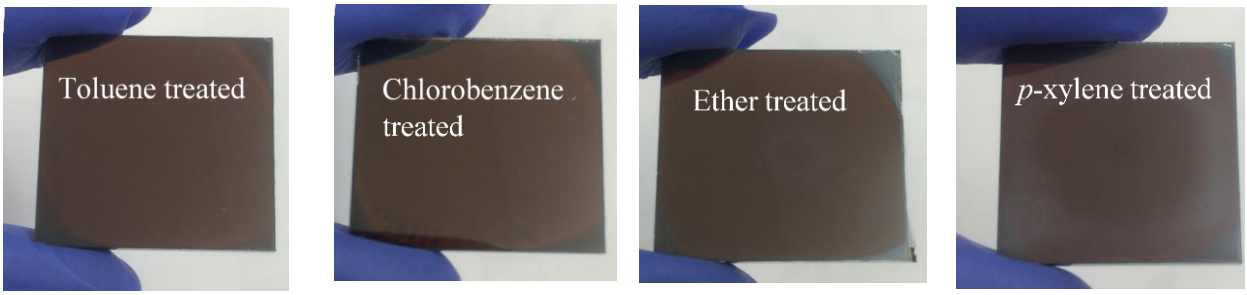

Figure S2.1. Photograph of toluene, chlorobenzene, *p*-xylene and ether treated perovskite films after annealing at 100 ^{0}C for 15 min.

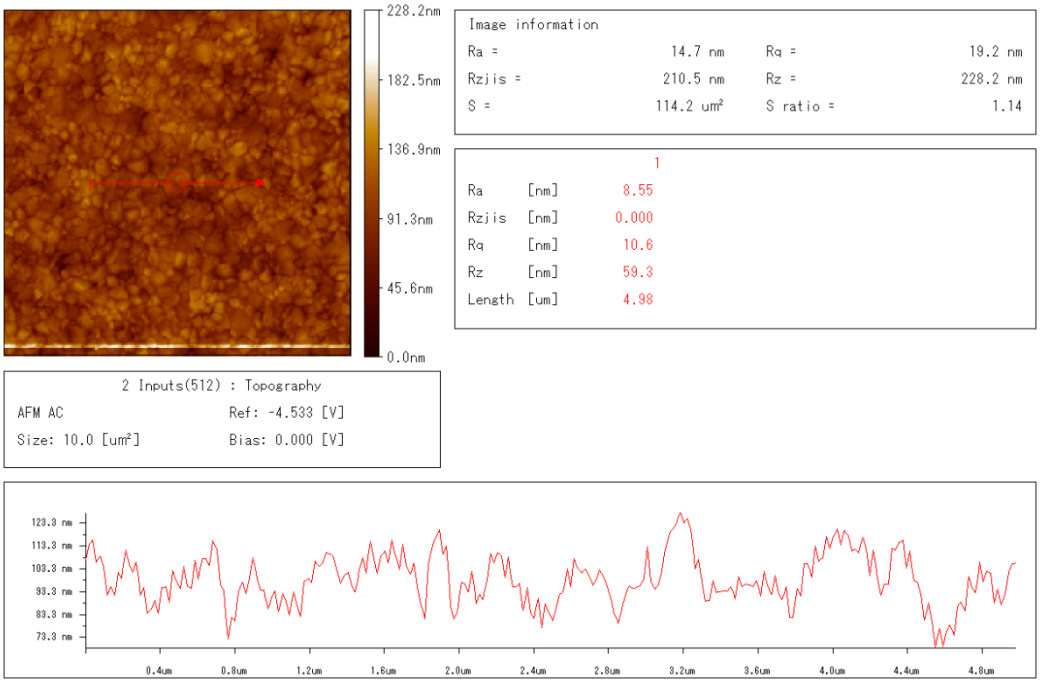

Figure S2.2. AFM image of toluene treated perovskite film with line profile.

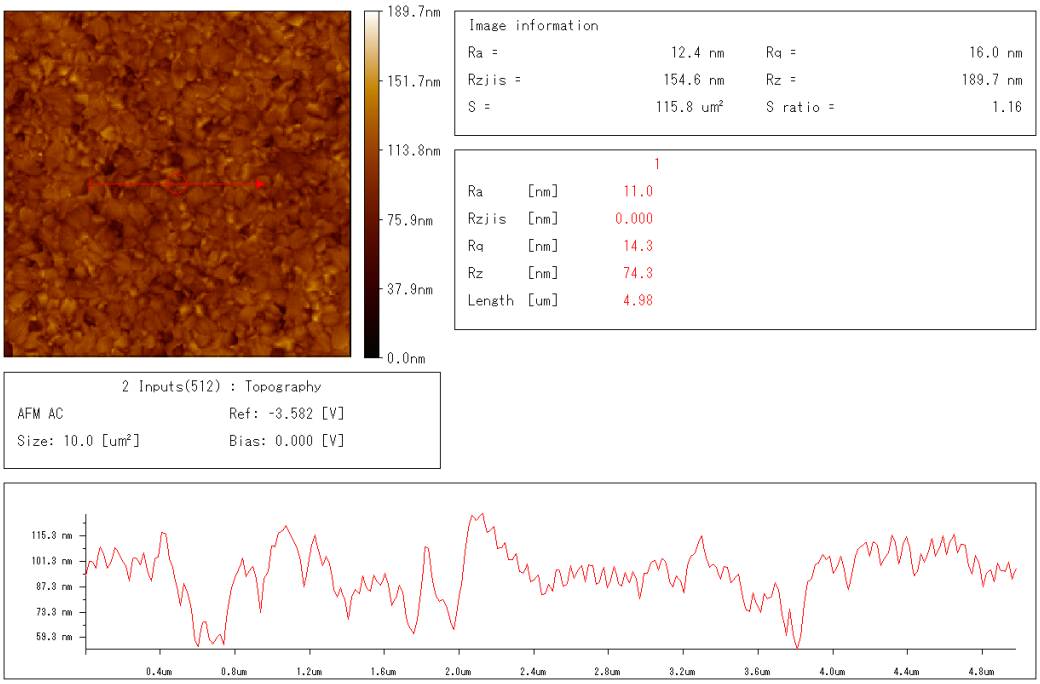

Figure S2.3. AFM image of chlorobenzene treated perovskite film with line profile.

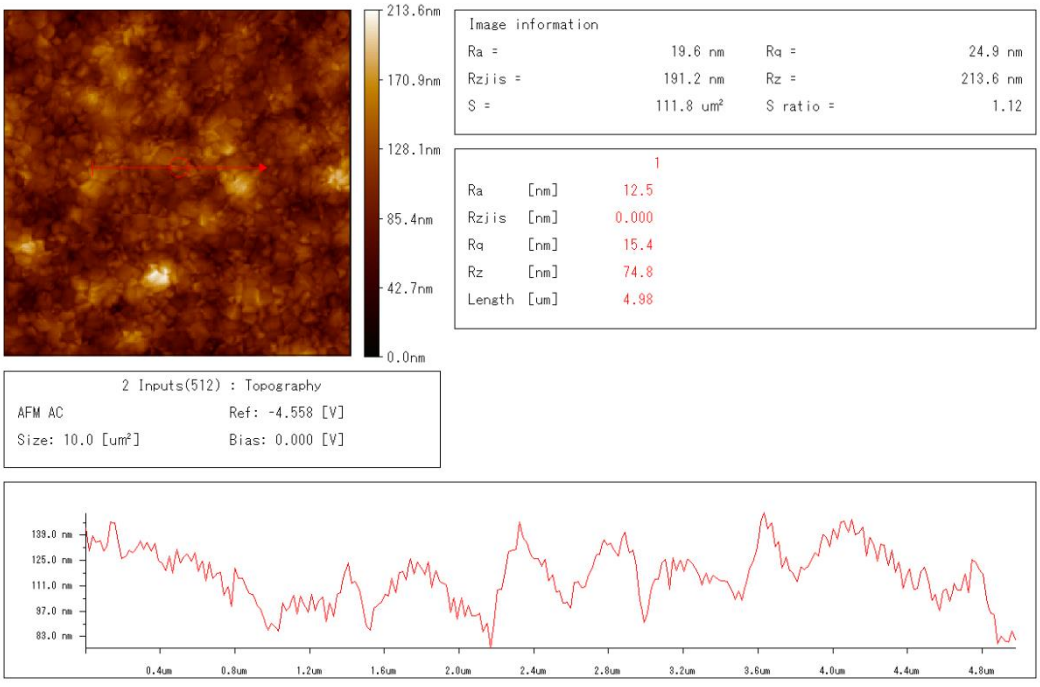

Figure S2.4. AFM image of *p*-xylene treated perovskite film with line profile.

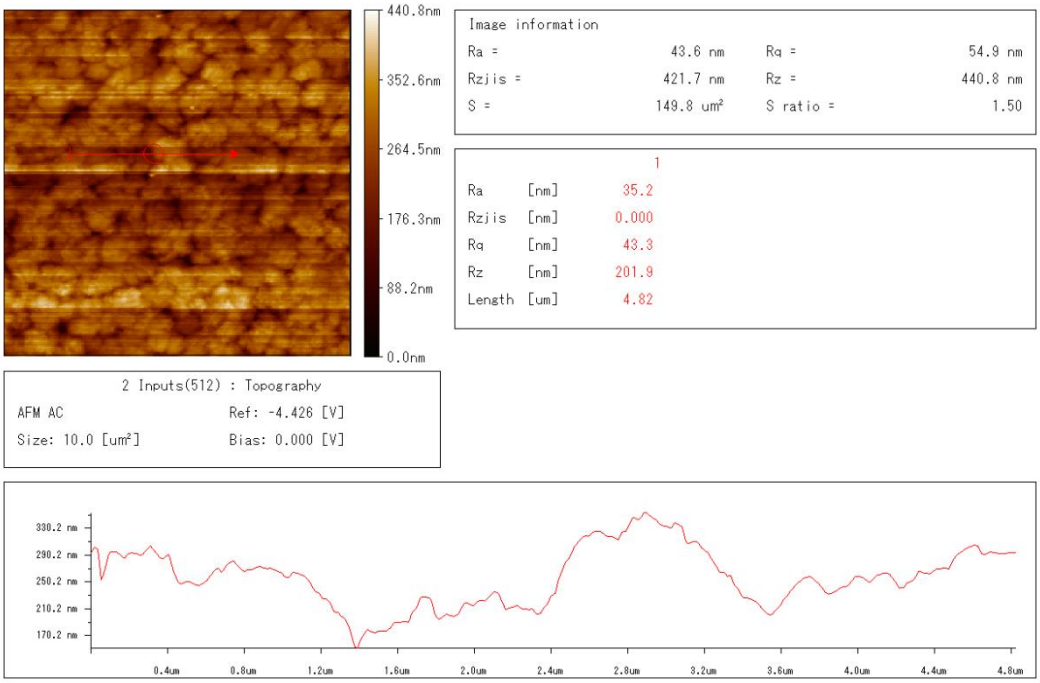

Figure S2.5. AFM image of ether treated perovskite film with line profile.

Chapter 3

Enhanced Photovoltaic Performance of Perovskite Solar Cells by Copper Chloride ($CuCl_2$) as an Additive in Single Solvent Perovskite Precursor

3.1 Introduction

For highly efficient perovskite solar cells (PSCs), the fabrication of uniform and crystalline perovskite film is the most crucial part. In this regard, the one-step anti-solvent method is well known for the fabrication of perovskite with optimum properties. In one step anti-solvent method, usually two solvents such as N, N-dimethylfomamide (DMF) and dimethyl sulfoxide (DMSO) or DMF and γ-Butyrolactone (GBL) are used as solvent for precursor solution to fabricate high quality of perovskite films.[1] Here DMSO or GBL form intermediate phase with BX_2 and slow down the crystallization of perovskite formation and lead to the formation uniform and homogeneous film.[2] For large scale fabrication in commercial aspects a single solvent perovskite precursor is more beneficial. But, the single solvent precursor solution leads to poor film morphology due to the uncontrol crystallization rate.[3] However, in one-step annealing method, additive engineering is well known for fabrication of perovskite film with enhanced optoelectronic properties and so the performance of corresponding PSCs. For example, a various type of additives such as metallic chlorides, organic molecules, inorganic or ammonium salts, polymers, ionic liquids etc. have been successfully used to form uniform and full covered perovskite films.[4-8] Here, the additive coordinate with BX_2 to form complex compound and control the perovskite growth rate.[9] This leads to the formation of uniform and homogeneous perovskite films with high crystallinity. The additive engineering has also been successfully used for other fabrication method to enhance the performance of PSCs. For example, Heben et al. used cadmium chloride ($CdCl_2$) as an additive in two-step method and observed enhanced grain size with improved crystallinity of perovskite films. As a result, the PCE of corresponding boosted to 2 orders of magnitude as compare with pristine one.[10] To simplify the one-step anti-solvent method, additive engineering has also been performed in this method for single solvent precursor system. For example, Troshin et al. have used HgI_2 in a single solvent (DMF) $CH_3NH_3PbI_3$ precursor solution to form uniform perovskite film and observed an enhancement of PCE from 9.4% (without HgI_2) to 13% (with HgI_2).[3] So, the combination of additive engineering and anti-solvent method together might be beneficial to produce high quality perovskite films for efficient PSCs.

In this work, the $CuCl_2$ has been introduced as an additive in the $CH_3NH_3PbI_3$ precursor solution with DMF as the solvent to obtain high quality perovskite films prepared by anti-solvent method. The effects of $CuCl_2$ addition on the final perovskite films was investigated through structural and optoelectronic characterization.

From the detail characterization, it has been observed that the addition of CuCl2, dramatically improved the morphology and optoelectronic properties. As a result, the optimized PSCs with 2.5 mol % $CuCl_2$, showed the best PCE of 15.22% with short circuit current (J_{SC}) of 17.99 mA/cm^2, open circuit voltage (V_{OC}) of 1.022 V and fill factor (FF) of 0.828.

3.2 Experimental Procedure

3.2.1 Materials

In this work, all the chemicals were used as received without any further purification including- PbI_2 (99%, Sigma–Aldrich), MAI (CH_3NH_3I) (> 98%, Tokyo Chemical Industry Co., Japan), $CuCl_2$ (97%, Sigma–Aldrich), nickel acetylacetonate (95%, Sigma–Aldrich), $PC_{61}BM$ (phenyl-C61-butyric acid methyl ester) (99.5%, Lumtec Co., Taiwan). Magnesium acetatetetrahydrate (99%), bathocuproine (BCP) and solvents of N,N-dimethylfomamide, toluene, chlorobenzene, acetonitrile, methanol and ethanol, were purchased from Wako Co. Japan.

3.2.2 Device Fabrication

The patterned fluorine doped tin oxide (FTO) coated glass substrates were ultrasonically cleaned with detergent, de-ionized water and ethanol sequentially for 15 minutes each and ultraviolet (UV)/ozone treated for 30 min . The NiO_x layer was sprayed on to the cleaned FTO substrate ($Ni(acac)_2$: $Mg(CH_3COO)_2$•$4H_2O$ (95:5 %V), in acetonitrile/ethanol) at 500 ^{0}C and annealed for 15 min. After cooling at room temperature, the substrates were transfer to the glove box for the deposition of other layers. 1.2M $CH_3NH_3PbI_3$ was prepared for pristine perovskite film. For $CH_3NH_3PbI_3$. z$CuCl_2$, $CuCl_2$ was added in CH_3NH_3I /PbI_2 with molar ratio of 1 (CH_3NH_3I): 1 (PbI_2): z ($CuCl_2$) (where z was varied from 1.25 to 15 mol %) in 1 mL DMF. The perovskite precursor solution was spin-coated onto the substrate at 5000 rpm for 42 s. After 12 s at 5000 rpm, an optimum amount (100 µL) of anti-solvent (toluene) was dripped on the spinning substrate and continue spinning till end. The spin coated substrates were then annealed at 100 ^{0}C for 30 min. Consequently, the electron transport layer (PCBM (20 mg mL^{-1} in chlorobenzene)) and interfacial layer (BCP (solution in methanol)) were spin-coated at 1000 rpm for 30 s and 6000 rpm for 30 s respectively. Finally, a 90 nm thick silver electrode layer was thermally evaporated under 4.65×10^{-6} Pa vacuum through a shadow mask with an active area of 0.09 cm^2.

3.2.3 Characterization

Optical absorbance spectra were measured by a UV-Vis (Shimadzu UV/Vis 3600) spectrophotometer. The surface morphology of perovskite films was observed by scanning electron microscopy (SEM) (JSM-6500F). The XRD was measured on a Rigaku RINT-2500 powder X-ray diffractometer using Cu Kα radiation.

The *J-V* characteristics were measured using a solar simulator with AM 1.5 sunlight (100mWcm^{-2}, WXS-155S-10: Wacom Denso Co., Japan). The *J-V* curves were measured by forward (-0.2V to 1.2V) scan by using the Keithley 2400. *J-V* curves for all devices were measured by masking the cells with a metal mask 0.09 cm^2 in area. The incident photon-to-current conversion efficiency (IPCE) spectra were measured with a monochromatic incident light of 1×10^{16} photons cm^{-2} in direct current mode (CEP-2000BX, Bunko-keiki). Steady-state photoluminescence (PL) was recorded by a spectrometer (Spectra Pro-300i) with an excitation by an Ar^+ laser of wavelength 514.5 nm (Stabilite 2017).

3.3 Results and Discussion

To observe the effect of $CuCl_2$ addition on the surface morphology of $CH_3NH_3PbI_3$ films, the SEM measurement was performed. The surface morphology of $CH_3NH_3PbI_3$ films at different concentration of $CuCl_2$ are shown in Figure 3.1. The pristine $CH_3NH_3PbI_3$ films showed small and inhomogeneous film morphology (Figure 3.1a). This may be due to the fast crystallization of $CH_3NH_3PbI_3$. Upon addition of 1.25 mol% $CuCl_2$, the overall grain size become larger and some grain became 0.9 to 1.2 µm but still the film was inhomogeneous (Figure 3.1b). With increasing amount of $CuCl_2$ concentration in the precursor solution up to 2.5 mol%, the corresponding $CH_3NH_3PbI_3$ films resulted in homogeneous grains with average size of 0.7 µm (Figure 3.1c). This is because, the addition of $CuCl_2$ in the precursor solution provide chloride ions which leads to the formation of intermediate phase and slow down the crystallization rate and promotes the growth of larger perovskite grains.[11] With further increment of $CuCl_2$ concentration up to 5 mol%, the morphology of $CH_3NH_3PbI_3$ film was similar to 2.5 mol% $CuCl_2$ films but showed small pores within the $CH_3NH_3PbI_3$ film (Figure 3.1d). The size of pore sizes and uncovered film morphology were increased with the increasing amount of $CuCl_2$ at 10 mol% and 15 mol% $CuCl_2$ concentration (Figures 3.1e and 3.1f).

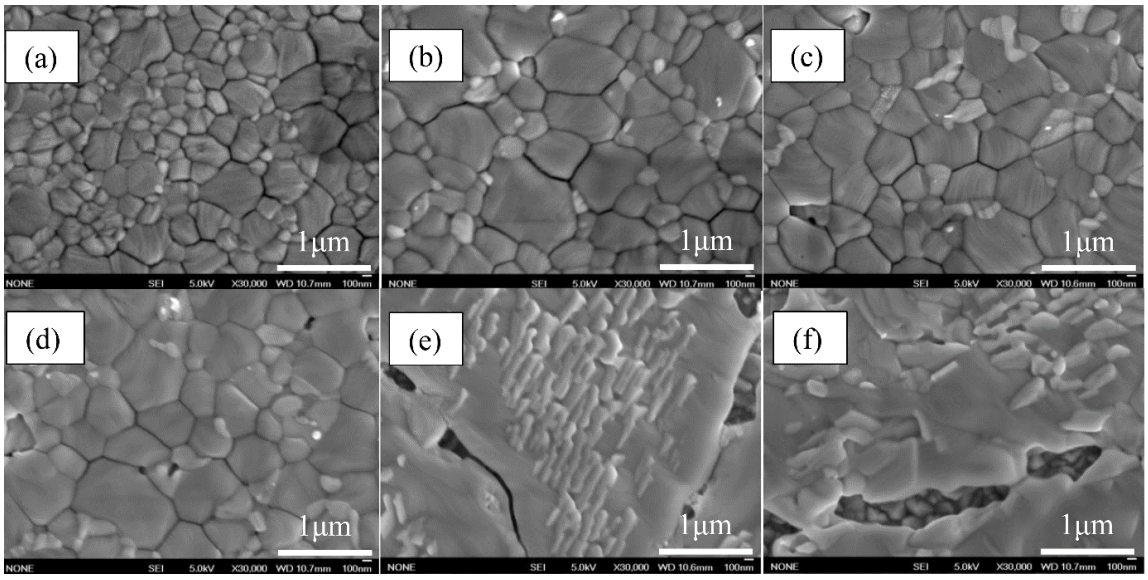

Figure 3.1. SEM images of $CH_3NH_3PbI_3$ films: (a) pristine (b) 1.25 mol% (c) 2.5 mol% (d) 5 mol% and (e) 10 mol% and (f) 15 mol% of $CuCl_2$ additive.

The performance of PSCs is directly dependent on the crystallinity of perovskite films.[5,12] Figure 3.2a shows the XRD pattern of $CH_3NH_3PbI_3$ perovskite films without and with $CuCl_2$ addition at different concentration. All the resulting films showed XRD peaks located at 14.2°, 28.5° and 31.9° corresponding to the 110, 220 and 310 crystal planes respectively for the tetragonal perovskite phase (space group *I4/mcm*).[13-16] From the XRD observation, it has been found that the intensity of the (110) peak at 2θ = 14.2° varied with $CuCl_2$ concentration in the precursor solution. The sample with 1.25 mol% $CuCl_2$ addition showed twice higher intensity and sharper as compared with pristine $CH_3NH_3PbI_3$, indicating improved crystallinity and larger crystallite size.[17] As the full width at half maximum of the diffraction peaks are inversely proportional to the crystallite size.[18] This result is also consistent with the SEM images observation. With the addition of $CuCl_2$ beyond 1.25 mol%, the XRD intensity gradually decreased. For the perovskite films with 5 mol% to 15 mol% $CuCl_2$, an extra peak at 12.6° was observed which can be assigned to the peak of PbI_2, indicating incomplete crystallization of perovskite film due to presence of excess $CuCl_2$.[19]

To observe the effect of $CuCl_2$ addition on the optoelectronic properties of $CH_3NH_3PbI_3$, the steady state photoluminescence measurement has been performed. For this measurement, the perovskite films were deposited on glass and encapsulated by using cavity glass and UV glue. Figure 3.2b shows the steady state PL spectra of the $CH_3NH_3PbI_3$ films with 2.5 mol% $CuCl_2$ and without $CuCl_2$ addition. The perovskite film without $CuCl_2$ showed relatively weak PL intensity at 774 nm whereas, the PL emission from the $CH_3NH_3PbI_3$ with 2.5 mol% $CuCl_2$ was more intense on the order of ~5. These results indicate a significant reduction in non-radiative recombination due to the formation of high quality crystals, eventually leading to lower trap states with the addition of 2.5 mol% $CuCl_2$.[20-21]

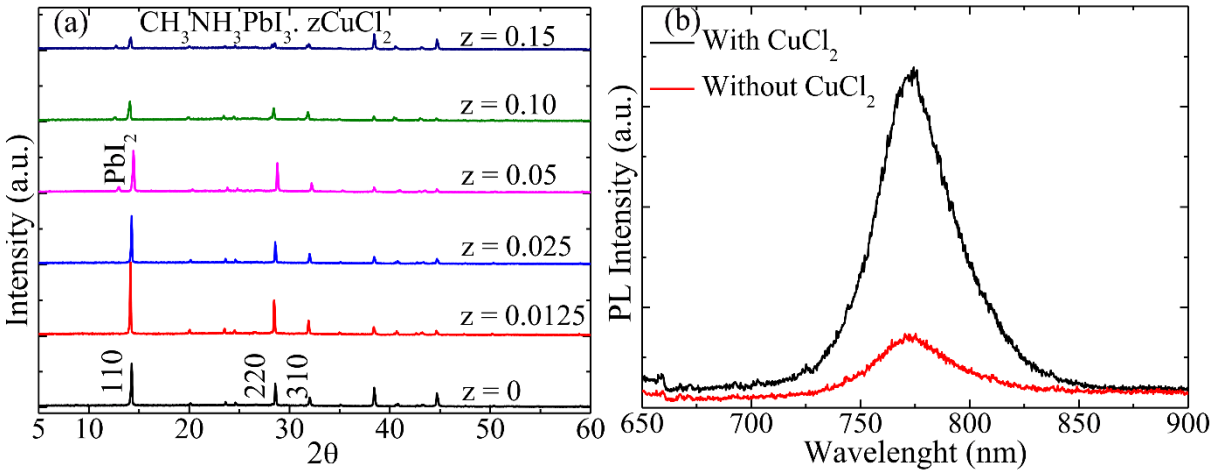

Figure 3.2. XRD pattern of $CH_3NH_3PbI_3$ films at different concentration of $CuCl_2$ (a) steady state PL spectra (b) of $CH_3NH_3PbI_3$ films of pristine and 2.5 mol% $CuCl_2$, deposited on the soda-lime glass substrate.

All the PSCs were fabricated in FTO/NiO_X/$CH_3NH_3PbI_3$.z$CuCl_2$/PCBM/BCP/Ag configuration. The IPCE spectra for the PSCs as a function of $CuCl_2$ concentration in the corresponding precursor solutions are

shown in Figure 3a and summarized in Table 3.1. The onset of the IPCE at 800 nm was consistent with the UV-vis light absorption of $CH_3NH_3PbI_3$ which is shown in supporting information (Figure S3.1). The pristine device showed poor IPCE of 60% at 590 nm wavelenght. Whereas, the PSCs formed by addition of 2.5 mol% and 5 mol% $CuCl_2$ in the $CH_3NH_3PbI_3$ precursor solutions showed highest IPCE of 76% at 590 nm wavelenght. The increased IPCE from the pristine device is due to the large and homogeneous grains structures which enhances the charge recombination resistance due to a decease in trap states which is in agreement with the PL observation. When the amount of $CuCl_2$ exceeds beyond 5 mol%, reduced pattern in the IPCE spectra were observed (40% to 60% at 15 mol% $CuCl_2$). From the SEM images, it has been observed that the addition of $CuCl_2$ increases the grain size resulting in reduced grain boundaries. This is why PSCs fabricated with 2.5 mol% - 5 mol% $CuCl_2$ in $CH_3NH_3PbI_3$ films showed higher IPCE values. As the addition of $CuCl_2$ was increased beyond 5 mol%, the lack of surface coverage by perovskite films results in lower IPCE in the respective PSCs.

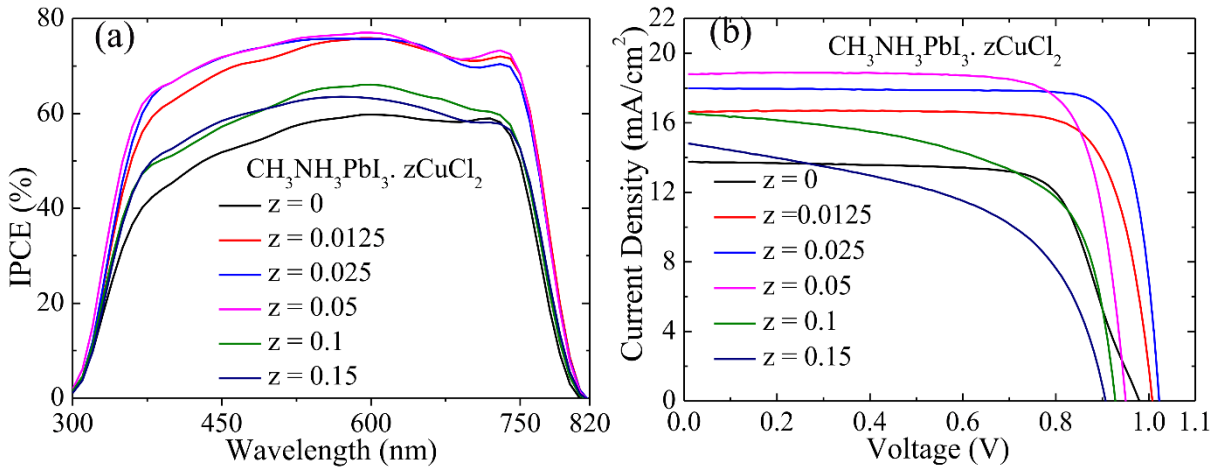

Figure 3.3. IPCE spectra(a) and J-V curves (b) for PSCs at different concentration of $CuCl_2$.

Figure 3b shows *J-V* curves for the PSCs fabricated using perovskite films with different concentration of $CuCl_2$ and the corresponding photovoltaic performance parameters are summarized in Table 3.1. The PSC without additive exhibits PCE of 9.73 % with the J_{SC} of 13.76 mA/cm^2, V_{OC} of 0.980 V, and FF of 0.72. With the addition of $CuCl_2$ in perovskite precursor solution from 1.25 mol% to 5 mol%, all the performance parameters of corresponding devices improved (Table 3.1). The PSC with 2.5 mol% $CuCl_2$ in the precursor solution, showed the best PCE of 15.22 %, with the J_{SC} of 17.99 mA/cm^2, V_{OC} of 1.022 V, and FF of 0.828. As compared with the pristine PSC, the 2.5 mol% $CuCl_2$ addition improved the J_{SC} and FF from 13.76 mA/cm^2 to 17.99 mA/cm^2 and 0.722 to 0.828 respectively.

Table 3.1: Photovoltaic Performance Parameters of PSCs at Different Concentration of $CuCl_2$ in Perovskite Precursor Solution.

Absorber layer	J_{SC} (mA/cm^2)	V_{OC} (V)	FF	PCE (%)	IPCE (%) At 590 nm
$CH_3NH_3PbI_3$	13.756	0.980	0.722	9.73	60
$CH_3NH_3PbI_3.zCuCl_2$ (z=0.0125)	16.622	1.008	0.789	13.21	76
$CH_3NH_3PbI_3.zCuCl_2$ (z=0.025)	17.988	1.022	0.828	15.22	76
$CH_3NH_3PbI_3.zCuCl_2$ (z=0.05)	18.590	0.950	0.782	13.81	76
$CH_3NH_3PbI_3.zCuCl_2$ (z=0.1)	16.556	0.928	0.617	9.47	66
$CH_3NH_3PbI_3.zCuCl_2$ (z=0.15)	14.811	0.907	0.531	7.13	63

3.4 Summary

In this work, the decisive effect of $CuCl_2$ addition on the morphology and optoelectronic properties of $CH_3NH_3PbI_3$ film from a single precursor solvent have been observed. Higher charge recombination resistance due to reduced trap states via $CuCl_2$ addition was observed in the perovskite films with an optimized 2.5 mol% $CuCl_2$ concentration in the precursor solution. Due to the positive aspects of CuCl2 addition into the precursor solution, the PCE has been boosted from 9.73% (pristine) to 15.22 % (with 2.5 mol% 2.5mol% $CuCl_2$) which is 56 % higher than the pristine $CH_3NH_3PbI_3$ based PSC. Hence, this work might be a pathway to obtain high quality perovskite films from a single solvent for large scale production.

References

(1) N.J. Jeon, J.H. Noh, Y.C. Kim, W.S. Yang, S. Ryu, S.I. Seok, Solvent Engineering for High-Performance Inorganic–Organic Hybrid Perovskite Solar Cells, *Nat. Mater.*, **2014**, 13, 897-903.

(2) Wu, Y.; Islam, A.; Yang, X.; Qin, C.; Liu, J.; Zhang, K.; Peng, W.; Han, L. Retarding the Crystallization of PbI_2 for Highly Reproducible Planar-Structured Perovskite Solar Cells Via Sequential Deposition. *Energy Environ. Sci.,* **2014,** *7*, 2934-2938.

(3) L.A. Frolova, D.V. Anokhin, K.L. Gerasimov, N.N. Dremova, P.A. Troshin, Exploring the Effects of The Pb^{2+} Substitution in $MAPbI_3$ on the Photovoltaic Performance of the Hybrid Perovskite Solar Cells, *J. Phys. Chem. Lett.,* **2016**, 7, 4353-4357

(4) Y. Zhao, K. Zhu, CH_3NH_3Cl-Assisted One-Step Solution Growth of $CH_3NH_3PbI_3$: Structure, Charge-Carrier Dynamics, and Photovoltaic Properties of Perovskite Solar Cells, *J. Phys. Chem. C*, **2014**, 118, 9412-9418.

(5) P.W. Liang, C.Y. Liao, C.C. Chueh, F. Zuo, S.T. Williams, X.K. Xin, J. Lin, A.K.Y. Jen, Additive Enhanced Crystallization of Solution - Processed Perovskite for Highly Efficient Planar - Heterojunction Solar Cells, *Adv. Mater*., **2014**, 26, 3748-3754.

(6) Y. Yang, J. Song, Y. Zhao, L. Zhu, X. Gu, Y. Gu, M. Che, Y. Qiang, Ammonium-Iodide-Salt Additives Induced Photovoltaic Performance Enhancement in One-Step Solution Process for Perovskite Solar Cells, *J Alloys Compd*., **2016**, 684, 84-90.

(7) C. Sun, Y. Guo, B. Fang, J. Yang, B. Qin, H. Duan, Y. Chen, H. Li, H. Liu, Enhanced Photovoltaic Performance of Perovskite Solar Cells Using Polymer P (Vdf-Trfe) as a Processed Additive, *J. Phys. Chem. C*, **2016**, 120, 12980-12988.

(8) J.Y. Seo, T. Matsui, J. Luo, J.P. Correa-Baena, F. Giordano, M. Saliba, K. Schenk, A. Ummadisingu, K. Domanski, M. Hadadian, Ionic Liquid Control Crystal Growth to Enhance Planar Perovskite Solar Cells Efficiency, *Adv. Energy Mater*., **2016**, 6,1600767.

(9) Wu, Y.; Xie, F.; Chen, H.; Yang, X.; Su, H.; Cai, M.; Zhou, Z.; Noda, T.; Han, L. Thermally Stable $MAPbI_3$ Perovskite Solar Cells with Efficiency of 19.19% and Area over 1 cm^2 Achieved by Additive Engineering. *Adv. Mater***, 2017,** *29*, 1701073.

(10) S.C. Watthage, Z. Song, N. Shrestha, A.B. Phillips, G.K. Liyanage, P.J. Roland, R.J. Ellingson, M.J. Heben, Enhanced Grain Size, Photoluminescence, and Photoconversion Efficiency with Cadmium Addition During the Two-Step Growth of $CH_3NH_3PbI_3$, *ACS Appl. Mater. Interfaces*, **2017**, 9, 2334-2341.

(11) S.T. Williams, F. Zuo, C.-C. Chueh, C.-Y. Liao, P.-W. Liang, A.K.-Y. Jen, Role of Chloride in the Morphological Evolution of Organo-Lead Halide Perovskite Thin Films, *ACS nano*, **2014**, 8, 10640-10654.

(12) Y. Shi, X. Wang, H. Zhang, B. Li, H. Lu, T. Ma, C. Hao, Effects of 4-Tert-Butylpyridine on Perovskite Formation and Performance of Solution-Processed Perovskite Solar Cells, *J. Mater. Chem. A*, **2015**, 3, 22191-22198.

(13) Z. Song, S.C. Watthage, A.B. Phillips, B.L. Tompkins, R.J. Ellingson, M.J. Heben, Impact of Processing Temperature and Composition on the Formation of Methylammonium Lead Iodide Perovskites, *Chem. Mater.*, **2015**, 27. 4612-4619.

(14) S. Dharani, H.K. Mulmudi, N. Yantara, P.T.T. Trang, N.G. Park, M. Graetzel, S. Mhaisalkar, N. Mathews, P.P. Boix, High Efficiency Electro spun TiO_2 Nanofiber Based Hybrid Organic-Inorganic Perovskite Solar Cell, *Nanoscale*, **2014**, 6, 1675-1679.

(15) S. Gharibzadeh, B.A. Nejand, A. Moshaii, N. Mohammadian, A.H. Alizadeh, R. Mohammadpour, V. Ahmadi, A. Alizadeh, Two - Step Physical Deposition of a Compact CuI Hole - Transport Layer and the Formation of an Interfacial Species in Perovskite Solar Cells, *ChemSusChem*, 2016, 9. 1929-1937.

(16) N. Rajamanickam, S. Kumari, V.K. Vendra, B.W. Lavery, J. Spurgeon, T. Druffel, M.K. Sunkara, Stable and Durable $CH_3NH_3PbI_3$ Perovskite Solar Cells at Ambient Conditions, *Nanotechnology*,2016, 27, 235404.

(17) Z. Zhou, X. Li, M. Cai, F. Xie, Y. Wu, Z. Lan, X. Yang, Y. Qiang, A. Islam, L. Han, Stable Inverted Planar Perovskite Solar Cells with Low-Temperature-Processed Hole-Transport Bilayer, *Adv. Energy Mater*., **2017**, 7, 1700763.

(18) A. Patterson, The Scherrer Formula for X-Ray Particle Size Determination, *Phys. Rev*., **1939**, 56, 978.

(19) Zhang, X.; Yuan, S.; Lu, H.; Zhang, H.; Wang, P.; Cui, X.; Zhang, Y.; Liu, Q.; Wang, J.; Zhan, Y. Hydrazinium Salt as Additive to Improve Film Morphology and Carrier Lifetime for High-Efficiency Planar-Heterojunction Perovskite Solar Cells via One-Step Method. *ACS Appl. Mater. Interfaces* **2017,** *9*, 36810-36816.

(20) Z. Xiao, Q. Dong, C. Bi, Y. Shao, Y. Yuan, J. Huang, Solvent Annealing of Perovskite - Induced Crystal Growth for Photovoltaic - Device Efficiency Enhancement, Adv. Mater., **2014**, 26, 6503-6509.

(21) C.-Y. Chang, K.-T. Lee, W.-K. Huang, H.-Y. Siao, Y.-C. Chang, High-Performance, Air-Stable, Low-Temperature Processed Semitransparent Perovskite Solar Cells Enabled by Atomic Layer Deposition, *Chem. Mater*., **2015**, 27, 5122-5130.

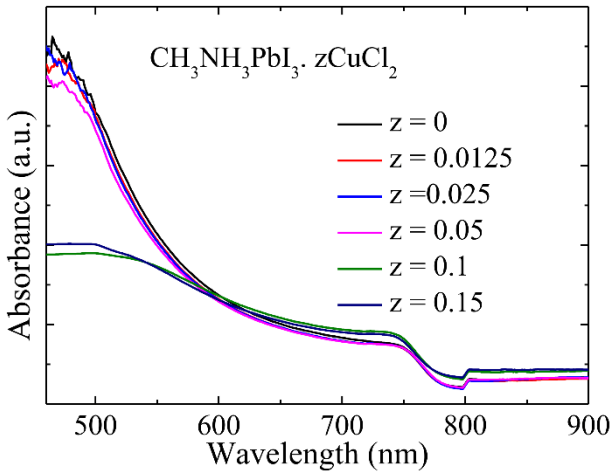

Figure S3.1. UV-vis absorbance spectra for $CH_3NH_3PbI_3$. $zCuCl_2$. z denotes the molar ratio of $CuCl_2$ to CH_3NH_3I and PbI_2 in the corresponding $CH_3NH_3PbI_3$ precursor solutions.

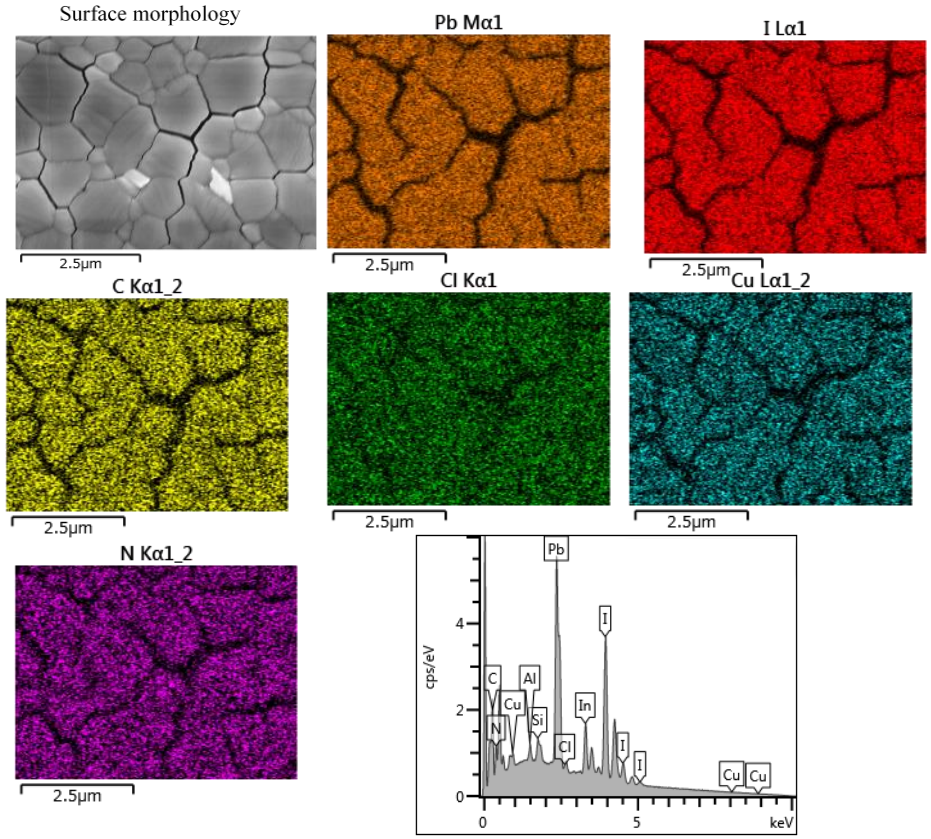

Figure S3.2. EDS mapping of different elements of $CH_3NH_3PbI_3$. $zCuCl_2$ (z=2.5 mol) film.

Table ST3.1: Atomic percentage of different elements in the $CH_3NH_3PbI_3$.$zCuCl_2$ (z=2.5 mol) film.

Element	Atomic %
N	1.92
Cl	0.03
Cu	1.09
I	59.55
Pb	37.40
Total	100.00

Chapter 4

Enhanced Photovoltaic Performance of $FASnI_3$ Based Perovskite Solar Cells with Hydrazinium Chloride (N_2H_5Cl) Coadditive

4.1 Introduction

At present, the PCE of PSCs has crossed 23% which is higher that the commercially available polycrystalline silicon solar cell.[1-2] However, all the reported high efficiency PSCs are generally constructed with Pb as the divalent metal in the perovskite compound which hinders the large-scale commercial production without any specified protocol for the vast amount of toxic Pb handling in the industrial production level. As a result, numerous researches are in constant pursuit to replace Pb with nontoxic metals such as Sn, Cu, Ge and Bi without compromising the favorable optoelectronic properties of the perovskite absorber.[3-6] Among these, Sn based halide perovskite ($ASnX_3$) has similar or even superior optoelectronic properties in comparison to Pb-based perovskites. Besides being less toxic, $ASnX_3$ perovskites contain favorable optoelectronic properties, such as- high light absorption competence, extremely high carrier mobility and bandgap of 1.2 eV-1.4 eV.[7-8] However, Sn-based perovskite compounds implemented in PSCs show poor photovoltaic performances reaching only up to 9% of PCE .[9-10] One of the reason for such limited performance is attributed to the facial tendency of oxidation from Sn^{2+} to Sn^{4+} state in Sn based perovskite film in ambient environment or even in glovebox with parts per million (ppm) level of water and oxygen (<10 ppm), which is well known as "self-doping."[3, 11-12] Due to the self-doping effect, the pure Sn-based perovskite loses suitable semiconducting properties for photovoltaic devices, leading to poor stability and reproducibility.[13] To reduce the oxidation of Sn^{2+} with semiconducting properties, the addition of SnF_2 in the precursor solution has been highlighted as a potential solution.[14] However, addition of excess SnF_2 has a tendency to form separate phase on the surface of perovskite films.[15] As a solution to prevent phase separation, pyrazine as a mediator has shown potential to effectively restrict phase separation of SnF_2.[16] Similar approaches has been undertaken by addition of hypophosphorous acid into the Sn perovskite precursor solution to prevent the SnF_2 phase separation.[17] Hence, retarding the oxidation of Sn^{2+} to Sn^{4+} is one of the main pre-requisite for efficient Sn based PSC fabrication.[18-19] However, SnF_2 addition does not effectively result in homogenous and pinhole free Sn based perovskite films. For obtaining efficient Sn based PSC, a compact and uniform perovskite film which can mitigate the penetration of oxygen into its inner domain to oxidize Sn^{2+} is much anticipated.[20] Additionally for Sn-based perovskite absorber layers, total control over the morphology is more challenging as compared to Pb-based perovskite absorber layer due to the faster reaction rate between SnI_2 and methylammonium (MAI) / formamidium iodide (FAI).[18,21] For high-quality pinhole-free Sn-based perovskite films, the formation of the intermediate SnI_2 solvates prior to final perovskite films is essential.[18] In this concern, addition of a secondary

additive with suitable functionality which can simultaneously assist to form a uniform film and retard the Sn^{2+} oxidation might be beneficial. For Pb-based perovskite films, addition of chlorine salts such as $HONH_3Cl$, GuCl, NaCl, $CdCl_2$ and N_2H_5Cl can facilitate growth of compact pinhole free perovskite layer. [22-27] In such instances, the chloride ion successfully tuned the rate of chemical reaction of perovskite film formation and assisted to form homogeneous films. Among these chlorinated salts, hydrazinium chloride (N_2H_5Cl) has been proven as effective additive for uniform film formation and widely known as a reducing agent.[27-29] However, using the dual beneficial aspects of N_2H_5Cl for uniform Sn based perovskite film growth with controlled rate provided by the chloride ion and effective suppression of Sn^{2+} oxidation has not been explored yet.

Here in this work in addition to SnF_2, the N_2H_5Cl has been added as a co-additive in a single solvent (dimethyl sulfoxide) precursor system to obtain homogeneous and pin-hole free $FASnI_3$ films with retarded Sn^{2+} oxidation. The resultant PSCs fabricated with N_2H_5Cl co-additive in $FASnI_3$ precursor showed increased shelf-life up to 1000 h. The successful inclusion of N_2H_5Cl at 2.5 mol% in the $FASnI_3$ precursor boosts the PCE up to 5.4% in an inverted planar PSC with short circuit current density (J_{SC}) of 17.64 mA cm^{-2}, open circuit voltage (V_{OC}) of 0.455 V and fill factor (FF) of 0.67.

4.2 Experimental Section

4.2.1 Materials

We have used all the chemicals as received without any further purification, including- SnI_2 (99.99%, Sigma–Aldrich), FAI (> 98%, Tokyo Chemical Industry Co., Japan), SnF_2 (>99%, Sigma-Aldrich), N_2H_5Cl (97%, Sigma-Aldrich), Poly (3,4-ethylenedioxythiophene)-poly (styrenesulfonate) (PEDOT:PSS) (Clevious P VP Al 4083), PCBM (Phenyl-C61-butyric acid methyl ester) (99.5%, Lumtec Co., Taiwan). Bathocuproine (BCP) and super dehydrated solvents of dimethyl sulfoxide (DMSO), chlorobenzene, methanol and ethanol, were purchased from Wako Co., Japan.

4.2.2 Perovskite Film Fabrication

The precursor solution for $FASnI_3$ perovskite film was prepared by mixing equaimolar ratio of (1 mmol) SnI_2 and FAI with 10 mol% SnF_2 in 1ml of DMSO solvent. For the coadditive engineered $FASnI_3$ films, the FAI was replaced with varying amount of N_2H_5Cl (0 mol%, 2.5 mol%, 5.0 mol% and 10 mol% in respect to the content of $FASnI_3$) from the precursor solution. The perovskite film was deposited by spin-coating 70µL of precursor solution at 5000 rpm for 45 s. During spin-coating, 80 µL chlorobenzene was dripped on the substrate after 17 seconds. The spin-coated films were then annealed. The annealing process was performed in two steps: at first heating at 65^0 C for 30 s and then heating at 100 ^{0}C for 15 min.

4.2.3 Solar Cell Fabrication

All the PSCs were fabricated on the patterned indium tin oxide (ITO) coated glass substrates which act as the transparent electrode. The substrates were ultrasonically cleaned with detergent, de-ionized water, acetone, and ethanol respectively for 15 min each. Before starting the device fabrication process, the cleaned substrates were treated with ultraviolet (UV)/ozone radiation for 30 min. The hole transport layer (HTL) was deposited on top of the ITO substrate by spin-coating 70µL of PEDOT:PSS solution at 1000 rpm and 4000 rpm for 10 s and 30 s respectively. The PEDOT:PSS films were then annealed at 150 ^{0}C for 15 min and cooled down to room temperature. After cooling at room temperature, the substrates were transferred to glove box and the $FASnI_3$ perovskite films were deposited. An electron transporting layer PCBM (20 mg ml^{-1} in chlorobenzene) and BCP (saturated solution in isopropanol) were deposited by spin-coating at 1000 rpm for 30 s and 6000 rpm for 30 s respectively. Finally, a 90 nm thick silver layer was vacuum deposited through a shadow mask with an active area of 0.09 cm^2. The PSCs were sealed, by a cavity glass using UV curable glue on top of the front active area of ITO.

4.2.4 Characterization

The optical absorption spectra were measured by a Shimadzu UV/Vis 3600 spectrophotometer. The morphology of the films and structure of devices were observed by scanning electron microscope (JSM-6500F field-emission under an acceleration voltage of 5 kV). The XRD was measured by a Rigaku RINT-2500 powder X-ray diffractometer using Cu Kα radiation. X-ray photoelectron spectroscopy (XPS) was performed on the film deposited on glass substrate by using PHI Quantera SXM (ULVAC- PHI). XPS measurement was carried out at ultrahigh vacuum as high as $5x10^{-11}$ mbar. X-ray from monochromatic Al Kα source (hυ =1486.7 eV) was used to excite the samples and electrons were detected at 45^o take off angle. Multi pack software was used for curve fitting. Steady state photoluminescence (PL) and time resolve photoluminescence (TRPL) were measured by a Hamamatsu C12132 fluorescence lifetime spectrometer using a 1.5 ns pulsed laser (frequency 15 kHz), at an excitation wavelength of λ=532 nm, and an excitation power of 1 mW. For PL and TRPL measurement, the relevant films were deposited on glass substrates and encapsulated in glovebox but were measured in ambient conditions. The current density-voltage (*J-V)* curves were measured using a solar simulator with standard air mass 1.5 sunlight (100mWcm^{-2}, WXS-155S-10: Wacom Denso Co., Japan) under ambient conditions. The *J-V* curves were measured in forward (-0.1V to 0.5V) or reverse (0.5V to -0.1V) scans by using the Keithley 2400 as a digital source meter. The step voltage was fixed at 10mV and the delay time was set at 50 ms. *J-V* curves for all devices were measured by masking the cells with a metal mask 0.09 cm^2 in area. A monochromatic incident light ($1x10^{16}$ photons/cm^2) in direct current mode (CEP-2000BX, Bunkoukeiki Co., LTD) was used to measure monochromatic incident photon-to-current conversion efficiency (IPCE) spectra. The stability (shelf-life) of the fabricated PSCs were measured in ambient environment and stored in N_2 filled glove box after measurement.

4.3 Results and Discussion

Hydrazine compounds are well explored reducing agents which decomposes based on the following equation and shows their reductive action.[31]

$$2N_2H_4 \rightarrow 2NH_3 + N_2 + H_2 + e^- \ldots\ldots\ldots\ldots (1)$$

$$Sn^{2+} \rightleftharpoons Sn^{4+} + 2e^- \ldots\ldots\ldots\ldots\ldots\ldots\ldots\ldots (2)$$

From equation 1, hydrazine dissociates into the solution and releases electrons which suppress the Sn^{2+} oxidation reaction (Equation 2). To evaluate the anti-oxidant properties of N_2H_5Cl, the precursor solution of $FASnI_3$ with SnF_2 and $SnF_2 + N_2H_5Cl$ (5 mol%) respectively were prepared and exposed the solution in ambient air. Initially, both of the precursor solutions exhibited light yellow color (Figure 4.1). After 2 hours exposure in ambient air, a dark red colored ring formed at the surface of the precursor solution resulting in oxidation of Sn^{2+} to Sn^{4+}. With increasing exposure time, the ring extended into the solution and after 8 hours, the solution without co-additive turned dark red whereas, the N_2H_5Cl added solution still maintained light yellow color solution. Hence, addition of N_2H_5Cl into the precursor solution decelerates the oxidation rate of Sn^{2+} to Sn^{4+} in the $FASnI_3$ precursor solution.

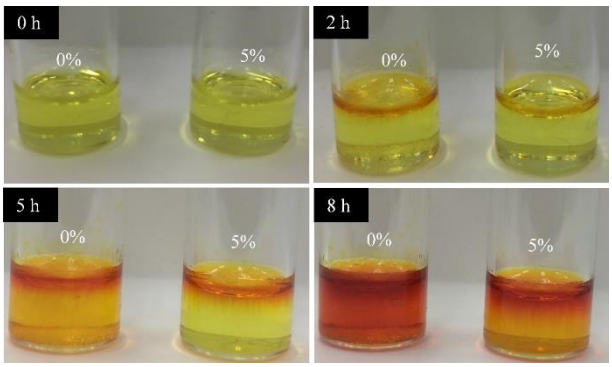

Figure 4.1. Photographic images of $FASnI_3$ precursor solution (1 mmol SnI_2, 1 mmol FAI and 0.1 mmol SnF_2) and SnF_2+5 mol% N_2H_5Cl exposed in air for different period of time.

In order to fabricate high quality $FASnI_3$ films, the retardation of crystallization process is beneficial. Specially for Sn-based perovskite as their crystallization rate are much faster than Pb-based counter part due to their higher Lewis acidity.[30] In this regard, DMSO solvent which has higher coordination affinity and lower saturated vapor pressure compared to DMF is used for Sn based perovskite films formation.[31] A recent study has shown that DMSO forms a transitional SnI_2.3DMSO intermediate phase which can facilitate decelerating perovskite formation rate and result in uniform Sn based perovskite film.[18] Hence, in this study, only DMSO has been used as precursor solvent to fabricate $FASnI_3$ films.

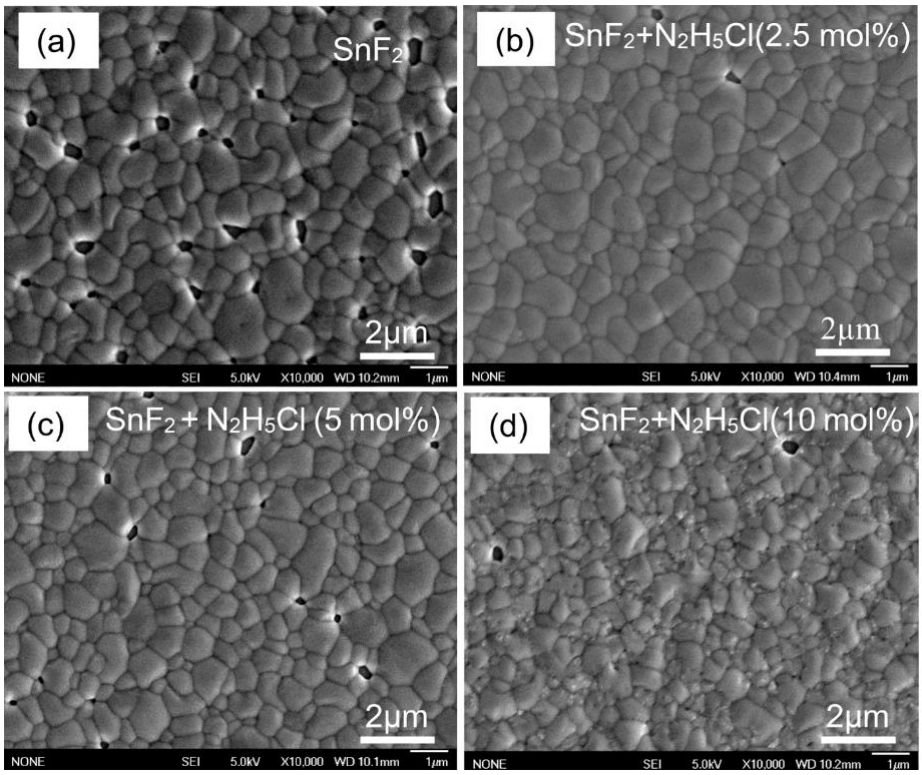

Figure 4.2. SEM images of $FASnI_3$ films: (a) SnF_2 (b) SnF_2 +2.5 mol% N_2H_5Cl (c) SnF_2 + 5 mol% N_2H_5Cl and (d) SnF_2 + 10 mol% of N_2H_5Cl.

To observe the effects of N_2H_5Cl on the morphology of $FASnI_3$ film, scanning electron microscopy (SEM) images have been taken for $FASnI_3$ at various concentration of N_2H_5Cl (Figure 4.2). The $FASnI_3$ films fabricated with SnF_2 additive exhibits very poor coverage with numerous pinholes over Poly (3,4-ethylenedioxythiophene)-poly (styrenesulfonate) (PEDOT:PSS) hole transport layer (Figure 4.2a). Upon addition of 2.5 mol% N_2H_5Cl, the surface morphology significantly improves with high coverage over the PEDOT:PSS under layer. The corresponding film showed larger grains with an average of 675 nm (Figure 4.2b, Figure S4.1). By the addition of N_2H_5Cl, the chloride ions in this additive led to formation of an intermediate fused template phase of perovskite which acts as seeds and directs the growth of larger $FASnI_3$ grains with full coverage.[32] The rapid decrease of pin-holes and formation of larger grains in the $FASnI_3$ film results in reduced grain boundary defects. Further increased concentration of N_2H_5Cl up to 5 mol%, the grain sizes decreased to an average of 0.55 μm (Figure S4.1) and increased the number of pin-holes in the corresponding $FASnI_3$ films (Figure 4.2c). However, with increased N_2H_5Cl concentration up to 10 mol%, resulted in 0.39 μm average grain sizes with some white dot particles on the surface of $FASnI_3$ film (Figure 4.2d).

The figure 4.3 shows X-ray diffraction pattern for $FASnI_3$ films with SnF_2 and SnF_2 + various concentration of N_2H_5Cl. All the XRD pattern showed similar characteristics of XRD peaks located at 14.1, 24.5, 28.3, 31.8, 40.50, and 42.9°, which can be assigned to 100, 102, 200, 122, 222, and 213 crystal planes, respectively, for the orthorhombic perovskite phase. Interestingly, by addition of N_2H_5Cl, the full width at half maxima of peak at 14.1^0 becomes narrower (0.145 for only SnF_2 and 0.110 for SnF_2 + 2.5 mol% N_2H_5Cl added

$FASnI_3$ films) (see Table S4.1). This may be due to the significant enhancement of crystallinity of $FASnI_3$ films with the addition of N_2H_5Cl.

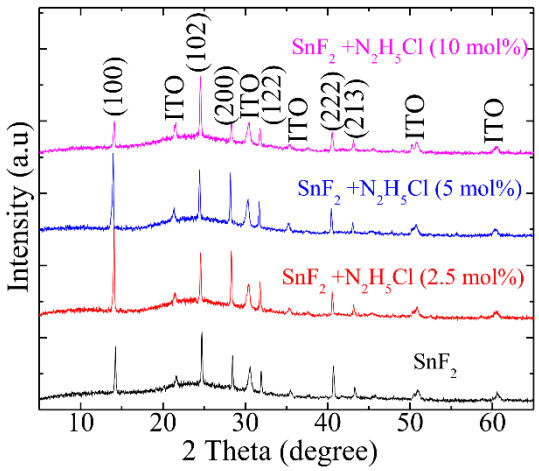

Figure 4.3. XRD patterns of $FASnI_3$ films at various concentrations of N_2H_5Cl deposited on ITO coated glass substrate.

The UV-Vis absorption spectra have been performed to observe the effect of N_2H_5Cl addition on the absorption band edge of $FASnI_3$ films (Figure S4.2). The bandgap of the respective $FASnI_3$ films have been determined from Tauc plot. From the results, it has found that all $FASnI_3$ films showed 1.37 eV except the 10 mol% of N_2H_5Cl added film. The $FASnI_3$ film with 10 mol% N_2H_5Cl showed 1.39 eV which may be due to the substitution of FA or I with N_2H_4 or Cl respectively.

X-ray photoelectron spectroscopy **(**XPS) measurement has been performed to evaluate the reducing effects of N_2H_5Cl addition as a co-additive on $FASnI_3$ films (Figure 4.4 a, b.). The two main peaks at 495.3 eV and 486.9 eV were assigned to $3d_{3/2}$ and $3d_{5/3}$ for Sn^{2+} respectively. Whereas the fitting peaks situated at 595.9 eV and 487.5 eV were ascribed as the binding energy of Sn^{4+}. To determine the relative amount of Sn^{2+} and Sn^{4+} in the $FASnI_3$ film, the XPS spectra were deconvoluted by curve fitting. The curve fitting was performed by using Multi-Pack software. The detail fitting results are given in table S4.2. The fitting results showed the atomic percent of Sn^{4+} were 7.3 and 4.9 for only SnF_2 and SnF_2+N_2H_5Cl added $FASnI_3$ films respectively. This result indicates that the addition of 2.5 mol% N_2H_5Cl in the perovskite precursor solution reduced the Sn^{4+} content from 7.3 to 4.9 atomic percent (see Table S4.2 and S4.3). Hence, confirming the ability of N_2H_5Cl to retard the oxidation of Sn^{2+} in the $FASnI_3$ films which is in accord with the results observed from the precursor solution test observation (Figure 4.1). In Sn based perovskite films, Sn^{4+} is considered as the Sn vacancies.[17]

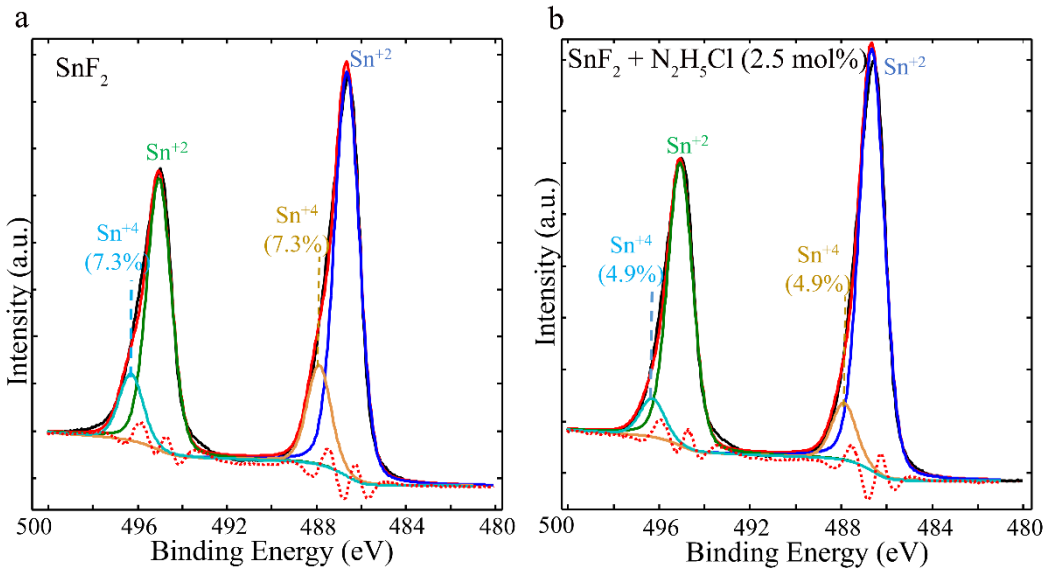

Figure 4.4. High-resolution XPS spectra (Sn 3d) of $FASnI_3$ thin films of (a) SnF_2 and (b) SnF_2 + 2.5 mol% N_2H_5Cl.

To understand the charge dynamics of SnF_2 and SnF_2 + 2.5 mol% N_2H_5Cl based $FASnI_3$ films, steady state PL and time resolved PL were performed and shown in Figure 4.5a and 4.5b. $FASnI_3$ film with 2.5 mol% N_2H_5Cl shows a PL peak with a small blue shift from 900 nm to 895 nm in comparison to only SnF_2 based $FASnI_3$ film (without N_2H_5Cl). This blue shift in the PL peak, which is also observed in the absorption spectra, indicates that the addition of N_2H_5Cl passivates the defect states just below the conduction band. Figure 4.5b shows the TRPL spectra for the SnF_2 and SnF_2 + 2.5 mol% N_2H_5Cl added $FASnI_3$ films. The 2.5 mol% N_2H_5Cl added $FASnI_3$ film showed relatively longer PL lifetime (τ = 4.83 ns) compared to only SnF_2 added $FASnI_3$ film (τ = 3.53 ns), assuming a first order decay (single exponential decay). This increase of the PL lifetime indicates a reduction of charge recombination in the $FASnI_3$ film fabricated with N_2H_5Cl additives. This may be due to the formation of pin-hole free larger grains films and reduced Sn^{4+} content as deduced from the SEM and XPS measurements respectively.

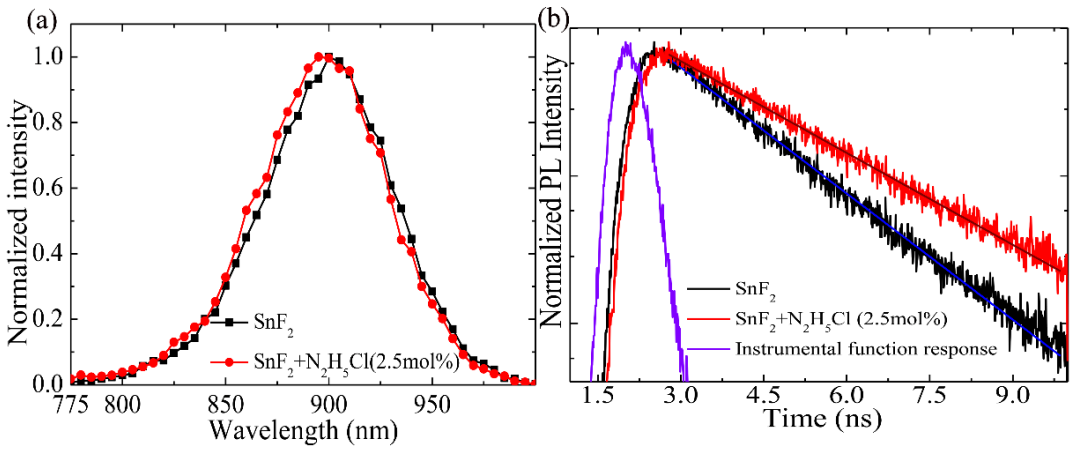

Figure 4.5. Steady state photoluminescence (PL) (a) time-resolved photoluminescence (TRPL) (b) of $FASnI_3$ films with only SnF_2 and SnF_2+N_2H_5Cl.

Inverted planar PSCs with a structure of ITO/PEDOT:PSS/$FASnI_3$/PCBM/BCP/Ag were fabricated to evaluate the photovoltaic performance of the $FASnI_3$ films. The schematic device structure and the cross-sectional SEM image of the fabricated device are shown in Figure S4.3. Figure 4.6a shows the current density-voltage *(J-V)* curves of the fabricated PSCs measured under AM 1.5 simulation (100 $mWcm^{-2}$ illumination) in forward bias mode and the corresponding photovoltaic parameters are shown in Table 4.1. The champion SnF_2 based PSC exhibited PCE of 2.5% with photovoltaic parameters of J_{SC} = 15.1 $mAcm^{-2}$, V_{OC} = 0.297 V and FF = 0.56. The PCE for this PSC is comparable with the previously reported DMSO based PSC. [27] For SnF_2 +2.5 mol% N_2H_5Cl based PSC, a high PCE of 5.4% has been observed with J_{SC} of 17.64 $mAcm^{-2}$, V_{OC} of 0.455V and FF of 0.67. This improvement in PCE is twice higher compared to only SnF_2 based PSC. The co-addition of 2.5 mol% N_2H_5Cl results in improved FF from 0.559 (SnF_2) to 0.673 (SnF_2+2.5 mol% N_2H_5Cl). With further increase of N_2H_5Cl concentration in the precursor solution, reduced PCE of corresponding PSCs has been observed (see in Table 4.1). The higher V_{OC} in the PSC using N_2H_5Cl as a co-additive can be explained by means of reduced background carrier density which causes the recombination loss. The presence of Sn^{4+} is known as the primary source of background carrier density[14, 33] which is suppressed by the addition of N_2H_5Cl as confirmed by the XPS results (Figure 4.4a and 4.4b). The improvement of FF mainly depends on the formation of pin-hole free uniform perovskite film which can effectively result in defect free interface with the corresponding electron transport layer.[34]The PCE of the champion PSC (5 mol% N_2H_5Cl) was 4.08% with J_{SC} of 16.13 mA cm^{-2}, V_{OC} of 0.388 V and FF of 0.65. Further increased concentration of N_2H_5Cl by 10 mol% resulted in reduced PCE of 1.84 %. This may be due to the formation of pin-holes and reduced grain size of perovskite films as observed from the SEM image (Figure 4.2d). We have also studied the hysteresis behavior of PSCs with various concentrations of N_2H_5Cl; as shown in Figure S4.4. For only SnF_2 added PSCs, we observed a distinct change in PCE from 2.5% to 0.61% during reverse scan (0.5 V to -0.1V). In contrast, this photocurrent hysteresis nearly disappeared for the PSCs fabricated by the addition of N_2H_5Cl as co-additive with SnF_2. This may be due to the elimination of charge trap states such as Sn vacancies or pin-holes by the addition of N_2H_5Cl which are known as the origin of photocurrent hysteresis.[35] Figure 4.6b shows the IPCE

spectra of the corresponding PSCs. Only SnF_2 added $FASnI_3$ based PSC showed 40% IPCE at 820 nm and maximum 60% at 520 nm. Whereas the PSC fabricated with 2.5 mol% N_2H_5Cl as co-additive with SnF_2 showed increased IPCE of 50% at 820 nm and 70% at 520 nm. The enhancement of IPCE of PSCs with the addition of N_2H_5Cl is due to the improvement of carrier recombination resistance of the $FASnI_3$ film. This result is also in accord with our TRPL results observed for 2.5 mol% N_2H_5Cl + SnF_2 resultant $FASnI_3$ films (Figure 4.5b). 5 mol% N_2H_5Cl + SnF_2 based PSC showed 40% IPCE at 820 nm and about 70% at 520 nm but for 10 mol% N_2H_5Cl addition, the IPCE was lower than the SnF_2 based PSC. The IPCE at 820 nm reduced to 22% and 30% at 520 nm.

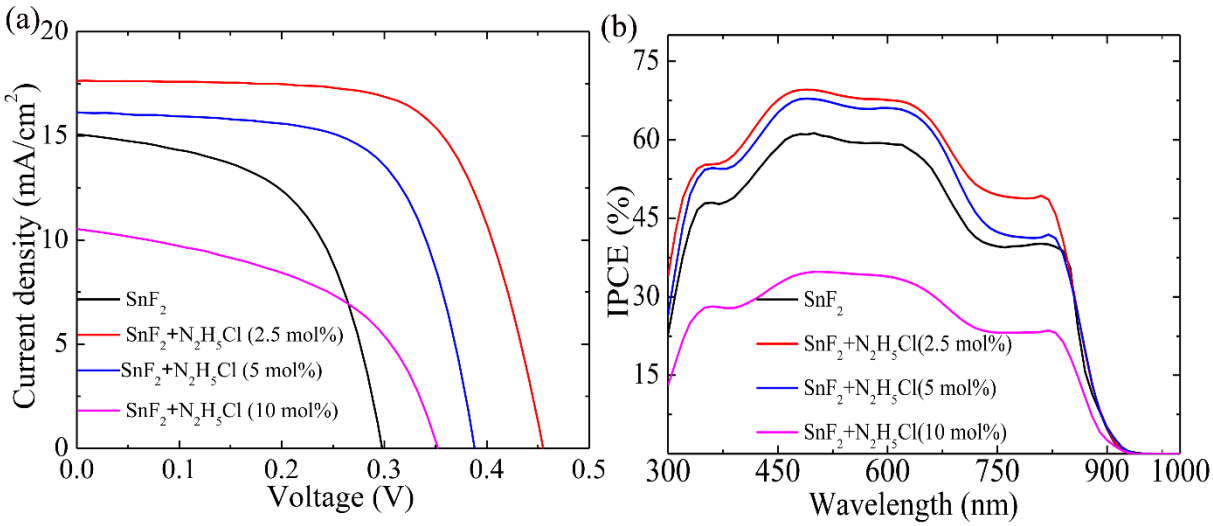

Figure 4.6. *J-V* curves(a) and incident photon-to-electron conversion efficiency (IPCE) (b) of SnF_2 and SnF_2+2.5 mol% N_2H_5Cl added $FASnI_3$ based PSCs.

Table 4.1. Photovoltaic performance parameters of PSCs at various concentrations of N_2H_5Cl in the perovskite precursor solution.

N_2H_5Cl concentration mol%	Remarks of the PSCs	J_{SC} (mA cm^{-2})	V_{OC} (V)	F.F.	PCE (%)
0	Average	14.78±1.9	0.302±0.4	0.474±0.1	2.08±0.50
	Champion	15.069	0.297	0.559	2.50
2.5	Average	16.60±1.34	0.433±0.033	0.655±0.025	4.72±0.76
	Champion	17.637	0.455	0.673	5.40
5	Average	15.81±1.88	0.386±0.018	0.616±0.038	3.75±0.53
	Champion	16.128	0.388	0.652	4.08
10	Average	8.87±1.63	0.283±0.051	0.549±0.06	1.34±0.40
	Champion	10.53	0.351	0.497	1.84

Figure 4.7a shows the shelf-life of SnF_2 and SnF_2 + 2.5 mol% N_2H_5Cl added $FASnI_3$ based PSCs stored in N_2 filled glovebox. The PSCs with 2.5 mol% N_2H_5Cl retains 65 % of its initial PCE after 1000 hours.

The PCE of only SnF_2 added PSC degraded quickly and eventually showed no photovoltaic response after 850 hours. Figure 4.7d shows the statistical histogram of PCEs for 10 individual PSCs fabricated with SnF_2 and SnF_2+2.5 mol% N_2H_5Cl based $FASnI_3$ films. The SnF_2 + 2.5 mol% N_2H_5Cl based PSCs yielded an excellent reproducibility with high PCE.

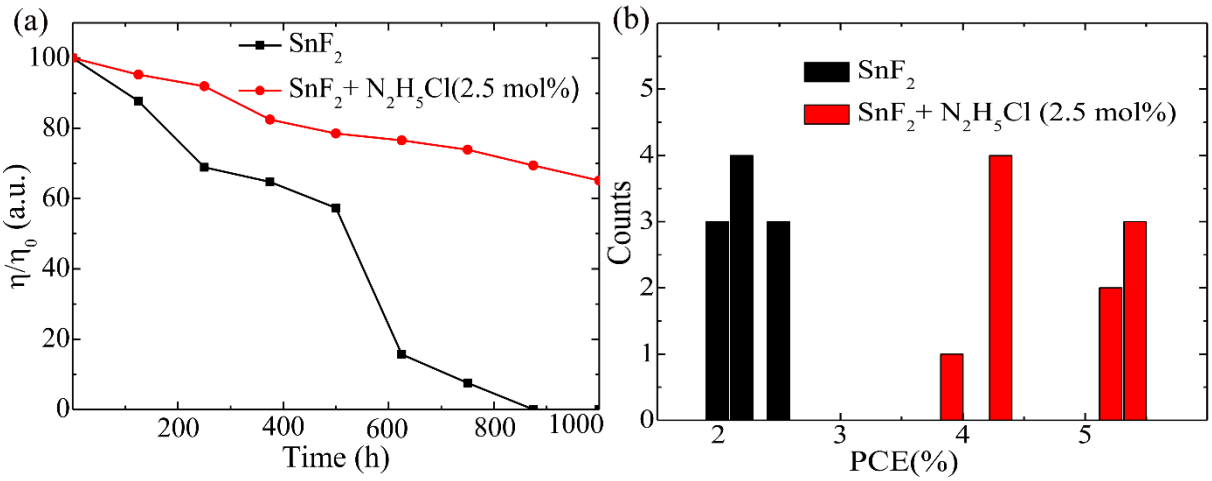

Figure 4.7. Shelf-life stability of SnF_2 and SnF_2+various concentration of N_2H_5Cl based PSCs (a) and Histogram of PCE of SnF_2 and SnF_2+2.5 mol% N_2H_5Cl added $FASnI_3$ based PSCs (b).

4.4 Summary

In this work, we have demonstrated that incorporation of N_2H_5Cl into the $FASnI_3$ precursor solution with SnF_2 effectively suppresses the oxidation of Sn^{2+} and assist the formation of uniform pin-hole free perovskite films. The inclusion of 2.5 mol% N_2H_5Cl at the $FASnI_3$ precursor solution resulted in perovskite films with less Sn^{4+} and longer charge carrier lifetime. As a result, the power conversion efficiency improved to 5.40% with V_{OC} of 0.46 V and FF of 0.67. Moreover, due to the high-quality film morphology and improved crystallinity, the best device retained 65 % of its initial PCE up to 1000 h. This work highlights the viability of N_2H_5Cl as a co-additive for the growth of high quality $FASnI_3$ films for Sn based PSCs and brings the application of non-toxic perovskite absorbers one step closer.

References

(1) Kojima, A.; Teshima, K.; Shirai, Y.; Miyasaka, T. Organometal halide perovskites as visible-light sensitizers for photovoltaic cells. *J. Am. Chem. Soc.* **2009,** *131*, 6050-6051.

(2) Green, M. A.; Hishikawa, Y.; Dunlop, E. D.; Levi, D. H.; Hohl-Ebinger, J.; Ho-Baillie, A. W. Y. Solar cell efficiency tables (version 51). *Prog Photovolt Res Appl.* **2018,** *26*, 3-12.

(3) Chung, I.; Song, J.-H.; Im, J.; Androulakis, J.; Malliakas, C. D.; Li, H.; Freeman, A. J.; Kenney, J. T.; Kanatzidis, M. G. $CsSnI_3$: semiconductor or metal? High electrical conductivity and strong near-infrared photoluminescence from a single material. High hole mobility and phase-transitions. *J. Am. Chem. Soc.* **2012,** *134*, 8579-8587.

(4) Cortecchia, D.; Dewi, H. A.; Yin, J.; Bruno, A.; Chen, S.; Baikie, T.; Boix, P. P.; Grätzel, M.; Mhaisalkar, S.; Soci, C. Lead-free $MA_2CuCl_xBr_{4-x}$ hybrid perovskites. *Inorg. Chem.* **2016,** *55*, 1044-1052.

(5) Krishnamoorthy, T.; Ding, H.; Yan, C.; Leong, W. L.; Baikie, T.; Zhang, Z.; Sherburne, M.; Li, S.; Asta, M.; Mathews, N. Lead-free germanium iodide perovskite materials for photovoltaic applications. *J. Mater. Chem. A* **2015,** *3*, 23829-23832.

(6) Slavney, A. H.; Hu, T.; Lindenberg, A. M.; Karunadasa, H. I. A bismuth-halide double perovskite with long carrier recombination lifetime for photovoltaic applications. *J. Am. Chem. Soc.,* **2016,** *138*, 2138-2141.

(7) Stoumpos, C. C.; Malliakas, C. D.; Kanatzidis, M. G. Semiconducting tin and lead iodide perovskites with organic cations: phase transitions, high mobilities, and near-infrared photoluminescent properties. *Inorg. Chem.* **2013,** *52*, 9019-9038.

(8) Shockley, W.; Queisser, H. J. Detailed balance limit of efficiency of p-n junction solar cells. *J. Appl. Phys.,* **1961,** *32*, 510-519.

(9) Noel, N. K.; Stranks, S. D.; Abate, A.; Wehrenfennig, C.; Guarnera, S.; Haghighirad, A.-A.; Sadhanala, A.; Eperon, G. E.; Pathak, S. K.; Johnston, M. B. Lead-free organic–inorganic tin halide perovskites for photovoltaic applications. *Energy Environ. Sci.,* **2014,** *7*, 3061-3068.

(10) Shao, S.; Liu, J.; Portale, G.; Fang, H. H.; Blake, G. R.; ten Brink, G. H.; Koster, L. J. A.; Loi, M. A. Highly Reproducible Sn-Based Hybrid Perovskite Solar Cells with 9% Efficiency. *Adv. Energy Mater.,* **2018,** *8*, 1702019.

(11) Takahashi, Y.; Hasegawa, H.; Takahashi, Y.; Inabe, T. Hall mobility in tin iodide perovskite $CH_3NH_3SnI_3$: evidence for a doped semiconductor. *J. Solid State Chem.,* **2013,** *205*, 39-43.

(12) Iefanova, A.; Adhikari, N.; Dubey, A.; Khatiwada, D.; Qiao, Q. Lead free $CH_3NH_3SnI_3$ perovskite thin-film with *p*-type semiconducting nature and metal-like conductivity. *AIP Adv.,* **2016,** *6*, 085312.

(13) Hao, F.; Stoumpos, C. C.; Cao, D. H.; Chang, R. P.; Kanatzidis, M. G. Lead-free solid-state organic–inorganic halide perovskite solar cells. *Nat. Photonics,* **2014,** *8*, 489.

(14) Kumar, M. H.; Dharani, S.; Leong, W. L.; Boix, P. P.; Prabhakar, R. R.; Baikie, T.; Shi, C.; Ding, H.; Ramesh, R.; Asta, M. Lead‐free Halide Perovskite Solar Cells with High Photocurrents Realized Through Vacancy Modulation. *Adv. Mater.,* **2014,** *26*, 7122-7127.

(15) Liao, W.; Zhao, D.; Yu, Y.; Grice, C. R.; Wang, C.; Cimaroli, A. J.; Schulz, P.; Meng, W.; Zhu, K.; Xiong, R. G. Lead-Free Inverted Planar Formamidinium Tin Triiodide Perovskite Solar Cells Achieving Power Conversion Efficiencies up to 6.22%. *Adv. Mater.,* **2016,** *28*, 9333-9340.
(16) Lee, S. J.; Shin, S. S.; Kim, Y. C.; Kim, D.; Ahn, T. K.; Noh, J. H.; Seo, J.; Seok, S. I. Fabrication of Efficient Formamidinium Tin Iodide Perovskite Solar Cells through Snf_2–Pyrazine Complex. *J. Am. Chem. Soc.,* **2016,** *138*, 3974-3977.
(17) Li, W.; Li, J.; Li, J.; Fan, J.; Mai, Y.; Wang, L. Addictive-Assisted Construction of all-Inorganic $CsSnIBr_2$ Mesoscopic Perovskite Solar Cells With Superior Thermal Stability up to 473 K. *J. Mater. Chem., A* **2016,** *4*, 17104-17110.
(18) Hao, F.; Stoumpos, C. C.; Guo, P.; Zhou, N.; Marks, T. J.; Chang, R. P.; Kanatzidis, M. G. Solvent-Mediated Crystallization of $CH_3NH_3SnI_3$ Films for Heterojunction Depleted Perovskite Solar Cells. *J. Am. Chem. Soc.,* **2015,** *137*, 11445-11452.
(19) Yokoyama, T.; Cao, D. H.; Stoumpos, C. C.; Song, T.-B.; Sato, Y.; Aramaki, S.; Kanatzidis, M. G. Overcoming Short-Circuit in Lead-Free $CH_3NH_3SnI_3$ Perovskite Solar Cells via Kinetically Controlled Gas–Solid Reaction Film Fabrication Process. *J. Phys. Chem. Lett.,* **2016,** *7*, 776-782.
(20) Dang, Y.; Zhou, Y.; Liu, X.; Ju, D.; Xia, S.; Xia, H.; Tao, X. Formation of Hybrid Perovskite Tin Iodide Single Crystals by Top-Seeded Solution Growth. *Angew. Chem. Int. Ed.,* **2016,** *55*, 3447-3450.
(21) Liang, K.; Mitzi, D. B.; Prikas, M. T. Synthesis and Characterization of Organic− Inorganic Perovskite Thin Films Prepared using a Versatile Two-Step Dipping Technique. *Chem. Mater.,* **1998,** *10*, 403-411.
(22) Dong, G.-h.; Ye, T.-l.; Pang, B.-y.; Yang, Y.-l.; Sheng, L.; Shi, Y.; Fan, R.-q.; Wei, L.-g.; Su, T. $HONH_3Cl$ Optimized $CH_3NH_3PbI_3$ Films for Improving Performance of Planar Heterojunction Perovskite Solar Cells Via a One-Step Route. *Phys. Chem. Chem. Phys.,* **2016,** *18*, 26254-26261.
(23) Hou, X.; Hu, Y.; Liu, H.; Mei, A.; Li, X.; Duan, M.; Zhang, G.; Rong, Y.; Han, H. Effect of Guanidinium on Mesoscopic Perovskite Solar Cells. *J. Mater. Chem., A* **2017,** *5*, 73-78.
(24) Lee, H.; Kim, A.; Kwon, H.-C.; Yang, W.; Oh, Y.; Lee, D.; Moon, J. Retarding Crystallization during Facile Single Coating of NaCl-Incorporated Precursor Solution for Efficient Large-Area Uniform Perovskite Solar Cells. *ACS Appl. Mater. Interfaces,* **2016,** *8*, 29419-29426.
(25) De Marco, N.; Zhou, H.; Chen, Q.; Sun, P.; Liu, Z.; Meng, L.; Yao, E.-P.; Liu, Y.; Schiffer, A.; Yang, Y. Guanidinium: A Route to Enhanced Carrier Lifetime and Open-Circuit Voltage in Hybrid Perovskite Solar Cells. *Nano Lett.* **2016,** *16*, 1009-1016.
(26) Watthage, S. C.; Song, Z.; Shrestha, N.; Phillips, A. B.; Liyanage, G. K.; Roland, P. J.; Ellingson, R. J.; Heben, M. J. Enhanced Grain Size, Photoluminescence, and Photoconversion Efficiency with Cadmium addition during the Two-Step Growth of $CH_3NH_3PbI_3$. *ACS Appl. Mater. Interfaces,* **2017,** *9*, 2334-2341.
(27) Zhang, X.; Yuan, S.; Lu, H.; Zhang, H.; Wang, P.; Cui, X.; Zhang, Y.; Liu, Q.; Wang, J.; Zhan, Y. Hydrazinium Salt as Additive to Improve Film Morphology and Carrier Lifetime for High-Efficiency Planar-Heterojunction Perovskite Solar Cells via One-Step Method. *ACS Appl. Mater. Interfaces,* **2017,** *9*, 36810-36816.

(28) Bye, R. Critical Examination of Some Common Reagents for Reducing Selenium Species in Chemical Analysis. *Talanta,* **1983,** *30*, 993-996.
(29) Miki, H., Method for Producing Copper Powder. Google Patents: 1998.
(30) Zhang, S.; Audebert, P.; Wei, Y.; Al Choueiry, A.; Lanty, G.; Bréhier, A.; Galmiche, L.; Clavier, G.; Boissiere, C.; Lauret, J.-S. Preparations and Characterizations of Luminescent two Dimensional Organic-Inorganic Perovskite Semiconductors. *Materials,* **2010,** *3*, 3385-3406.
(31) Wu, Y.; Islam, A.; Yang, X.; Qin, C.; Liu, J.; Zhang, K.; Peng, W.; Han, L. Retarding the Crystallization of PbI_2 for Highly Reproducible Planar-Structured Perovskite Solar Cells via Sequential Deposition. *Energy Environ. Sci.,* **2014,** *7*, 2934-2938.
(32) Williams, S. T.; Zuo, F.; Chueh, C.-C.; Liao, C.-Y.; Liang, P.-W.; Jen, A. K.-Y. Role of Chloride in the Morphological Evolution of Organo-Lead Halide Perovskite Thin Films. *ACS nano.,* **2014,** *8*, 10640-10654.
(33) Xu, P.; Chen, S.; Xiang, H.-J.; Gong, X.-G.; Wei, S.-H. Influence of Defects and Synthesis Conditions on The Photovoltaic Performance of Perovskite Semiconductor $CsSnI_3$. *Chem. Mater.,* **2014,** *26,* 6068-6072.
(34) Ye, J.; Zhang, X.; Zhu, L.; Zheng, H.; Liu, G.; Wang, H.; Hayat, T.; Pan, X.; Dai, S. Enhanced Morphology and Stability of High-Performance Perovskite Solar Cells with Ultra-Smooth Surface and High Fill Factor via Crystal Growth Engineering. *Sustainable Energy Fuels,* **2017,** *1*, 907-914.
(35) Jena, A. K.; Kulkarni, A.; Ikegami, M.; Miyasaka, T. Steady State Performance, Photo-Induced Performance Degradation and Their Relation to Transient Hysteresis in Perovskite Solar Cells. *J. Power Sources,* **2016,** *309*, 1-10.

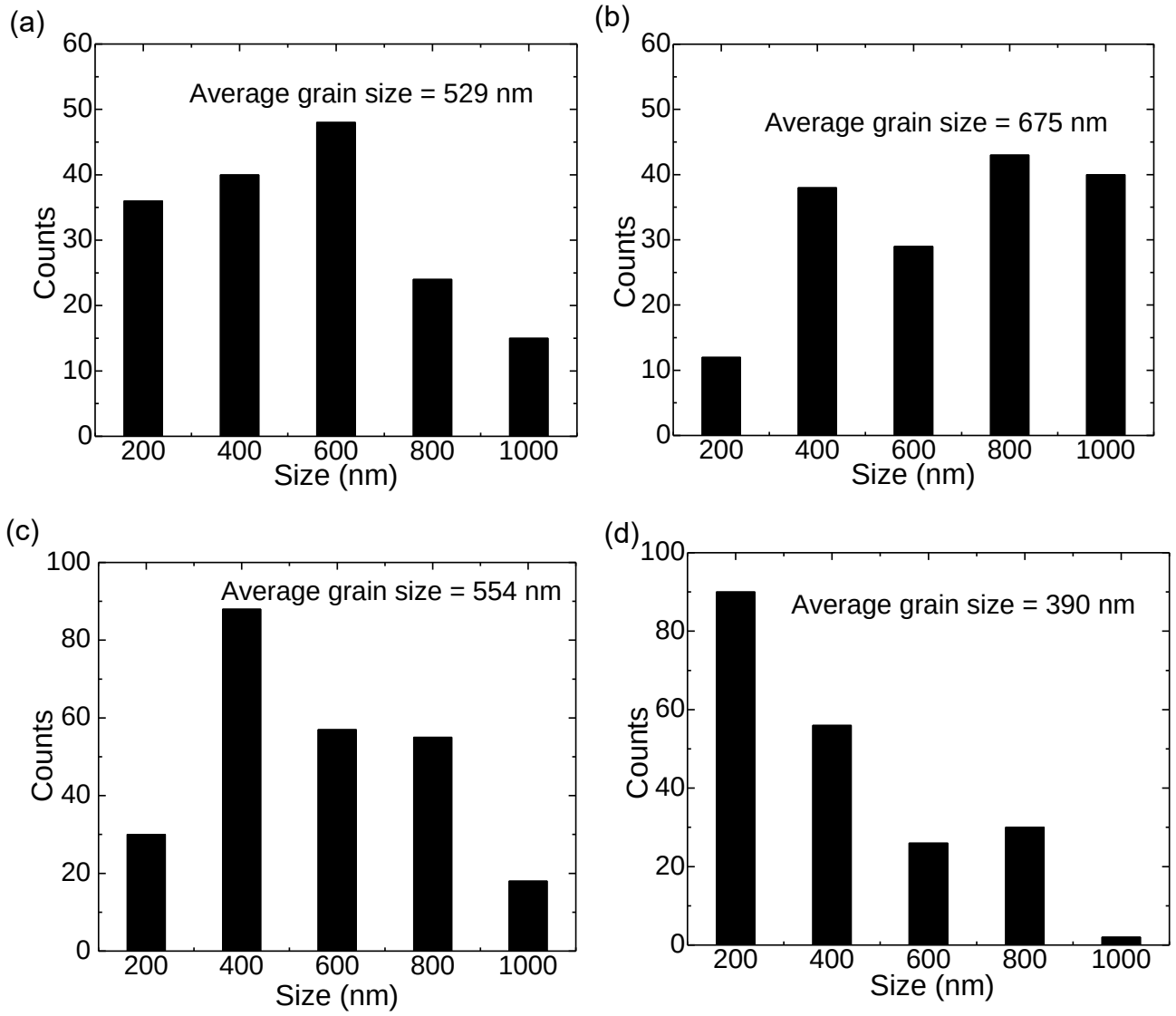

Figure S4.1. Grain size distributions determined from SEM images in figure 2a, b, c and d for perovskite films with only SnF_2, SnF_2+2.5 mol% N_2H_5Cl, SnF_2+5 mol% N_2H_5Cl and SnF_2+10 mol% N_2H_5Cl respectively.

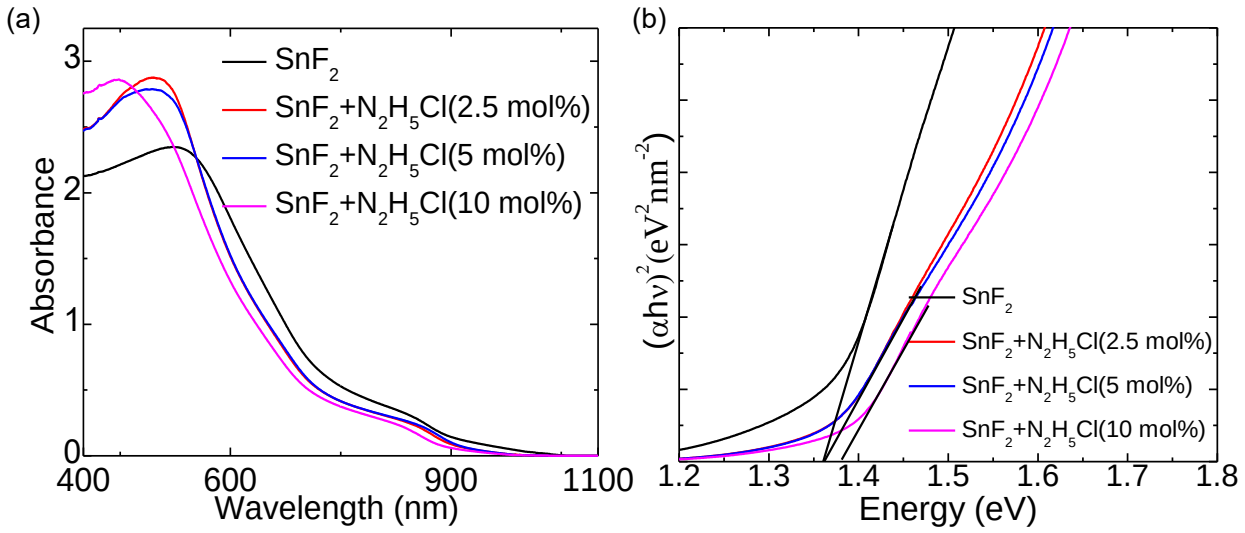

Figure S4.2. (a) UV-Vis spectra (b) Tauc plot of $FASnI_3$ films with only SnF_2 and with SnF_2 + various concentration of N_2H_5Cl.

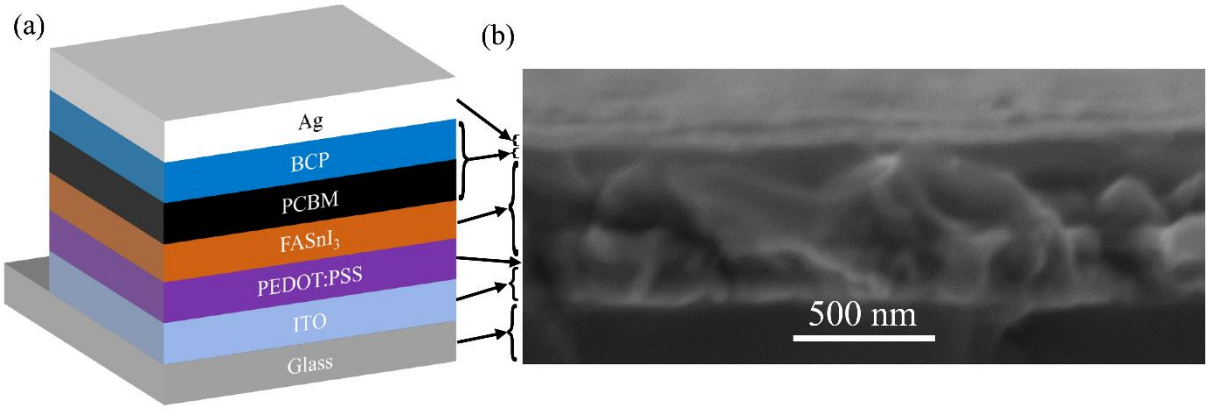

Figure S4.3. (a) Schematic illustration of the device structure, and (b) cross-sectional scanning electron microscope image of complete $FASnI_3$ based PSC.

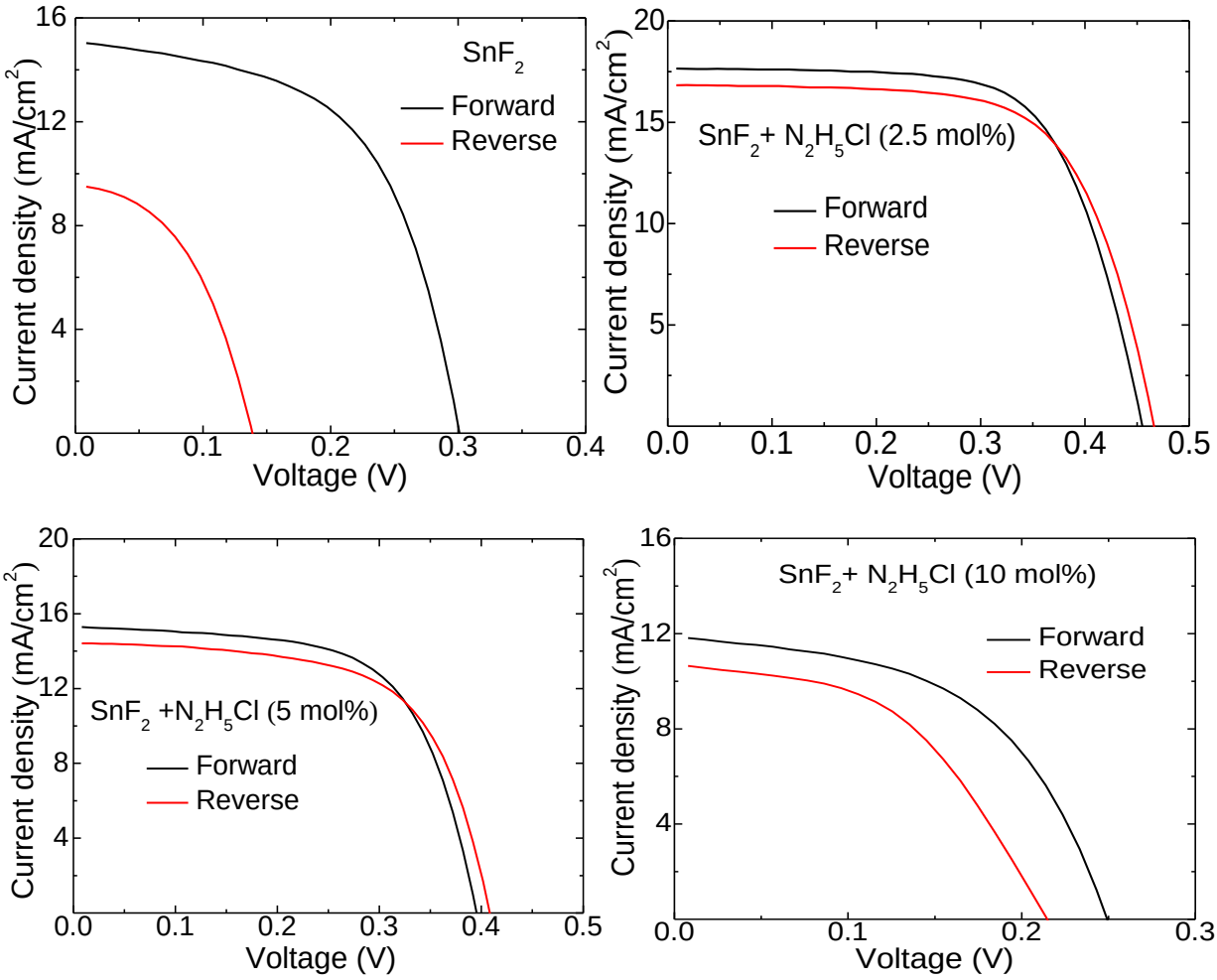

Figure S4.4. Current density-voltage (*J-V*) curves of SnF_2 and SnF_2 + various concentration of N_2H_5Cl based PSCs measured under forward and reverse voltage scan.

Table S4.1. The full width at half maxima (FWHM) of different peaks at different angles

Sample	FWHM at		
	14.1^0	24.5^0	28.4^0
$FASnI_3$ (SnF_2)	0.145	0.121	0.118
$FASnI_3$ (SnF_2 +2.5 mol% N_2H_5Cl)	0.110	0.125	0.093
$FASnI_3$ (SnF_2 +5 mol% N_2H_5Cl)	0.124	0.121	0.116
$FASnI_3$ (SnF_2 +10 mol% N_2H_5Cl)	0.196	0.163	0.174

Table S4.2. The fitting results of XPS spectra for the SnF_2 added $FASnI_3$ films.

$FASnI_3$ (10 mol% SnF_2)	Sn $3d_{5/2}$		Sn $3d_{3/2}$	
	Sn^{2+}	Sn^{4+}	Sn^{2+}	Sn^{4+}
Energy position (eV)	486.54	487.47	494.95	495.88
FWHM	1.20	1.57	1.20	1.54
% Gauss	80	80	80	80
Area	103185	57483	69134	38514
Area ratio	1	0.56	1	0.56
Atomic %	13.1	7.3	13.1	7.3

Table S4.3. The fitting results of XPS spectra for the SnF_2+ N_2H_5Cl added $FASnI_3$ films.

$FASnI_3$ (10 mol% SnF_2 + 2.5 mol% N_2H_5Cl)	Sn $3d_{5/2}$		Sn $3d_{3/2}$	
	Sn^{2+}	Sn^{4+}	Sn^{2+}	Sn^{4+}
Energy position (eV)	486.56	487.47	494.97	495.86
FWHM	1.20	1.33	1.20	1.33
% Gauss	80	80	80	80
Area	103357	35525	69249	23802
Area ratio	1	0.34	1	0.34
Atomic %	14.3	4.9	14.3	4.9

Table S4.4. Photovoltaic parameters of PSCs as a function of N_2H_5Cl concentration in the precursor solution under forward and reverse bias condition.

N_2H_5Cl concentration in mol %	Scan direction	J_{SC} (mA/cm^2)	V_{OC} (V)	FF	PCE (%)
0	Forward	15.069	0.297	0.559	2.5
	Reverse	9.54	0.139	0.458	0.61
2.5	Forward	17.63	0.455	0.673	5.40
	Reverse	16.822	0.466	0.669	5.24
5	Forward	15.317	0.395	0.632	3.83
	Reverse	14.43	0.408	0.629	3.71
10	Forward	10.53	0.351	0.497	1.84
	Reverse	8.902	0.365	0.564	1.83

Chapter 5

Coadditive Engineering with 5-Ammonium Valeric Acid Iodide for Efficient and Stable Sn Perovskite Solar Cells

5.1 Introduction

Sn-based perovskites have become promising candidates as an alternative of toxic Pb-based perovskite for the green energy technology due to their low toxicity and similar or even superior photovoltaic properties.[1-3] Even though it's favorable optoelectronic properties, the performance of Sn-based PSCs is still far below from the Pb-based devices.[4] This is because the Sn-based perovskites are suffered from some fundamental limitations such as inability to form pin-holes free uniform films, facial tendency to oxidation from Sn^{2+} to Sn^{4+} and poor stability.[5-6] The oxidation of Sn^{2+}, which is also known as the Sn^{2+} vacancies, causes unwanted p-type doping in perovskite films, result resulting in loses of suitable semiconducting properties for Sn-based perovskite materials.[7]

To lower the Sn^{4+} content in final film, Mathews et al. group used excess amount of SnF_2 into the precursor solution and demonstrated that the addition of SnF_2 is also essential for continuous film morphology with lower Sn^{4+} content.[8] After that, the addition of excess amount of SnF_2 is commonly used for Sn-based and other mixed metal-based PSCs.[9-10] Later, several other additives such as $SnCl_2$, $SnBr_2$, H_3PO_2, pyrazine, hydrazine vapor etc. have also been used with SnF_2 to further reduce the Sn^{4+} concentration and to improve the film morphology.[11-15] In this regard, the addition of N_2H_5Cl as a coadditive of SnF_2 has been found beneficial not only to reduce the Sn^{4+} content but also to deposit uniform and pin-holes free $FASnI_3$ films.[16] Mixing of organic cation have has also been reported to enhance the performance and stability of Sn-based PSCs. For instant, Huang et al. replaced part of methylamonium (MA^+) by formamidinium (FA^+) for Sn-based perovskite films and improved the performance and reproducibility.[17] However, the Sn-based PSCs are still suffered from their poor device stability. To enhance the stability, recently the two-dimensional (2D)/ three-dimensional (3D) composite perovskites concept from the Pb-based PSCs has been implemented for Sn-based PSCs.[18-19] In this case, a hydrophobic low dimensional perovskite is formed on the top of 3D perovskite by replacing small organic cation with bulkier organic cation which effectively protects the inner layer from ambient environment. For example, Ning et al. added 20 mol% phenylethylammonium iodide (PEAI) into $FASnI_3$ precursor solution to form a 2D/3D perovskite interface layer and improved the device performance and stability.[18] Later, Shao et al. group optimized the PEAI for $FASnI_3$ based PSCs and improved the PCE up to 9% and light soaking stability for 2 h in nitrogen filled glove box.[19] But they did not show the maximum power point tracking (MPPT) stability of Sn-based PSCs which is considered as the standard degradation test

for any photovoltaic solar cells. Recently, Diau et al. reported PCE of 9.6% with 1 h operational stability at MPPT condition by using two co-additives for $FASnI_3$ based PSCs in 0.022 cm^2 active area.

Hydrophobic long carbon chain organic additives with bifunctional groups, like 5-ammonium valeric acid iodide (5- AVAI) and butylphosphonic acid 4-ammonium chloride (4ABPCl), are well-known for improving the crystallinity and stability of Pb-based perovskites by cross-linking adjacent grains and forming a protective layer.[21-22] Nazeeruddin et al. used the hydrophobic nature of 5-AVAI to form an ultra-stable 2D perovskite with PbI_2 and showed 1 year-stable PSCs.[21] In contrast, Graetzel et al. demonstrated the crosslinking properties of 4-ABPCl to fabricate a compact and passive film morphology for stable Pb-based PSCs.[22] Therefore, these dual beneficial aspects of additives for cross-linking grains through hydrogen bond formation and forming an inert passive layer on the surface might simultaneously enhance the performance and stability of Sn-based PSCs, which has not been explored yet.

In this thesis, the effects of 5-AVAI on the passivation of grain boundaries, film formation and crystallinity, and the overall device performance and stability have been studied. With the addition of 5-AVAI in to the precursor solution, it has been observed that the 5-AVAI coordinated with SnI_6^{-4} through hydrogen bond formation by its bifunctional groups and effectively passivated grain boundaries of $FASnI_3$ films. We also found that a small proportion of 5-AVAI changed the crystal orientation and enhanced the crystallinity and optoelectronic properties of $FASnI_3$ films. As a result, the PCE of PSCs improved from 3.30 % to 6.85 %. More importantly, the PSC with 3 mol% 5-AVAI showed remarkable operational stability with zero loss in performance up to 100 hours.

5.2 Experimental Procedure

5.2.1 Materials

We have used all the chemicals as received without any further purification, including- SnI_2 (99.99%, Sigma–Aldrich), FAI (> 98%, Tokyo Chemical Industry Co., Japan), SnF_2 (>99%, Sigma-Aldrich), 5-Aminovaleric acid (Sigma-Aldrich), Poly(3,4-ethylenedioxythiophene)-polystyrene sulfonate (PEDOT:PSS) (Clevious P VP Al 4083), Phenyl-C61-butyric acid methyl ester (PCBM) (99.5%, Lumtec Co., Taiwan). Bathocuproine (BCP) and super dehydrated solvents of dimethyl sulfoxide (DMSO), chlorobenzene, methanol and ethanol, were purchased from Wako Co., Japan.

5.2.2 Materials Synthesis

$HOOC(CH_2)_4NH_3I$ (5-AVAI) was synthesized by reacting hydroiodic acid with 5-amiovaleric acid with a molar ratio of 1:1 under continuous stirring for 2 hours at 0^0 C. After that, the remaining liquid was evaporated using rotary evaporator. Finally, the precipitate was washed three time with diethyl ether and vacuum dried overnight.

5.2.3 Perovskite Film Fabrication

The precursor solution for $FASnI_3$ perovskite film was prepared by mixing equaimolar ratio of (0.8 mmol) SnI_2 and FAI with 10 mol% SnF_2 in 1ml of DMSO solvent. For the co-additive engineering of $FASnI_3$ films, we prepared precursor solution by adding 3 mol%, 5 mol%, 10 mol% and 100 mol% of 5-AVAI and maintained 1:1 molar ratio of 5-AVAI and $FASnI_3$ to SnI_2 in DMSO. The perovskite film was deposited by spin-coating 70µL of precursor solution at 5000 rpm for 45 s. During spin-coating, 80 µL chlorobenzene was dripped on the substrate after 17 seconds. The spin-coated films were then annealed. The annealing process was performed in two steps: at first heating at 65^0 C for 30 s and then heating at 100^0C for 15 min.

5.2.4 Solar Cell Fabrication

All the PSCs were fabricated on the patterned indium tin oxide (ITO) coated glass substrates. The substrates were ultrasonically cleaned with detergent, de-ionized water, acetone, and ethanol respectively for 15 min each. Before starting the device fabrication process, the cleaned substrates were treated with ultraviolet (UV)/ozone radiation for 30 min. The hole transport layer (HTL) was deposited on top of the ITO substrate by spin-coating 70µL of PEDOT:PSS solution at 1000 rpm and 4000 rpm for 10 s and 30 s respectively. The PEDOT:PSS films were then annealed at 150 ^{0}C for 15 min and cooled down to room temperature. After cooling at room temperature, the substrates were transferred to glove box and the $FASnI_3$ perovskite films were deposited. An electron transporting layer PCBM (20 mg ml^{-1} in chlorobenzene) and BCP (saturated solution in isopropanol) were deposited by spin-coating at 1000 rpm for 30 s and 6000 rpm for 30 s respectively. Finally, a 90 nm thick silver layer was vacuum deposited through a shadow mask with an active area of 0.25 cm^2. The PSCs were sealed, by a cavity glass using UV curable glue on top of the front active area of ITO.

5.2.5 Characterization

The absorption spectra of perovskite films were measured by a Shimadzu UV/Vis 3600 spectrophotometer. A field-emission scanning electron microscope (SEM) (JSM-6500F SEM) was used to obtain SEM images of samples, under an acceleration voltage of 5 kV. MiniFlex600 powder X-ray diffractometer was used for XRD pattern of thin films. Proton nuclear magnetic resonance (^{1}H NMR) spectra of $FASnI_3$ films were collected on JEOL ECS 400 NMR spectrometer, operating at 400 MHz. X-ray photoelectron spectroscopy (XPS) spectra were collected for perovskite films deposited on ITO glass substrate by using PHI Quantera SXM (ULVAC- PHI). An ultrahigh vacuum as high as $5x10^{-11}$ mbar was used for XPS measurement. Multi pack software was used for curve fitting. Steady state photoluminescence (PL) and time resolved PL (TRPL) were measured with a Hamamatsu C12132 fluorescence lifetime spectrometer using a 1.5 ns pulsed laser (frequency 15 kHz), at an excitation wavelength of λ=532 nm, and an excitation power of 1 mW. The samples for the PL and TRPL measurements were deposited on glass substrates and encapsulated using cavity glass and UV-curable glue.

The current density - voltage (*J-V)* curves were measured by means of a solar simulator with standard air mass 1.5 sunlight (100mWcm^{-2}, WXS-155S-10: Wacom Denso Co., Japan) under ambient conditions. The *J-V* curves were measured in forward (-0.1V to 0.7V) or reverse (0.7V to -0.1V) scans by using the Keithley 2400 as a digital source meter under ambient condition with a delay time of 10 ms. A metal mask of 0.25 cm^2 in area was used for all *J-V* curves measurements. For incident photon-to-current conversion efficiency spectra, a monochromatic incident light (1x10^{16} photons/cm^2) in direct current mode (CEP-2000BX, Bunkoukeiki Co., LTD) was used. The electrochemical impedance spectra (EIS) was performed by using electrochemical workstation (PAIOS 4, FLUXiM) in frequency range of 4Hz to 4MHz with ac amplitude 50 mV under dark condition at 0.3V. The operational (or light socking) stability test of the encapsulated solar cells was measured under maximum power point tracking condition (using VK-PA-25 PV Power Analyzer, SPD Laboratory, Inc) and under 1 sun continuous illumination (with a 420 nm UV cut filter). For operational stability the solar cells were encapsulated in nitrogen filled glovebox using cavity glass and UV-curable glue. In addition, the encapsulated solar cells were enclosed into a stainless-steel capsule equipped with electrical connectors, quartz window for illumination and inlets for gas flow (such as Ar, N_2) to minimize the exposure to air during the measurements.

5.3 Results and Discussion

One step anti-solvent method has been used for the fabrication of $FASnI_3$ films. Here, the precursor solution has been prepared by dissolving formamidinium iodide (FAI, 0.8 mmol), tin iodide (SnI_2, 0.8 mmol), tin fluoride (SnF_2, 0.1mmol) in dimethyl sulfoxide (DMSO) solvent. To observe the effect of 5-AVAI on the $FASnI_3$ films, the 5-AVAI was added into the precursor solution by maintaining a 1:1 molar ratio of organic cations and SnI_2. The optimized molar ratio of 5-AVAI to FAI was found to 1:30. To investigate the effects of 5-AVAI addition into the precursor solution, we performed morphological, structural and optical characterization. For simplicity, hereafter the perovskite film prepared by addition of only SnF_2 and SnF_2 + 5-AVAI will refer as pristine and with 5-AVAI respectively.

Proton nuclear magnetic resonance (^{1}H NMR) measurement was performed to observe the coordination of 5-AVAI with $FASnI_3$ (Figure 5.1). To do this, the ^{1}H NMR spectra of FAI, 5-AVAI, FAI-SnI_2, and FAI-5-AVAI-SnI_2 in deuterated dimethyl sulfoxide-d_6 (DMSO-d_6) solution have been performed (Figure 5.1). For FAI-SnI_2 ^{1}H NMR spectra, the proton resonance peaks at 7.8 ppm, 8.4 ppm and 8.7 ppm can be assigned for the -CH-, -NH_2 and =NH_2 for FA respectively[23]. But with the addition of 5-AVAI into FAI-SnI_2 solution, including the above three peaks, a new proton resonance peak appeared at 7.5 ppm. To assign this peak, we performed ^{1}H NMR for FAI with 5-AVAI and SnI_2 with 5-AVAI solution in DMSO-d_6. For FAI with 5-AVAI, we observed no new peak except the peaks related to the FAI and 5-AVAI. However, for SnI_2 with 5-AVAI, we found a new peak at about 7.5 ppm which was not present in the ^{1}H NMR spectra of 5-AVAI but perfectly matched with the newly appeared peaks that was developed with the addition of 5-AVAI into $FASnI_3$ precursor solution. From this result, we proposed that the 5-AVAI undergoes a hydrogen bond interaction (O−H···I and N−H···I) by the carboxylic acid (−COOH) and the ammonium (−NH^{3+}) end groups of 5- AVAI with

iodide from SnI_6^{4-} octahedra. This type of phenomena has been confirmed for Pb-based perovskite system in which a bifunctional additive such as 4-ABPCl, cross-links adjacent perovskite grains by hydrogen bonding between phosphonic acid moiety and iodine ion of PbI_6^{4-}octahedra.[22]

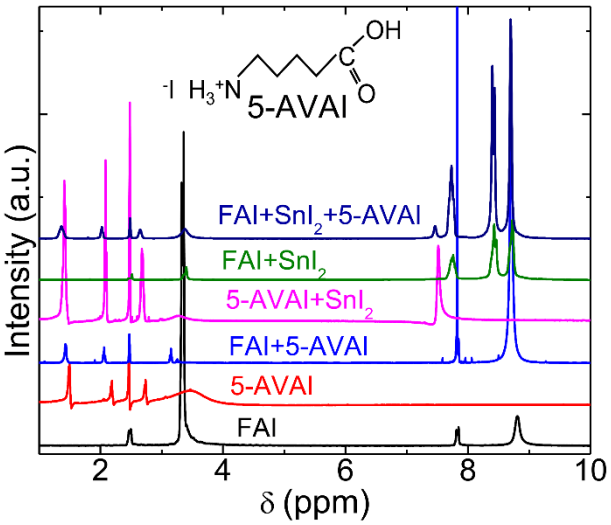

Figure 5. 1. ^{1}H NMR spectra of FAI, 5-AVAI, FAI+5-AVAI, FAI+SnI_2 and FAI+SnI_2+5-AVAI in DMSO-d_6 solution.

The surface morphology of $FASnI_3$ films was investigated by means of scanning electron microscopy (SEM) (Figure 5.2). The pristine $FASnI_3$ film exhibited relatively larger grains but very poor film coverage with numerous pinholes. The average grain size was about 603 nm (Figure S5.2a). However, after incorporating optimum amount (3 mol%) of 5-AVAI into $FASnI_3$ precursor solution, a homogeneous and pin-holes free uniform film was obtained. This is because the bifunctional 5-AVAI additive becomes coordinated with SnI_2, which delays the perovskite crystallization rate and directs the growth of perovskite grains with full coverage. However, we observed a reduced grain size of perovskite with increasing amount of 5-AVAI (average grain size 418 nm, 343 nm and 128 nm for 3 mol%, 5 mol% and 10 mol% of 5-VAI respectively (Figure S5.2b-d)), possibly due to the increasing number of heterogeneous nucleation sites with increasing 5-AVAI amount.[24-25]

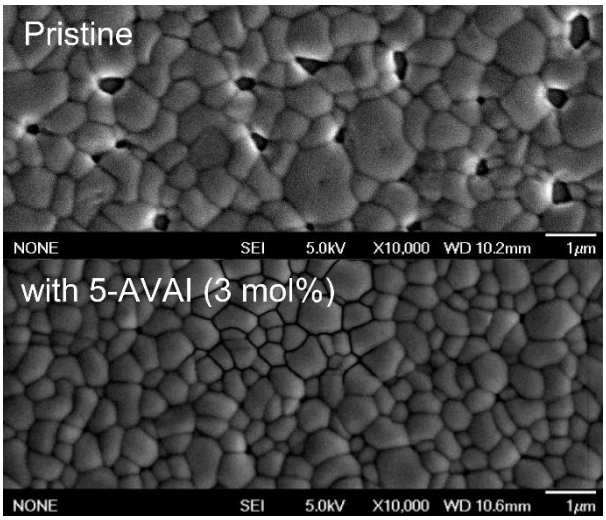

Figure 5. 2. SEM images of pristine and 5-AVAI added $FASnI_3$ films.

X-ray diffraction (XRD) patterns of pristine and with 5-AVAI $FASnI_3$ films showed similar characteristic XRD peaks located at14.1^0, 24.5°, 28.3^0, 31.8^0, 40.50^0 and 42.9^0 which can be assigned to 100, 102, 200, 122, 222 and 213 crystal planes respectively for the orthorhombic perovskite phase (Figure 5.3).[18,26] More in details, the $FASnI_3$ films with 3 mol% of 5-AVAI show a change in intensity of (100), (102) and (200) peaks as compared with pristine $FASnI_3$ XRD pattern. With the addition of 5-AVAI the diffraction intensity of (102) plane decreased whereas the intensities of (100) and (200) plans increased relatively to those of other peaks. This result indicates a preferred orientation along the <h00> direction with the addition of 5-AVAI into the precursor solution.[27] The XRD pattern of film with composition of only 5-AVAI and SnI_2 showed some sharp peaks at lower diffraction angle ($2\theta < 10^0$). This result provides the evidence for the formation of low dimensional perovskite.[28]

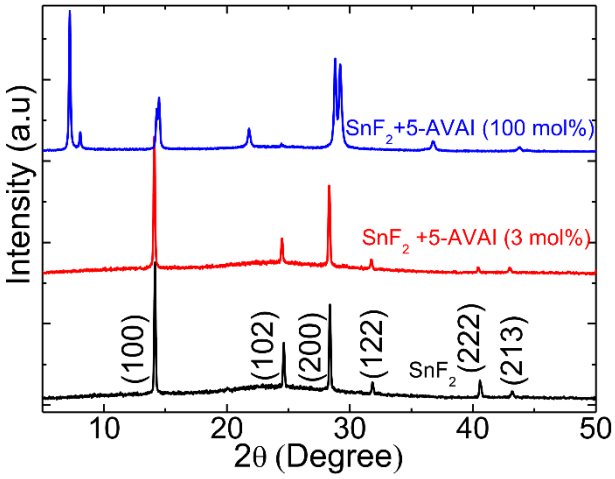

Figure 5.3. XRD patterns of $FASnI_3$ films at various concentration of 5-AVAI.

To evaluate the impact of 5-AVAI addition on the optoelectronic properties of $FASnI_3$ films, the UV-Vis absorbance, steady state photoluminescence (PL) and time resolved PL (TRPL) measurement have been performed on pristine and 5-AVAI added $FASnI_3$ films (encapsulated films on glass substrate). From the UV-vis absorbance (Figure S5.3) and steady state PL (Figure 5.4a), it was observed that the addition of 5-AVAI did not have significant effects on the absorption band edge. For semiconducting materials, carrier PL lifetime is considered as the hall mark for the quality of materials. The higher the PL lifetime better the quality of material. From TRPL measurement, a longer PL lifetime (τ) for the $FASnI_3$ with 5-AVAI (τ=5.88 nm) as compared to the pristine $FASnI_3$ film (τ=3.53 nm) (Figure 5.4.b) have been observed. This enhancement in PL lifetime (τ) with the addition of 5-AVAI indicates the reduction of charge recombination in the $FASnI_3$ film.

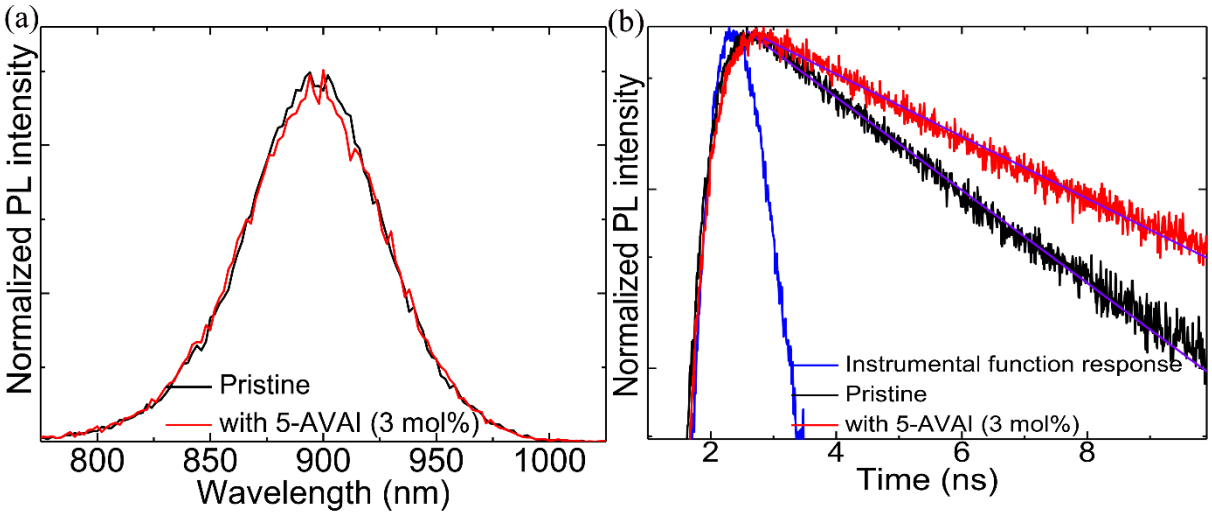

Figure 5. 4. Steady-state photoluminecence (PL) (a) and time resolved PL (TRPL) (b) of pristine and 5-AVAI added $FASnI_3$ films.

To observe the existence of 5-AVAI on the surface of $FASnI_3$ film, the X-ray photoelectron spectroscopy (XPS) measurement for pristine and 5-AVAI added $FASnI_3$ films has been performed (Figure S5.4). As the 5-AVAI additive contains carbon, nitrogen and oxygen elements, so to observe the existence of 5-AVAI on the surface of the $FASnI_3$ films, the XPS peaks of C1s, N1s and O1s for pristine and 5-AVAI added $FASnI_3$ films have been compared (Figure 5.5a-c). From elemental analysis, a new shoulder peak for C1s at 286.0 eV (Figure 5.5a) and an overall increased amount of C concentration for $FASnI_3$ film with 5-AVAI (see Table ST5.1) has been observed. For N1s, the peak at 401.5 eV (Figure 5.5b) can be assigned for NH_4^+ group and for O1s, a dominated peak at 531.9 eV (Figure 5.5c) can be assigned for C-OH or C-O-C or COO^- functional group. Therefore, the above elemental analysis, demonstrates the presence of NH_4^+, COO^- and an increased amount of carbon on the surface for 5-AVAI added $FASnI_3$ film which ultimately indicates the existence of 5-AVAI on surface of perovskite film. In this measurement, a reduced atomic percentage of Sn^{4+} was observed for 5-AVAI added $FASnI_3$ film as compared with the pristine $FASnI_3$ film (Figure 5.5d-e) which reveals the Sn^{2+} oxidation retardation ability of 5-AVAI. Most importantly, the atomic ratio of Sn:I was found

1:1.2 for both pristine and 5-AVAI added $FASnI_3$ films (Table ST5.2). But from the chemical composition it should be 1:3 as it is found for $MAPbI_3$ system.[29] This may be due to the higher content of SnF_2 on the perovskite surface as XPS can detect only the elements situated up to a 5−6 nm depth from the surface.

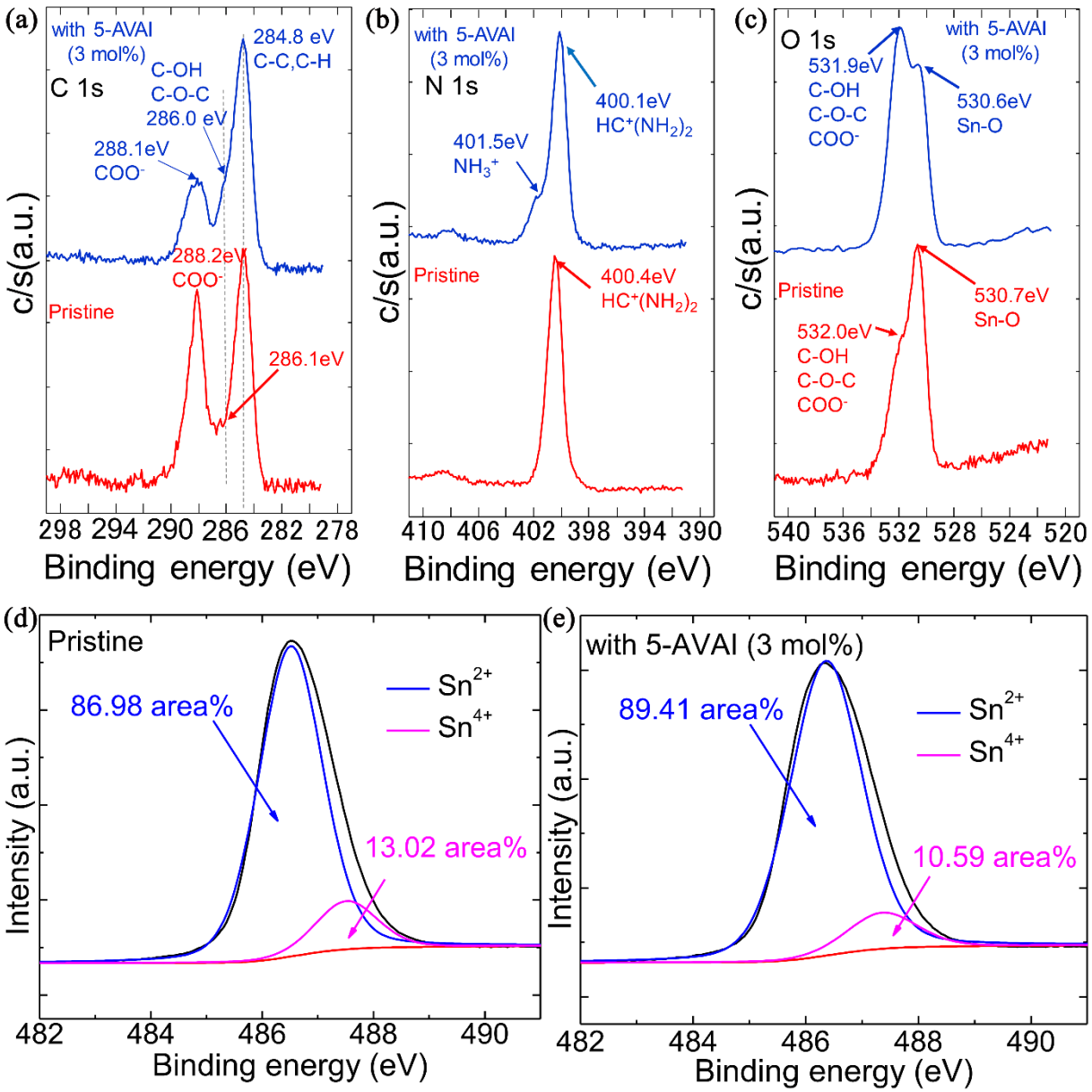

Figure 5.5. XPS spectra for C1s (a), N1s (b) and O1s (c) on the surface of pristine and 5-AVAI added $FASnI_3$ films; XPS spectra for pristine (d) and 5-AVAI added (e) $FASnI_3$ films showing Sn^{2+} and Sn^{4+} distribution in their surface state.

Photovoltaic Performance

As the $FASnI_3$ films with 5-AVAI are highly crystalline pin-holes free and featuring longer PL lifetime, it can be expected that $FASnI_3$ based solar cells with 5-AVAI will have better device performances.

To study the effect of 5-AVAI on the device performance, the ITO/PEDOT:PSS/$FASnI_3$/PCBM/BCP/Ag inverted planar heterojunction solar cells were fabricated. The current density-voltage (J-V) curves of the best $FASnI_3$ solar cells either pristine or with 5-AVAI under 1 sun in forward bias scan (from -0.1 V to 0.7 V) are shown in Figure 5.6a, and the corresponding photovoltaic performance parameters are summarized in Table 5.1. The PCE of the pristine $FASnI_3$ solar cell is 3.40 % with short circuit current (J_{SC}) = 15.75 mA/cm^2, open circuit voltage (V_{OC}) = 0.36 V and fill factor (FF) =0.59, which are consistent with the previously reported results.[16] On the other hand, of the best solar cell consisting of $FASnI_3$ with 5-AVAI (3 mol%) shows a superior J_{SC} of 18.89 mA/cm^2, V_{OC} of 0.59 and FF of 0.62 which pushes the PCE to 7.0%.

The incident photon-to-electron conversion efficiency (IPCE) spectra for both pristine and 5-AVAI added $FASnI_3$ solar cells are shown in Figure 5.6b. The pristine PSC shows an IPCE of 25% at 800 nm and maximum 56% at 670 nm, whereas the PSC with 5-AVAI shows an enhanced IPCE with 42% at 800 nm and maximum 68% at 670 nm. The addition of 5-AVAI into $FASnI_3$ leads to an overall increase the IPCE in the entire spectral range, which is consistent with the increase of J_{SC} estimated from the J-V curves.

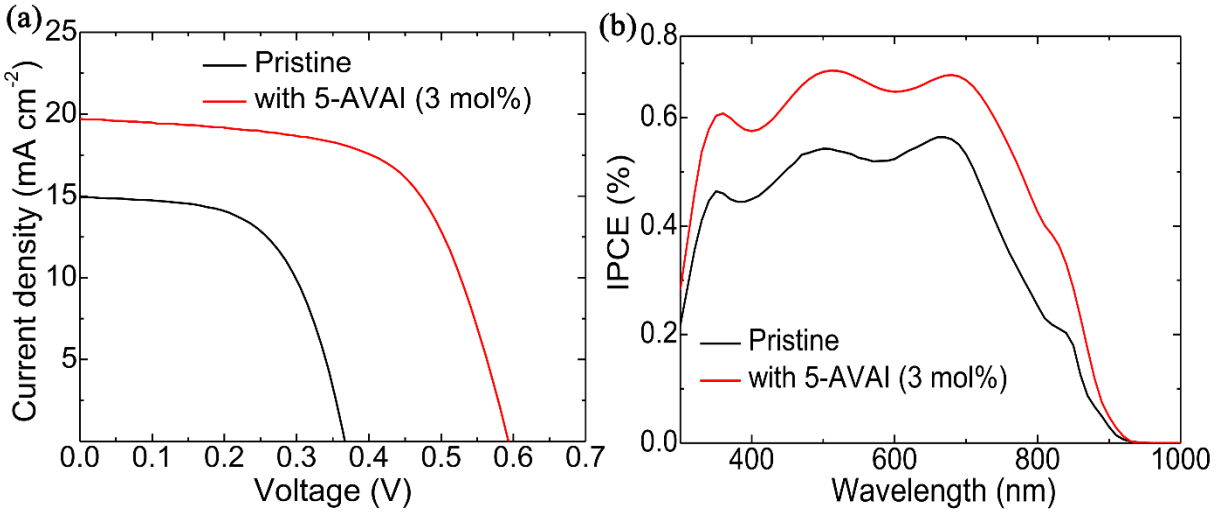

Figure 5.6. J-*V* curves measured (a) under 1 sun (A.M. 1.5, 100 mW cm^{-2}) and Incident photon-to-electron conversion efficiency (IPCE) (b) of pristine and 5-AVAI added $FASnI_3$ based PSCs.

Table 5.1. Photovoltaic performance parameters of pristine and 5-AVAI added $FASnI_3$ PSCs.

5-AVAI concentration (mol%)	Comments of the PSCs	J_{SC} (mAcm^{-2})	V_{OC}(V)	FF	PCE (%)
0	Average	15.643 ± 0.840	0.341 ± 0.019	0.564 ± 0.018	3.0 ± 0.259
	Champion	15.747	0.363	0.591	3.4
3	Average	17.99 ± 1.60	0.504 ± 0.046	0.643 ± 0.029	5.8 ± 0.664
	Champion	18.89	0.592	0.623	7.0

It important to stress that the addition of 5-AVAI into $FASnI_3$ significantly improves the V_{OC} from 0.36 V to 0.59 V as well as the J_{SC} from 15.75 mA/cm^2 to 18.89 mA/cm^2. To find out the reason for the V_{OC} enhancement, the dark *J-V* curves of the pristine and 5-AVAI added PSCs were measured (Figure 5.7a). From this measurement, it was observed that the dark current density for PSC with 5-AVAI was about 1 order of lower magnitude than the pristine one. This result indicates that the addition of 5-AVAI suppresses the leakage current, which is one of the harmful carrier recombination path that compete with dissociation and transport of the photo-generated charges. This result is also consistent with the XPS measurements showing that the concentration of Sn^{4+}, considered as one of the recombination center, was reduced upon the addition of 5-AVAI into $FASnI_3$ (Figure 5.5d-e). This result is also consistent with the longer PL lifetime (τ), which indicates the reduction of charge recombination in the $FASnI_3$ film upon the addition of 5-AVAI. To observe the effect of 5-AVAI on the charge recombination resistance, the electrochemical impedance measurement was performed on pristine and 5-AVAI added PSCs (Figure S5.5). From the Nyquist plots, a larger semicircle, which represents recombination resistance, for the 5-AVAI added device compared to that of pristine, which is consistent with the corresponding device performance (Figure 5.6). To confirm the reproducibility of results, 12 individuals PSCs were fabricated for pristine and for 5-AVAI added $FASnI_3$ (Figure 5.7b and Figure S5.6).

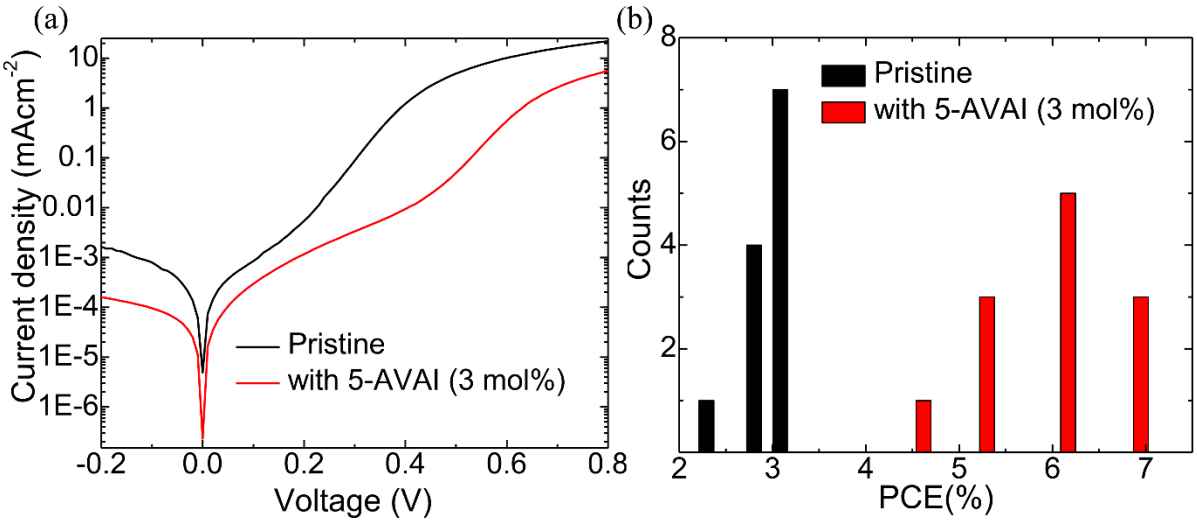

Figure 5.7. *J-V* curves measured in dark (a) and a histogram of PCE of 12 devices (b) of pristine and 5-AVAI added $FASnI_3$ based PSCs.

Device and Materials Stability

To observe the effect of 5-AVAI on the stability, the change of PCE for pristine and 5-AVAI added $FASnI_3$ based PSCs without capsulation in ambient air conditions at ~50% relative humidity have been measured (Figure 5.8a). The PCE of pristine PSC rapidly decays in ambient environment and eventually

degrade after 10 hours, whereas the PSC with 5-AVAI retains 40 % of its initial efficiency up to 50 hours. This result shows the relative ability of 5-AVAI to slowdown the degradation of PSCs even under extreme environment conditions. Next, the operational stability test on pristine and 5-AVAI added $FASnI_3$ based PSCs in encapsulated condition, under air mass 1.5 global (1.5G) continuous illumination and using the MPPT were performed (Figure 5.8b). The PCE, in the MPPT mode, of pristine PSC continuously decays and reaches 75% of its initial efficiency within 100 h, whereas the PCE of the device with 5-AVAI remarkably maintains its initial efficiency during same period. These results demonstrate that encapsulated PSCs with 5-AVAI show a better operational (light soaking) stability than pristine PSCs.

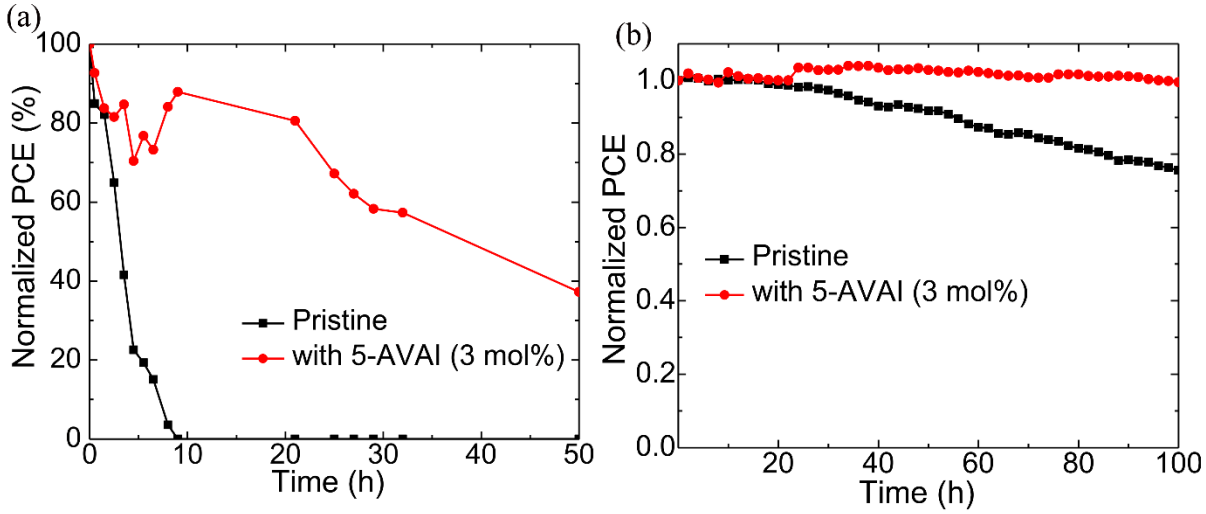

Figure 5.8. Normalized PCE of pristine and with 5-AVAI added PSCs versus time for: un-encapsulated devices in ambient air (a) and an encapsulated device under 1 sun continuous illumination in MPPT mode to test the operational stability (b).

To further confirm that 5-AVAI improves the stability of the crystal structure of $FASnI_3$ films, the XRD measurements on $FASnI_3$ films with or without 5-AVAI were performed as a function of time. Their degradation was observed by monitoring the change of XRD peaks at different interval of exposure time to ambient air ~50% relative humidity (without encapsulation, in room light condition) (Figure 5.9a and 5.9b). The pristine $FASnI_3$ film started to degrade within 3 hours exposure in air, as 3 new peaks appear at slightly higher angles adjacent to the (100), (102), (200) planes and the other one at 12.5^0. The peaks adjacent to the (100), (102), (200) planes can be assigned for different oxidation state of Sn^{2+}.[35] The peak at 12.5^0 which does not match with Sn-I or Sn-O compounds, can be assigned for (101) plane of the yellow $FASnI_3$ phase.[3, 31-32] On the other hand, XRD pattern of 5-AVAI added $FASnI_3$ film did not show any changes with time up to 15 h and some new XRD peaks corresponding to the yellow phase of $FASnI_3$ and oxidation of Sn^{2+} appeared after 26 h. Therefore, this result indicates that the addition of 5-AVAI significantly slows down the degradation and improves the environmental stability $FASnI_3$ film.

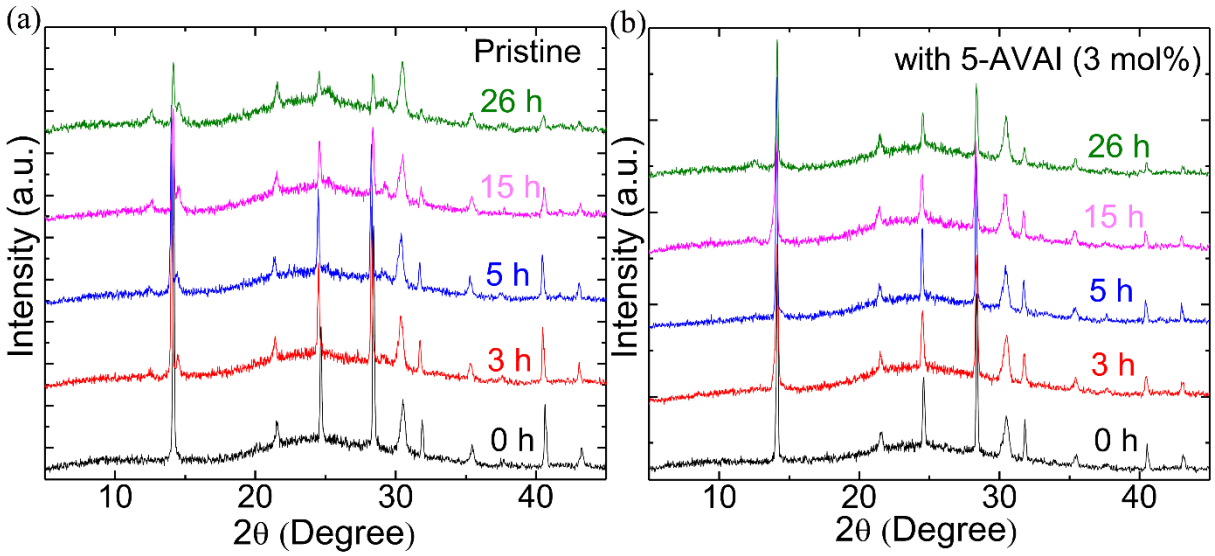

Figure 5.9. XRD pattern as a function of time of pristine and 5-AVAI added $FASnI_3$ films in ambient air (un-encapsulated).

From the detail characterization, it has been proposed that robust nature of $FASnI_3$ with the addition of 5-AVAI into the $FASnI_3$ precursor solution is due to the formation of thin hydrophobic film on the surface of perovskite film. This layer protects the $FASnI_3$ film from moisture and air. The Figure 5.10 schematically represent the stability enhancement mechanism of $FASnI_3$ by 5-AVAI.

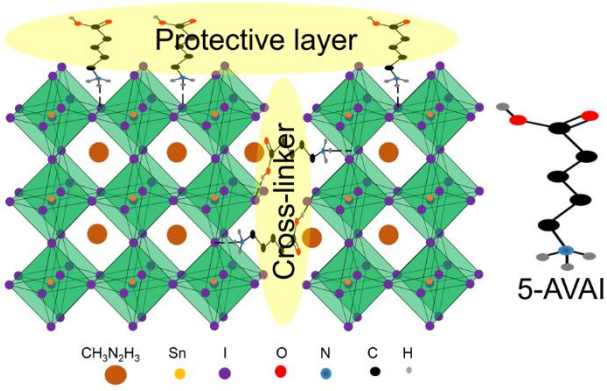

Figure 5.10. Schematically representation of proposed mechanism for the stability enhancement of $FASnI_3$ film by 5-AVAI.

5.4 Summary

In this work, it has been demonstrated that the incorporation of bifunctional 5-AVAI organic cation, effectively modifies the perovskite grains through the formation of hydrogen bonding and enhanced crystallinity of $FASnI_3$. The suppression of Sn^{2+} oxidation and enhancement of charge carrier lifetime with the

addition of 5-AVAI augmented the PCE of $FASnI_3$ based PSCs from 3.34% to 7.0%. Moreover, the existence of bulker 5-AVAI molecules at the grain boundaries of perovskite films and the formation of compact pinholes-free films, effectively retarded oxygen penetration into the perovskite lattice and enhanced the air stability of $FASnI_3$. These positive aspects of 5-AVAI made it possible to demonstrate stable $FASnI_3$ based PSCs up to 100 hours at MPPT condition. This work highlights the coadditive strategy with 5-AVAI for highly stable Sn-based PSCs, which may bring nontoxic PSCs one step closer to real-life application.

References

(1) Chung, I.; Song, J.-H.; Im, J.; Androulakis, J.; Malliakas, C. D.; Li, H.; Freeman, A. J.; Kenney, J. T.; Kanatzidis, M. G. $CsSnI_3$: Semiconductor or Metal? High Electrical Conductivity and Strong Near-Infrared Photoluminescence from a Single Material. High Hole Mobility and Phase-Transitions. *J. Am. Chem. Soc.*, **2012,** *134*, 8579-8587.

(2) Zhang, J.; Yu, C.; Wang, L.; Li, Y.; Ren, Y.; Shum, K. Energy Barrier at the N719-dye/$CsSnI_3$ Interface for Photogenerated Holes in Dye-Sensitized Solar Cells. *Sci. Rep.*, **2014,** *4*, 6954.

(3) Stoumpos, C. C.; Malliakas, C. D.; Kanatzidis, M. G. Semiconducting Tin and Lead Iodide Perovskites with Organic Cations: Phase Transitions, High Mobilities, and Near-Infrared Photoluminescent Properties. *Inorg. Chem.*, **2013,** *52*, 9019-9038.

(4) Jokar, E.; Chien, C.-H.; Chang, Y.-H.; Fathi, A.; Rameez, M.; Diau, E. W.-G. Slow Surface Passivation and Crystal Relaxation with Additives to Improve Device Performance and Durability for Tin-Based Perovskite Solar Cells. *Energy Environ. Sci.*, **2018,** *11*, 2353-2362.

(5) Noel, N. K.; Stranks, S. D.; Abate, A.; Wehrenfennig, C.; Guarnera, S.; Haghighirad, A.-A.; Sadhanala, A.; Eperon, G. E.; Pathak, S. K.; Johnston, M. B. Lead-Free Organic–Inorganic Tin Halide Perovskites for Photovoltaic Applications. *Energy Environ. Sci.*, **2014,** *7*, 3061-3068.

(6) Rajendra Kumar, G.; Kim, H.-J.; Karupannan, S.; Prabakar, K. Interplay between Iodide and Tin Vacancies in $CsSnI_3$ Perovskite Solar Cells. *J. Phys. Chem. C*, **2017,** *121*, 16447-16453.

(7) Hao, F.; Stoumpos, C. C.; Cao, D. H.; Chang, R. P.; Kanatzidis, M. G. Lead-Free Solid-State Organic–Inorganic Halide Perovskite Solar Cells. *Nat. Photonics*, **2014,** *8*, 489.

(8) Kumar, M. H.; Dharani, S.; Leong, W. L.; Boix, P. P.; Prabhakar, R. R.; Baikie, T.; Shi, C.; Ding, H.; Ramesh, R.; Asta, M. Lead-Free Halide Perovskite Solar Cells with High Photocurrents Realized Through Vacancy Modulation. *Adv. Mater.*, **2014,** *26*, 7122-7127.

(9) Liao, W.; Zhao, D.; Yu, Y.; Grice, C. R.; Wang, C.; Cimaroli, A. J.; Schulz, P.; Meng, W.; Zhu, K.; Xiong, R. G. Lead-Free Inverted Planar Formamidinium Tin Triiodide Perovskite Solar Cells Achieving Power Conversion Efficiencies up to 6.22%. *Adv. Mater.*, **2016,** *28*, 9333-9340.

(10) Ito, N.; Kamarudin, M. A.; Hirotani, D.; Zhang, Y.; Shen, Q.; Ogomi, Y.; Iikubo, S.; Minemoto, T.; Yoshino, K.; Hayase, S. Mixed Sn–Ge Perovskite for Enhanced Perovskite Solar Cell Performance in Air. *J. Phys. Chem. Lett.*, **2018,** *9*, 1682-1688.

(11) Tsai, C. M.; Mohanta, N.; Wang, C. Y.; Lin, Y. P.; Yang, Y. W.; Wang, C. L.; Hung, C. H.; Diau, E. W. G. Formation of Stable Tin Perovskites Co-crystallized with Three Halides for Carbon-Based Mesoscopic Lead-Free Perovskite Solar Cells. *Angew. Chem.*, **2017,** *129*, 14007-14011.

(12) Li, W.; Li, J.; Li, J.; Fan, J.; Mai, Y.; Wang, L. Addictive-Assisted Construction of All-Inorganic $CsSnIBr_2$ Mesoscopic Perovskite Solar Cells with Superior Thermal Stability Up to 473 K. *J. Mater. Chem. A*, **2016,** *4*, 17104-17110.

(13) Lee, S. J.; Shin, S. S.; Kim, Y. C.; Kim, D.; Ahn, T. K.; Noh, J. H.; Seo, J.; Seok, S. I. Fabrication of Efficient Formamidinium Tin Iodide Perovskite Solar Cells through SnF_2–Pyrazine Complex. *J. Am. Chem. Soc.*, **2016,** *138*, 3974-3977.

(14) Song, T.-B.; Yokoyama, T.; Stoumpos, C. C.; Logsdon, J.; Cao, D. H.; Wasielewski, M. R.; Aramaki, S.; Kanatzidis, M. G. Importance of Reducing Vapor Atmosphere in the Fabrication of Tin-Based Perovskite Solar Cells. *J. Am. Chem. Soc.,* **2017,** *139*, 836-842.

(15) Lee, S. J.; Shin, S. S.; Im, J.; Ahn, T. K.; Noh, J. H.; Jeon, N. J.; Seok, S. I.; Seo, J. Reducing Carrier Density in Formamidinium Tin Perovskites and Its Beneficial Effects on Stability and Efficiency of Perovskite Solar Cells. *ACS Energy Lett.,* **2017,** *3*, 46-53.

(16) Kayesh, M. E.; Chowdhury, T. H.; Matsuishi, K.; Kaneko, R.; Kazaoui, S.; Lee, J.-J.; Noda, T.; Islam, A. Enhanced Photovoltaic Performance of $FASnI_3$ Based Perovskite Solar Cells with Hydrazinium Chloride (N_2H_5Cl) Co-Additive. *ACS Energy Lett.,* **2018,** *3*, 1584-1589.

(17) Zhao, Z.; Gu, F.; Li, Y.; Sun, W.; Ye, S.; Rao, H.; Liu, Z.; Bian, Z.; Huang, C. Mixed-Organic-Cation Tin Iodide for Lead-Free Perovskite Solar Cells with an Efficiency of 8.12%. *Adv. Sci.,* **2017,** *4*, 1700204.

(18) Liao, Y.; Liu, H.; Zhou, W.; Yang, D.; Shang, Y.; Shi, Z.; Li, B.; Jiang, X.; Zhang, L.; Quan, L. N. Highly Oriented Low-Dimensional Tin Halide Perovskites with Enhanced Stability and Photovoltaic Performance. *J. Am. Chem. Soc.,* **2017,** *139*, 6693-6699.

(19) Shao, S.; Liu, J.; Portale, G.; Fang, H. H.; Blake, G. R.; ten Brink, G. H.; Koster, L. J. A.; Loi, M. A. Highly Reproducible Sn-Based Hybrid Perovskite Solar Cells with 9% Efficiency. *Adv. Energy Mater.,* **2018,** *8*, 1702019.

(20) Jokar, E.; Chien, C. H.; Tsai, C. M.; Fathi, A.; Diau, E. W. G. Robust Tin-Based Perovskite Solar Cells with Hybrid Organic Cations to Attain Efficiency Approaching 10%. *Adv. Mater.,* **2018**, 31, 1804835.

(21) Grancini, G.; Roldán-Carmona, C.; Zimmermann, I.; Mosconi, E.; Lee, X.; Martineau, D.; Narbey, S.; Oswald, F.; De Angelis, F.; Graetzel, M. One-Year Stable Perovskite Solar Cells by 2D/3D Interface Engineering. *Nat. Commun.* **2017,** *8*, 15684.

(22) Li, X.; Dar, M. I.; Yi, C.; Luo, J.; Tschumi, M.; Zakeeruddin, S. M.; Nazeeruddin, M. K.; Han, H.; Grätzel, M. Improved Performance and Stability of Perovskite Solar Cells by Crystal Crosslinking with Alkylphosphonic Acid ω-Ammonium Chlorides. *Nat. Chem.,* **2015,** *7*, 703-711.

(23) Ke, W.; Stoumpos, C. C.; Zhu, M.; Mao, L.; Spanopoulos, I.; Liu, J.; Kontsevoi, O. Y.; Chen, M.; Sarma, D.; Zhang, Y. Enhanced Photovoltaic Performance and Stability with a New Type of Hollow 3D Perovskite {en} $FASnI_3$. *Sci. Adv.,* **2017,** *3*, e1701293.

(22) Zhao, T.; Chueh, C.-C.; Chen, Q.; Rajagopal, A.; Jen, A. K.-Y. Defect Passivation of Organic–Inorganic Hybrid Perovskites by Diammonium Iodide Toward High-Performance Photovoltaic Devices. *ACS Energy Lett.,* **2016,** *1*, 757-763.

(25) Lee, D. S.; Yun, J. S.; Kim, J.; Soufiani, A. M.; Chen, S.; Cho, Y.; Deng, X.; Seidel, J.; Lim, S.; Huang, S. Passivation of Grain Boundaries by Phenethylammonium in Formamidinium-Methylammonium Lead Halide Perovskite Solar Cells. *ACS Energy Lett.,* **2018,** *3*, 647-654.

(26) Koh, T. M.; Krishnamoorthy, T.; Yantara, N.; Shi, C.; Leong, W. L.; Boix, P. P.; Grimsdale, A. C.; Mhaisalkar, S. G.; Mathews, N. Formamidinium Tin-Based Perovskite with Low E_g for Photovoltaic Applications. *J. Mater. Chem. A.,* **2015,** *3*, 14996-15000.

(27) Mei, A.; Li, X.; Liu, L.; Ku, Z.; Liu, T.; Rong, Y.; Xu, M.; Hu, M.; Chen, J.; Yang, Y. A Hole-Conductor–Free, Fully Printable Mesoscopic Perovskite Solar Cell with High Stability. *Science,* **2014,** *345,* 295-298.
(28) Mercier, N.; Poiroux, S.; Riou, A.; Batail, P. Unique Hydrogen Bonding Correlating with a Reduced Band Gap and Phase Transition in the Hybrid Perovskites $(HO(CH_2)_2NH_3)_2PbX_4$ (X= I, Br). *Inorg. Chem.,* **2004,** *43,* 8361-8366.
(29) Li, Y.; Xu, X.; Wang, C.; Ecker, B.; Yang, J.; Huang, J.; Gao, Y. Light-Induced Degradation of $CH_3NH_3PbI_3$ Hybrid Perovskite Thin Film. *J. Phys. Chem. C,* **2017,** *121,* 3904-3910.
(30) Wang, F.; Ma, J.; Xie, F.; Li, L.; Chen, J.; Fan, J.; Zhao, N. Organic Cation-Dependent Degradation Mechanism of Organotin Halide Perovskites. *Adv. Funct. Mater.,* **2016,** *26,* 3417-3423.
(31) Dwivedi, V.; Prakash, G. V. Fabrication and Room-Temperature Exciton Photoluminescence Stability Studies of Inorganic–Organic Hybrid $(C_{12}H_{25}NH_3)_2SnI_4$ Thin Films. *Solid State Sci.,* **2014,** *27,* 60-64.
(32) Koh, T. M.; Fu, K.; Fang, Y.; Chen, S.; Sum, T.; Mathews, N.; Mhaisalkar, S. G.; Boix, P. P.; Baikie, T. Formamidinium-Containing Metal-Halide: an Alternative Material for Near-IR Absorption Perovskite Solar Cells. *J. Phys. Chem. C,* **2013,** *118,* 16458-16462.

Supporting Information

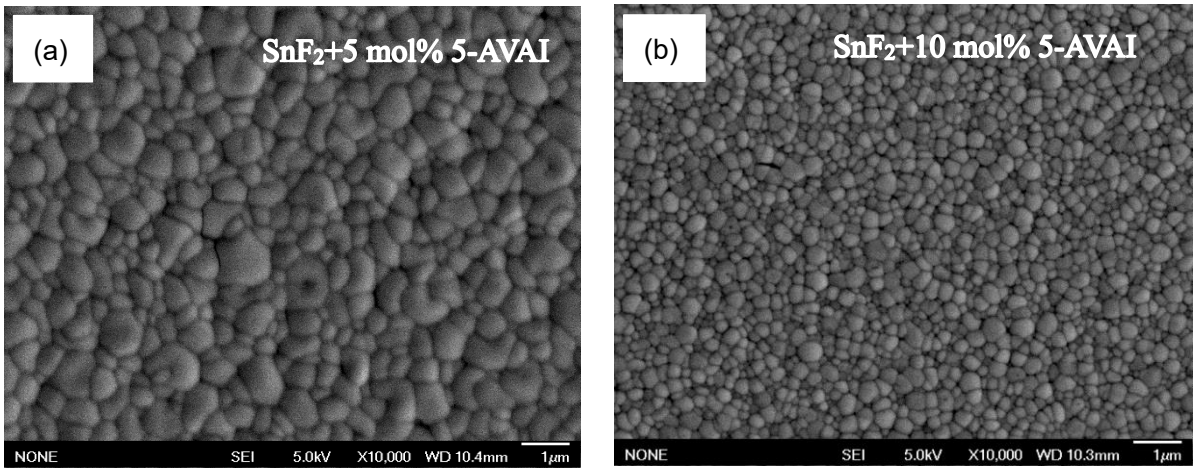

Figure S5.1. SEM images of $FASnI_3$ with the addition of (a) 5 mol% and (b) 10 mol% of 5-AVAI.

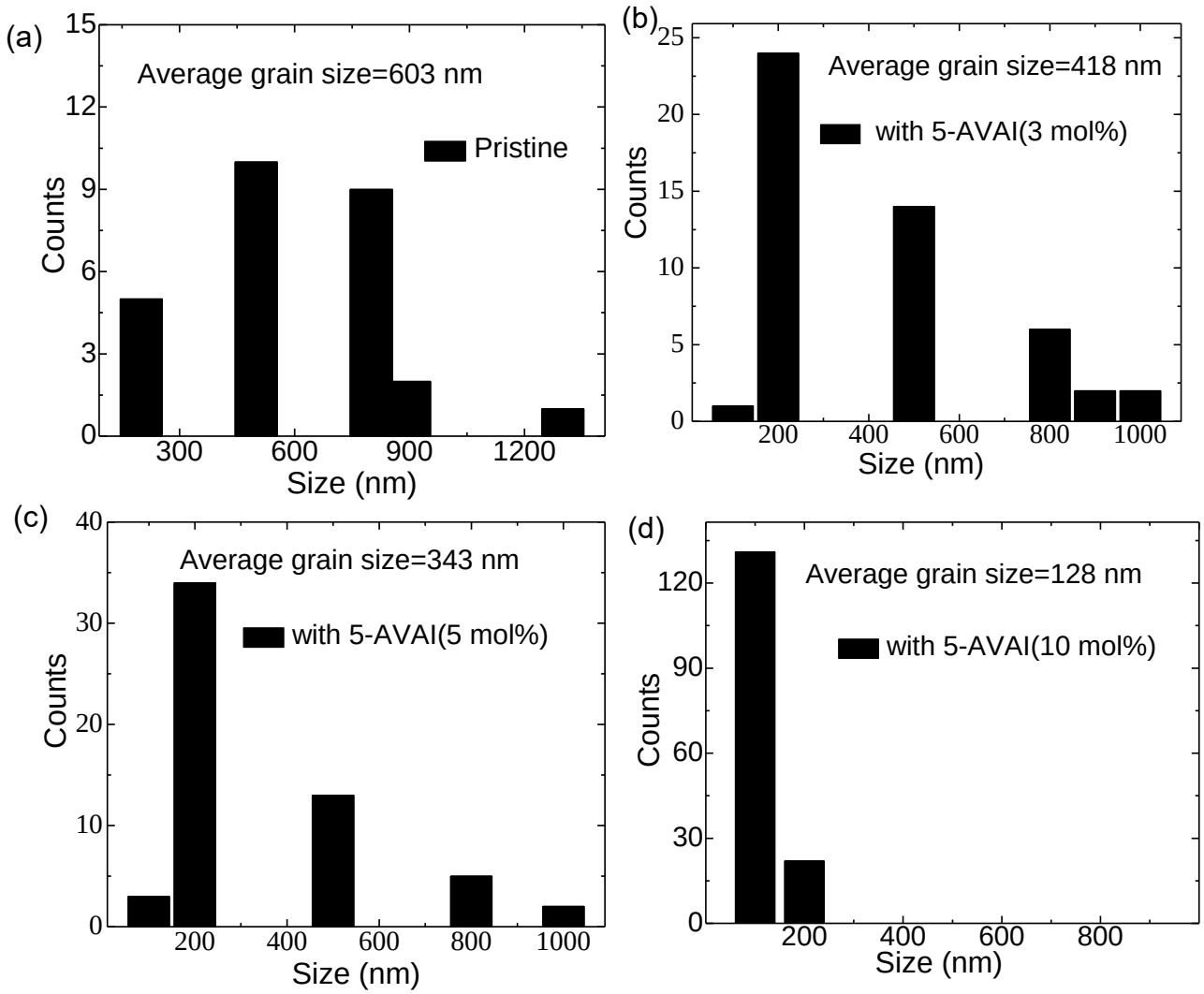

Figure S5.2. Grain size distributions determined from SEM images in Figure 1b, S1a and S1b for $FASnI_3$ with (a) 0 mol%, (b) 3 mol%, (c) 5 mol% and (d) 10 mol% of 5-AVAI respectively.

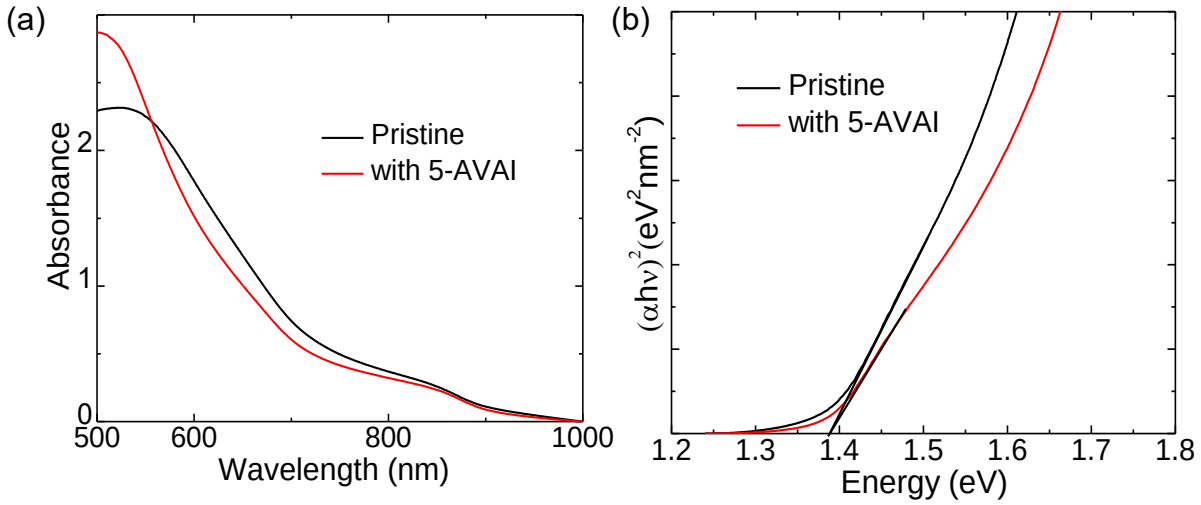

Figure S5.3. UV-Vis spectra (a) and Tauc plot (b) of pristine and 5-AVAI added $FASnI_3$ films.

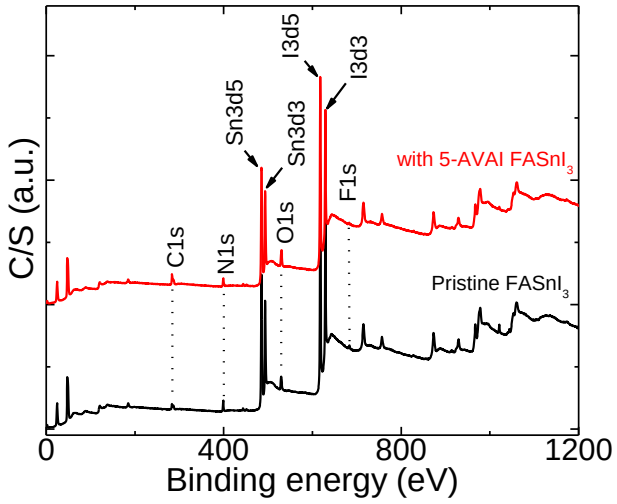

Figure S5.4. XPS survey spectra of pristine and 5-AVAI added $FASnI_3$ films.

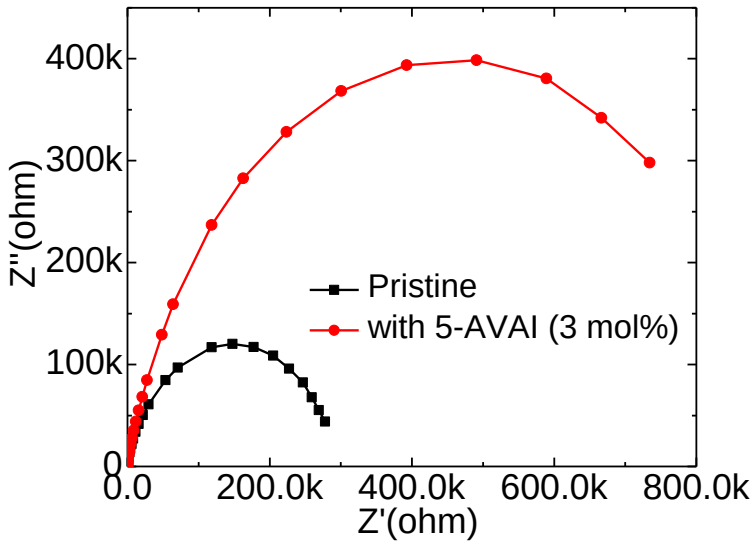

Figure S5.5. Nyquist plots of pristine and 5-AVAI added $FASnI_3$ based PSCs.

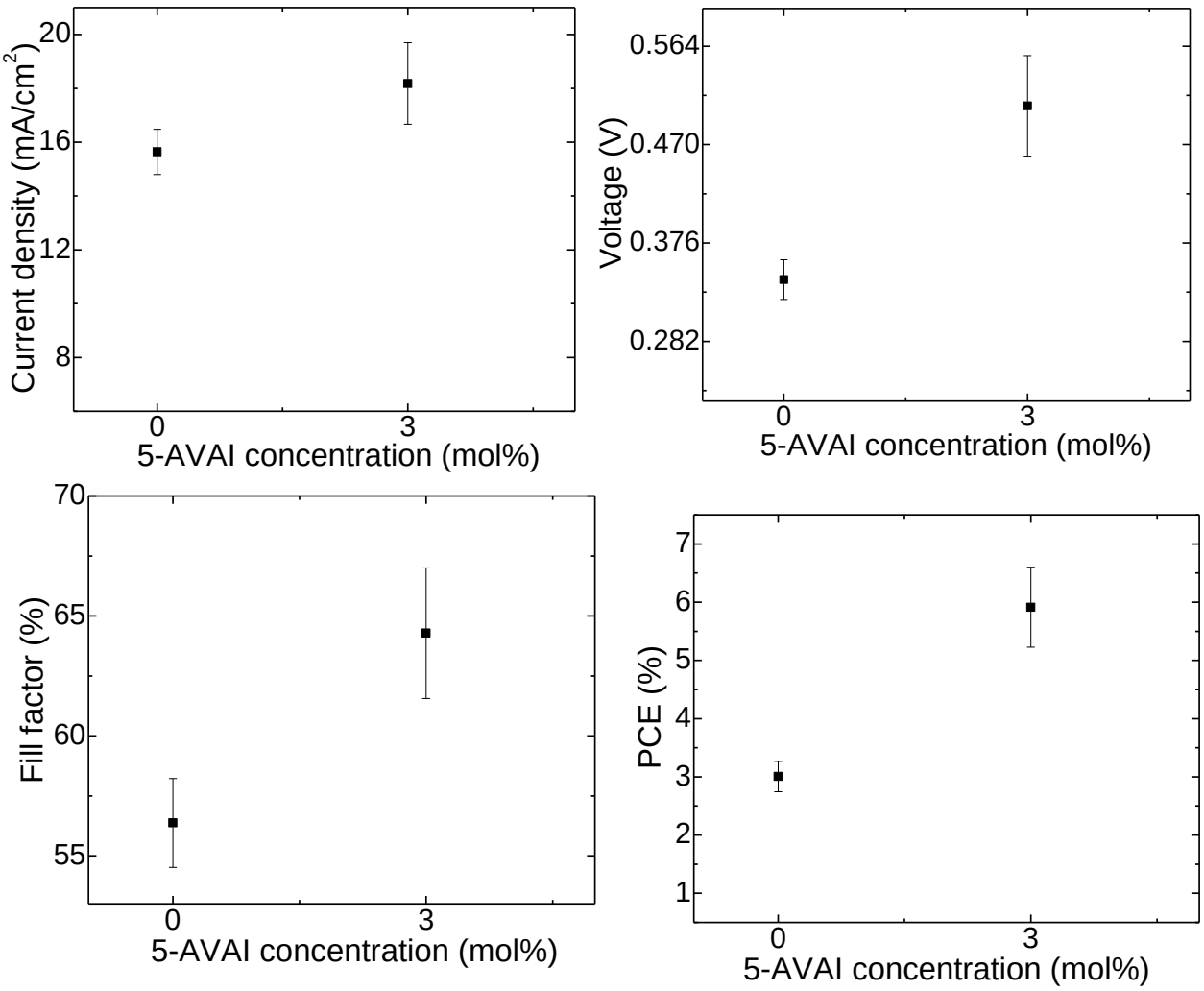

Figure S5.6. Performance parameter of pristine and 5-AVAI added PSCs for 12 cells of each composition.

Table ST5.1. Atomic concentrations of different elements on the surfaces of pristine and 5-AVAI added $FASnI_3$ films, calculated from the XPS survey spectra.

Sample	C 1s	N 1s	O 1s	F 1s	Sn 3d5	I 3d5
Pristine $FASnI_3$	23.2%	14.7%	17.2%	2.7%	18.1%	21.8%
With 5-AVAI $FASnI_3$	34.3%	11.7%	19.6%	0.9%	15.0%	17.7%

Table ST5.2. Atomic ratio of Sn:I on the surfaces of pristine and 5-AVAI added $FASnI_3$ films, calculated from the XPS survey spectra.

Sample	Sn: I
Pristine $FASnI_3$	1.0: 1.2
With 5-AVAI $FASnI_3$	1.0: 1.2

Chapter 6

Conclusions

To meet the future energy demand, the development of renewable energy is the most efficient response of mankind. In this regard, sun represents the most safe and unlimited renewable source of energy. For this reason, the solar cells, convert the sunlight into electricity, have experienced a constant development over time. Among the existing solar cell technologies, the perovskite solar cells (PSCs) have been recognized as a potential candidate for future energy harvesting. Due to the continuous research efforts from all over the world, the power conversion efficiency (PCE) of PSCs has been approached to the established PV technology within a few years. The low cost and easy fabrication and rapid progress in PSCs performance have motivated researchers to solve the existing issues. For the commercialization of PSCs, the research community has focused their attention not only to make efficient device but also stable. In PSCs, the perovskite absorber layer itself is the key issues for the performance. So, the fabrication of perovskite layer with optimum properties and robust stable nature will overcome the problems associated with efficiency and stability. In order to achieve these goals innovative design, detailed analysis, and optimization of fabrication technologies are in constant pursuit. The main focus of this thesis is to develop perovskite film for high efficiency and stable Pb-based and Sn-based PSCs.

In an attempt to optimize the one step anti-solvent dripping (ASD) perovskite film fabrication method, a thorough studied was performed to observe the effects different anti-solvent such as toluene, chlorobenzene, *p*-xylene and ether anti-solvents treatment on the $MAPbI_3$ perovskite film and the performance of corresponding PSCs. The anti-solvents with high boiling point and missible in solvent, such as toluene and chloroebenzene, formed $MAPbI_3$ films with single grain structure and showed highest stability. Due to the stable nature of perovskite films, the corresponding PSCs showed stable performance both in dark and under light soaking condition.

To simplify the ASD method, an additive engineering was incorporated for the fabrication of perovskite film from single solvent precursor solution. $CuCl_2$ was used as additive to control the crystal growth. Cl^- from the $CuCl_2$ controls the perovskite crystallization rate and results in larger, and uniform grain size with optimum optoelectronic properties and showed 56% higher photovoltaic performance than the pristine $MAPbI_3$ based PSCs.

In the following part of this thesis, attempts were taken to substitute the toxic Pb by non-toxic Sn from the absorber layer of PSCs. But for the Sn-based perovskite, the rate of crystal growth is much faster than the Pb-based perovskite which makes pin-hole free uniform film formation challenging. Due to the higher

coordination of Dimethyl sulfoxide (DMSO) with SnI_2, the optimized single DMSO solvent precursor system was used for uniform Sn-based perovskite film. However, still the film contained pinholes with higher Sn^{4+} concentration. To overcome this problem, the dual beneficial aspects of hydrazinium chloride (N_2H_5Cl) additive for uniform Sn-based perovskite film formation by controlling perovskite growth rate and suppression of Sn^{2+} oxidation through its reducing nature have been used. From detail characterization, it was observed that the addition of N_2H_5Cl into the precursor solution assisted to fabricate pin-holes free uniform perovskite films with lowered Sn^{4+} content with longer PL lifetime. As a result, the PCE of $FASnI_3$ based PSCs improved twice as compared to the pristine one and showed enhanced self-life time.

In an attempt to improve the stability, most importantly the operational stability of Sn-based PSCs, another coadditive engineering was performed with hydrophobic long carbon chain organic additive with bifunctional groups, 5-ammonium valeric acid iodide (5-AVAI). The suppression of Sn^{2+} oxidation and enhancement of PL lifetime of Sn-based perovskite film were observed with the addition of 5-AVAI which augmented the PCE of $FASnI_3$-based PSCs twice with a large surface area (0.25 cm^2) area. Moreover, the incorporation of 5-AVAI into the precursor solution formed a thin layer on the surface of $FASnI_3$ films which protected the film from moisture and air resulting in enhanced film stability. This robust nature of $FASnI_3$ films made it possible for corresponding PSCs to maintain their initial performance for 100 h under continuous illumination under maximum power point tracking system, which is the longest period of light soaking stability for Pb free perovskite solar cells.

List of Publications

1. **M. E. Kayesh**, K. Matsuishi, R. Kaneko, S. Kazaoui, J. J. Lee, T. Noda and A. Islam, "Coadditive Engineering with 5-Ammonium Valeric Acid Iodide for Efficient and Stable Sn Perovskite Solar Cells." *ACS Energy Lett*., **2019, 1,** 278-284.

2. **M. E. Kayesh**, T. H. Chowdhury, K. Matsuishi, R. Kaneko, S. Kazaoui, J. J. Lee, T. Noda and A. Islam, "Enhanced Photovoltaic Performance of $FASnI_3$ Based Perovskite Solar Cells with Hydrazinium Chloride (N_2H_5Cl) Co-Additive." *ACS Energy Lett*., **2018**, **3**, 1584-1589.

3. **M. E. Kayesh**, K. Matsuishi, T. H. Chowdhury, R. Kaneko, J. J. Lee, T. Noda and A. Islam. "Influence of anti-solvents on $CH_3NH_3PbI_3$ films surface morphology for fabricating efficient and stable inverted planar perovskite solar cells." *Thin Solid Films*, **2018, 663**, 105-115.

4. **M. E. Kayesh**, K. Matsuishi, T. H. Chowdhury, R. Kaneko, T. Noda and A. Islam, "Enhanced photovoltaic performance of perovskite solar cells by copper chloride ($CuCl_2$) as an additive in single solvent perovskite precursor". *Electron. Mater. Lett*. **2018, 14**, 712.

Other Related Publications

1. T. H. Chowdhury, R. Kaneko, **M. E. Kayesh**, M. Akhtaruzzaman, K. B. Sopian, J. J. Lee, and A. Islam. "Nanostructured NiOx as hole transport material for low temperature processed stable perovskite solar cells." *Mater. Lett.,* **2018, 223**, 109-111.

2. T. H. Chowdhury, M. Akhtaruzzaman, **M. E. Kayesh**, R. Kaneko, R., T. Noda, J. J. Lee, and A. Islam, "Low temperature processed inverted planar perovskite solar cells by r-GO/CuSCN hole-transport bilayer with improved stability." *Solar Energy*, **2018, *171*,** 652-657.

3. R. Kaneko, Towhid H. Chowdhury, G. Wub, **M. E. Kayesh**, S. Kazaoui, K. Sugawa, J.J. Lee, T. Noda, A.Islam and J. Otsuki. "Cobalt-doped nickel oxide nanoparticles as efficient hole transport materials for low-temperature processed perovskite solar cells" *Solar Energy*, **2019, 181,** 243-250.

List of Conferences

A. Oral Presentations

- **Md. Emrul Kayesh**, Towhid Hossain Chowdhury, Ashraful Islam, Kiyoto Matsuishi, "Influence of Anti-Solvents of $CH_3NH_3PbI_3$ Film Morphology: Efficient and Stable Inverted Planar Perovskite Solar Cells." The 78th JSAP Autumn Meeting, **2017**, Fukuoka, Japan
- **Md. Emrul Kayesh**, Kiyoto Matsuishi, Towhid H. Chowdhury, Ryuji Kaneko, Said Kazaoui, Jae-Joon Lee, Takeshi Noda, Ashraful Islam,
  "Co-additive Engineering of Lead free Perovskites Solar cells for Enhanced Photovoltaic Performance and Improved Stability" The 79th JSAP Autumn Meeting, **2018**, Nagoya, Japan

B. Poster Presentations

- **Md. Emrul Kayesh**, Kiyoto Matsuishi, Towhid H. Chowdhury and Ashraful Islam, "Effects of Reducing Salt on Sn-Based Perovskite Films and their Solar Cell Performance" AP-HOPV -**2018**, Kitakyushu, Japan.
- **Md. Emrul Kayesh,** Kiyoto Matsuishi, Towhid H. Chowdhury, Ryuji Kaneko, Said Kazaoui, Jae-Joon Lee, Takeshi Noda and Ashraful Islam. "Co-additive Engineering with Bifunctional Additive for Enhanced Performance and Improved Stability of Sn-based Perovskites Solar Cells" IPEROP- **2019,** Kyoto, Japan.

Acknowledgements

First of all, I would like to express my deepest gratitude to **Prof. Kiyoto Matsuishi,** Institute of Materials Science, University of Tsukuba. He has not only accepted me as a Ph.D. student in his research group but also provided constant guidance, encouragement and metal support to pursue my research freely. At the same time, **Prof. Matsuishi** was always there to solve my questions, review my papers and support me beside academic research. I believe that my doctoral studies have been gotten this extent form due to his keen interest and wisdom.

I also would like to express my deepest gratitude to **Prof. Ashraful Islam,** Photovoltaic Materials Group, National Institute for Materials Science (NIMS). From the beginning of my study, **Prof. Islam** put a lot of trust on me and offered unconditional support. This is he to whom I got the highly sensitive device fabrication facilities. Besides, he spent endless time for discussion and explanations on the research results and reviewing my papers.

I would like to thank Prof. Ohshima Kenichi and Prof. Miwako Takahashi, Institute of Materials Science, University of Tsukuba, for teaching and providing me the knowledge about crystal structure experiment and analysis.

I would also like to thank all the present and past Matsuishi lab members specially, Koyama san, Suzuki san, Shimomura san, Takahashi san, Nakayama san for their friendly behavior, technical support and kind help inside and outside of laboratories. I would like to convey my gratitude and profound acknowledgements to my group member at National Institute of Materials Science (NIMS) namely (in family name order) Dr. Towhid H. Chowdhury, Dr. Xiao, Dr. Xiangyue and Mr. Ryuji Kaneko for being generous and kind to me.

I am highly thankful to the Japan government for providing me the financial support for whole period of research work as MONBUKAGASHO (MEXT) scholarship.

Finally, I would like to thank my parents and my family for their encouragement, patience, sacrifice and unconditional love during my work. Last but not least, I would like to thank my wife Jannatul Ferdous for her sacrifice, patience, care, love, support, knowledge that providing me the wisdom to pursue my Ph.D. degree throughout all these years.